

STRAIN RATE AND TEMPERATURE DEPENDENCE ON THE CONSTITUTIVE
BEHAVIOR OF ADVANCED STRUCTURAL ALLOYS
FOR AEROSPACE SYSTEMS

by

OMAR L. RODRIGUEZ

PAUL G. ALLISON, COMMITTEE CHAIR
J. BRIAN JORDON
STEVE DANIEWICZ
DAVID W. MACPHEE
LIN LI
WILBURN R. WHITTINGTON
BRUNO ZAMORANO-SENDEROS

A DISSERTATION

Submitted in partial fulfillment of the requirements for the degree
of Doctor of Philosophy in the Department of Mechanical
Engineering in the Graduate School of
The University of Alabama

TUSCALOOSA, ALABAMA

2018

Copyright Omar L. Rodriguez 2018
ALL RIGHTS RESERVED

ABSTRACT

Titanium alloys and Nickel-based superalloys are omnipresent in advanced aerospace and terrestrial systems due their combination of specific material properties (normalized by density) and superb performance at elevated temperatures. Although found in automotive, biomedical and sporting goods industries the materials high costs impede their widespread usage. When applicable, Additive Manufacturing (AM) technologies such as Electron Beam Melting (EBM) and Selective Laser Melting (SLM) could alleviate production costs by reducing the amount of raw material needed, machining processes and personnel.

While the aerospace-grade structural materials market has been traditionally dominated by conventional alloys such as the above described High Entropy Alloys (HEAs) have emerged as potential candidates given their combination of excellent stability, high strength, corrosion and fatigue resistance. HEAs are loosely defined as alloys containing five or more principal elements, each with a concentration between 5-35 at. %. Notwithstanding its complex chemical arrangement, a multiplicity of reports in the open literature identified the formation of solid solution phases consisting, generally, of simple FCC and/or BCC crystal structures.

The foundation of this doctoral dissertation lays at the intersection of material science and mechanical engineering. Is on the basis of the correlation between processing physical descriptors, materials structure and properties that an engineer can design an industry or application specific component with predictable performance. Consequently, this document summarizes a comprehensive investigation of the microstructural features (initial state and deformed) and first tier mechanical properties of current and potential aerospace-grade alloys,

i.e., EBM Ti6Al4, SLM IN718 and as-cast HEAs. Particular emphasis was placed on documenting the high deformation rate (10^3 - 10^5 s $^{-1}$) plastic response. The body of knowledge on quasi-static behavior (10^4 - 10^1 s $^{-1}$) is vast, however, the scientific literature is, at most limited, in reporting mechanical properties on the high rate domain.

DEDICATION

This dissertation is dedicated to my family, who provided her continual support and encouragement throughout the duration of this work.

ACKNOWLEDGEMENTS

While accredited to my name, this document is not mine alone. I am in great debt to a number of people for their invaluable contributions. My list should start with committee and faculty members: Dr. J. Brian Jordon, Dr. Steve Daniewicz, Dr. David MacPhee, Dr. Lin Li, Dr. Wilburn Whittington, Dr. Bruno Zamorano-Senderos and Dr. Mark Barkey. Although, you were the reason for endless hours at the laboratory this work could not have come to fruition without your ideas and suggestions.

Friends alleviate the grueling time that graduate school constitute. To Dr. Oscar Rivera, Abby Cisko, Dr. Joao Morales and Dr. Todd Butler: thanks for all the moments.

A special category is reserved to Tito Rodriguez, Ruth Hidalgo and Dr. Rogie Rodriguez. One is my sibling, the other two acts like it, all role models for me.

Lastly, my deepest debt is to Dr. Paul Allison. Not only you provided me the opportunities and tools for a successful life after school but also with lessons to become a better person.

CONTENTS

ABSTRACT	ii
DEDICATION	iv
ACKNOWLEDGEMENTS	v
LIST OF TABLES	viii
LIST OF FIGURES	ix
CHAPTER 1 INTRODUCTION.....	1
1.1 Intellectual Merits	1
1.2 Additive Manufacturing.....	4
1.3 Microstructure and Mechanical Properties: Ti6Al4V.....	7
1.4 Microstructure and Mechanical Properties: INCONEL718	11
1.5 Microstructure and Mechanical Properties: High Entropy Alloys	13
1.6 Objectives	18
CHAPTER 2 STRAIN RATE EFFECT ON THE TENSION AND COMPRESSION STRESS-STATE ASYMMETRY FOR ELECTRON BEAM ADDITIVE MANUFACTURED TI6AL4V.....	20
2.1 Introduction.....	21
2.2 Experimental Procedures	22
2.3 Results and Discussion	24
2.4 Concluding Remarks.....	45

CHAPTER 3 INFLUENCE OF THERMAL POST-PROCESSES ON MORPHOLOGY AND TENSILE RESPONSE OF INCONEL 718 FABRICATED BY SELECTIVE LASER MELTING ADDITIVE MANUFACTURING.....	53
3.1 Introduction	54
3.2 Experimental Procedures	56
3.3 Results and Discussion	58
3.4 Concluding Remarks.....	66
CHAPTER 4 PROCESSING, MICROSTRUCTURE AND MECHANICAL PERFORMANCE OF THE $\text{Al}_x\text{CoCrFeNi}$ HIGH-ENTROPY ALLOY SYSTEM WITH MULTIPRINCIPAL ELEMENTS.....	71
4.1 Introduction	72
4.2 Experimental Methods	74
4.3 Results and Discussions	75
4.4 Concluding Remarks.....	94
CHAPTER 5 SUMMARY AND FUTURE DIRECTIONS	101
REFERENCES	106

LIST OF TABLES

Table 1-1 Comparison of PBF technologies [18], [19].....	6
Table 2-1 Summary of AM PBF Ti6Al4V QS tensile properties for different orientations and post-processing conditions. Adapted from [35].....	27
Table 3-1 Thermal Post-Processes: SLM IN718 Test Articles.....	57
Table 3-2 Summary of AM PBF and DED Laser-Melted IN718 QS tensile properties for different orientations and post-processing conditions. Adapted from [38].	64

LIST OF FIGURES

Figure 1-1PBF technologies schematics (a) EBM and (b) SLM. Reprinted from [18].....	5
Figure 1-2 Overview of relationship between input parameters and underlying physics to meet the expected outcome of metal AM. Reprinted from [18].....	7
Figure 2-1 (a) Bright field 3D OM composite for as-built EBM Ti6Al4V. Z axis indicates build direction. (b) SE SEM metallography insets presents grain morphology; equiaxed grain structures at XY plane. Meanwhile (c) depicts the columnar micro-architecture parallel to the building direction. Both micrographs illustrate α (HCP), β (BCC) and γ (HCP) phases in detail.	25
Figure 2-2 True stress - true strain relations for quasi-static ($\dot{\epsilon} = 0.001 \text{ s}^{-1}$), and dynamic ($\dot{\epsilon} = 1500 \text{ s}^{-1}$) tensile results. Unlike the previous publication [14], the effects to load frame compliance and elastic wave propagation equilibrium were considered here for the static and dynamic samples by correcting the elastic portion of the deformation curves. Also, the flow stress curves reveal the weak dependance of the plastic flow on deformation rate.	29
Figure 2-3 The strain hardening rate dependence on tensile ductility ($\Theta(\dot{\epsilon})$) identified the dominant deformation mechanism as elongation progress. As often reported for Ti and Ti alloys the Θ dependency on deformation is featured as a multi-stage curve [49]–[52].	31
Figure 2-4 OM fractograph (a) depicts a cup-and-cone fracture topography for the quasistatically deformed ($\dot{\epsilon} = 0.001 \text{ s}^{-1}$) uniaxial tensile specimen. As observed on the SE SEM micrograph the central zone fracture topography is characterized by equiaxed dimple rupture. The same fractographic analysis demonstrates the shear nature of the dynamic fractured specimen ($\dot{\epsilon} = 1500 \text{ s}^{-1}$). OM micrograph presented at (b) shows that the fracture surface of the dynamic specimen is aligned with the maximum shear plane (45°). Shear dimples are observed on the SE SEM photomicrograph.	32
Figure 2-5 True stress – true strain flow curves for compression mode under different deformation rates ($\dot{\epsilon} = 0.001$, and 1000 s^{-1}). At the macroscopic level compression results exhibit a rate sensitivity of the flow stress and prominent strain hardening.	33
Figure 2-6 The strain hardening rate dependence on true compression strain ($\Theta(\dot{\epsilon})$), maps the dominant deformation mechanisms as the contraction evolved. Notice that the progression of the static strain hardening rate follows a similar behavior that their tensile counterpart. Meanwhile, the strain hardening rate response of high rate compression specimens shows pronounced stage transitions.....	36

Figure 2-7 Low magnification OM metallographs illustrates the V-shaped ASB that propagated through a non-fractured HR compression sample. The transverse section morphology also reveals band bifurcation and intricate variants of Widmanstätten α -laths, which were shortened or elongated, due to severe localized deformation. Void coalescence and shear crack front are depicted by SE SEM's Inset A. Meanwhile, a not-to-scale schematic illustrating the microstructural evolution process, is superimposed on the EBSD inset. The grain orientations are represented by the color-coded Inverse Pole Figure (IPF) map..... 37

Figure 2-8 SE SEM micrograph illustrating the topography of a dynamically fractured ($\epsilon = 1000 \text{ s}^{-1}$) compression specimen with ductile-shear dimples and smeared surface regions. The relatively smooth and smeared regions are products of the opposite surfaces rubbing. The inset shows a still frame of the high-speed fracture video (25 kfps). Notice light emission oriented diagonally with respect to the loading direction; this is an indication of ASB occurrence after peak stress was attained..... 38

Figure 2-9 Averaged true stress vs true strain comparison of compression and tension results at both QS and HR. The macroscopic response curves show the asymmetry about the stress state increased as strain rate increased. The deformation rate effect on flow stress proves to be more pronounced in compression as expected. Also, strain hardening appeared increased at the lower QS loading rates. Uncertainty bands, representing the standard deviation, are included on the curves. 40

Figure 2-10 Macroscopic compression response at varying temperatures and strain rates suggest that the material's fundamental stress-strain behavior was dominated by the thermal phenomena (softening) rather than by strengthening associated with an increase in deformation rate. Fracture strain was not achieved on any of the tested specimens..... 42

Figure 2-11 Bright field OM depict the structural damage sustained by the compression specimens tested under varying levels of temperature and strain rates. Neither fracture nor ASB initiation strains were achieved on any of the tested specimens. 44

Figure 3-1 As depicted (a) the alternating raster strategy of the SLM IN718 process formed a complex spatial topological structure by overlapping multiple track layer molten pools. In order to alleviate residual stress, repair volumetric defects and spherical microdefects and precipitate strengthening phases, test articles were exposed to a progressive post-processing schedule (b-d) in agreement with specifications and standards for AM aerospace alloys (MSFC-SPEC-3717, ASTM and SAE AMS 5664E) [5], [21]. 60

Figure 3-2 True stress - true strain relations for quasi-static ($\epsilon = 0.001 \text{ s}^{-1}$) and high rate ($\epsilon = 2000 \text{ s}^{-1}$) tensile results for SLM IN718 specimens in as-built, SR, HIP and STA conditions. Cast and wrought IN718 values per SAE AMS specifications [33], [34]. As-built, quasi-static results, not published in the open-scientific literature, were provided by NASA MSFC; specimen geometry in accordance with ASTM E8 standard [36], i.e.,

direction on the micrographs. An schematic of a deformed cylindrical specimen with a coarse grain distribution is included as visual reference (reprinted from [46]). 86

Figure 4-6 Optical photomicrographs documented the microstructural phenomena associated with the various strain hardening stages observed in $\text{Al}_{0.3}$ deformed compression specimens. All optical micrographs presented here are from the longitudinal cross-sections of the specimens with the loading direction parallel to the vertical direction on the micrographs. As plastic deformation progressed the density of deformation marks increased. An schematic of a deformed cylindrical specimen with a coarse grain distribution is included as visual reference (reprinted from [46]). 87

Figure 4-7 Macroscopic response of $\text{Al}_{0.3}$ and $\text{Al}_{0.7}$ obtained by tensile testing at different deformation rates ($0.001, 1400 \text{ s}^{-1}$). Here, the influence Al concentration and microstructural phases is reflected on the strength and ductility levels. Whereas $\text{Al}_{0.7}$ specimens present higher strength values its tensile ductility is minimal when compared to $\text{Al}_{0.3}$. Higher σ_y values were computed for the HR dataset when compared against QS counterparts. While $\text{Al}_{0.7}$ HR test articles achieved elongation to fracture high speed imagery shows that $\text{Al}_{0.3}$ tensile specimens fractured on the fifth loading pulse. 89

Figure 4-8 OM micrographs reveal the level of structural damage on the gage section of quasi-static (a) and high rate (b) $\text{Al}_{0.3}$ and quasi-static (c) and high rate (d) $\text{Al}_{0.7}$ tensile specimens. Tensile loading axis parallel to the vertical direction on the micrographs. It is noted the inhomogeneous deformation within gage section experienced by the $\text{Al}_{0.3}$ specimens are due to coarse grain size distribution. 91

Figure 4-9 Tensile specimen's schematic, superimposed over a cast ingot, illustrates the possibility of equiaxed and columnar grains intersecting at the specimen's stress concentration region. Inserts (b), (c) and (d) displays microstructural features of the fracture on $\text{Al}_{0.7}$. Inset's (d) EDS map displays the fracture initiation and propagation occurred on the less ductile BCC phase. 92

CHAPTER 1 INTRODUCTION

1.1 Intellectual Merits

On a forum organized by the United States Government Accountability Office (GAO) in 2014 the participants identified the challenges of using Additive Manufacturing (AM) to produce functional parts for the medical, aerospace and defense sectors [1]. Among those, the participants delineated the challenges associated with the fabrication of parts with microstructural integrity. From pioneering works [2]–[6] to the dissertation that precede this effort [7], process-microstructural correlations help to establish the route to be adopted in order to ensure product quality by avoiding unwanted defects such as porosity and/or residual stresses that may result in poor mechanical performance. Once the fabrication parameters have been established, it is customary to diagnose mechanical performance, thus completing the process-microstructure-properties characterization pathway necessary to ensure the production of functional parts. By quantifying the plastic behavior and characterizing the deformed microstructure of an AM Ti6Al4V and INCONEL 718 (IN718) under various deformation modes, strain rates, and temperatures, this work aims to contribute to the physical properties library of advanced structural materials. “First-tier” mechanical properties (yield, ultimate and fracture strengths etc.) experimentally obtained by this investigation may be used not only as criteria for alloy development and/or selection but also as data necessary to calibrate and validate constitutive equations used in material models.

A similar contribution is proposed for the novel field of High Entropy Alloys (HEAs). While the aerospace-grade structural materials market has been traditionally dominated by conventional alloys (steels, nickel-based and titanium alloys), HEAs have emerged as potential candidates given their combination of excellent stability, high strength, corrosion and fatigue resistance. In early studies, single phase HEAs were usually chosen as a model system to investigate the fundamental physical mechanisms and mechanical behavior due to their simplified structure [8]. Recently, there has been a shift towards multiphase HEAs fueled by scientific publications that documented their superb mechanical performance at high temperatures [9]–[11].

For instance, an increase in Al concentration on a multiprincipal system promotes phase transformation. Transitions from a single phase FCC lattice to a duplex FCC+BCC type and finally to a BCC structure has been documented by several studies [8], [12] on $\text{Al}_x\text{CoCrFeNi}$ HEAs. Moreover, as reported by Tang et al. [12], by increasing the Al concentration on the aforementioned HEA system an increase in strength is observed while its ductility is reduced. Meanwhile, a later study by the same authors [13] revealed a remarkable improvement on tensile ductility due to a microstructural homogenization treatment. The discrepancy on elongation to fracture results by Tang and collaborators [13] on homogenized vs. non-homogenized specimens revealed the importance of the composition-processing-microstructure-performance correlations. Tensile specimens, with a similar elemental composition, had a diametrically opposed performance (elongation to fracture) due to microstructural modifications caused by a homogenization treatment (process). Thus, while examinations of the effect of Al concentration on lattice parameters and their effect on the inelastic behavior has been performed previously [8],

[12] this work attempts to develop a deeper understanding by coupling the effect of stress state, strain rate and temperature of an $\text{Al}_x\text{CoCrFeNi}$ ($x = 0.3$ and 0.7 in molar ratio) HEA system.

Recapitulating, the relationship between composition, process, microstructures and mechanical properties for structural materials are complex hence a comprehensive examination is compulsory. Microstructure plays an important role in the material's mechanical properties such as strength, ductility, fracture toughness and crack propagation. In turn, the initial state of the microstructure is dependent on elemental composition, processing methods and thermal procedures [14]. Moreover, the micro-mechanisms of plastic deformation, which its understanding is critical for structural applications, are known to be strain rate and temperature dependent. This work not only correlates the composition to the processing parameters, microstructures and mechanical response for three different material systems (Ti6Al4V, IN718 and $\text{Al}_x\text{CoCrFeNi}$) but also aim to explain the obtained flow stresses in terms of their underlying plasticity carriers.

This dissertation can be separated in two main parts. The first, which is represented by Chapters 2 and 3, is a study of the influence of deformation conditions on the plastic behavior of AM Ti6Al4V and IN718. Specifically, flow stress dependence on strain rate, stress state and temperature was investigated for an Electron Beam Melting (EBM) AM Ti6Al4V (Chapter 2) while the influence of thermal post-processes on the tensile plastic behavior (at varying deformation rates) was assessed for a Selective Laser Melting (SLM) AM IN718 (Chapter 3). The latter part of this document (Chapter 4) constitutes a study, following the blueprint established on Chapter 2, of HEAs ($\text{Al}_x\text{CoCrFeNi}$) with varying levels of aluminum. Lastly, the remainder of Chapter 1 provides the necessary background whereas Chapter 5 state the conclusions and recommendations for the whole document.

1.2 Additive Manufacturing

Although rapid prototyping and related layer manufacturing processes have been developed over the past several decades, the recent availability of commercial systems have posted revolutionary manufacturing concepts [15]. Additive Manufacturing (AM), termed by some researchers as “the next renaissance in manufacturing,” [16] offers many promising benefits such as reducing the need for tooling accessories, i.e. molds and jigs, and allowing for more optimized and complex components to be produced than conventional manufacturing techniques. These attributes make AM especially applicable to the automotive, aerospace, defense, electronics and medical/biomedical industrial sectors.

The American Society for Testing and Materials (ASTM) F42 Committee on AM has issued a standard on process terminology [17]. A total of seven process categories were identified. As defined by the committee:

- **Binder Jetting** - an additive manufacturing process in which a liquid bonding agent is selectively deposited to join powder materials.
- **Direct Energy Deposition** - an additive manufacturing process in which focused thermal energy is used to fuse materials by melting as they are being deposited.
- **Material Extrusion** - an additive manufacturing process in which material is selectively dispensed through a nozzle or orifice.
- **Material Jetting** - an additive manufacturing process in which droplets of build material are selectively deposited.
- **Powder Bed Fusion** - an additive manufacturing process in which thermal energy selectively fuses regions of a powder bed.

- **Sheet Lamination** - an additive manufacturing process in which sheets of material are bonded to form an object.
- **Vat Photopolymerization** - an additive manufacturing process in which liquid photopolymer in a vat is selectively cured by light-activated polymerization.

Of the seven F42 standard categories only four pertain to metal AM, these are: Powder Bed Fusion (PBF), Direct Energy Deposition (DED), Binder Jetting and Sheet Lamination. This research characterizes two different metal systems (Ti6Al4 and IN718) fabricated via PBF technologies, therefore, hereinafter, only PBF technologies are discussed.

PBF includes all processes where focused energy (electron beam or laser beam) is used to selectively melt or sinter a layer of a powder bed. Schematics of current PBF technologies, Electron Beam Melting (EBM) and Selective Laser Melting (SLM) are presented by Figure 1-1.

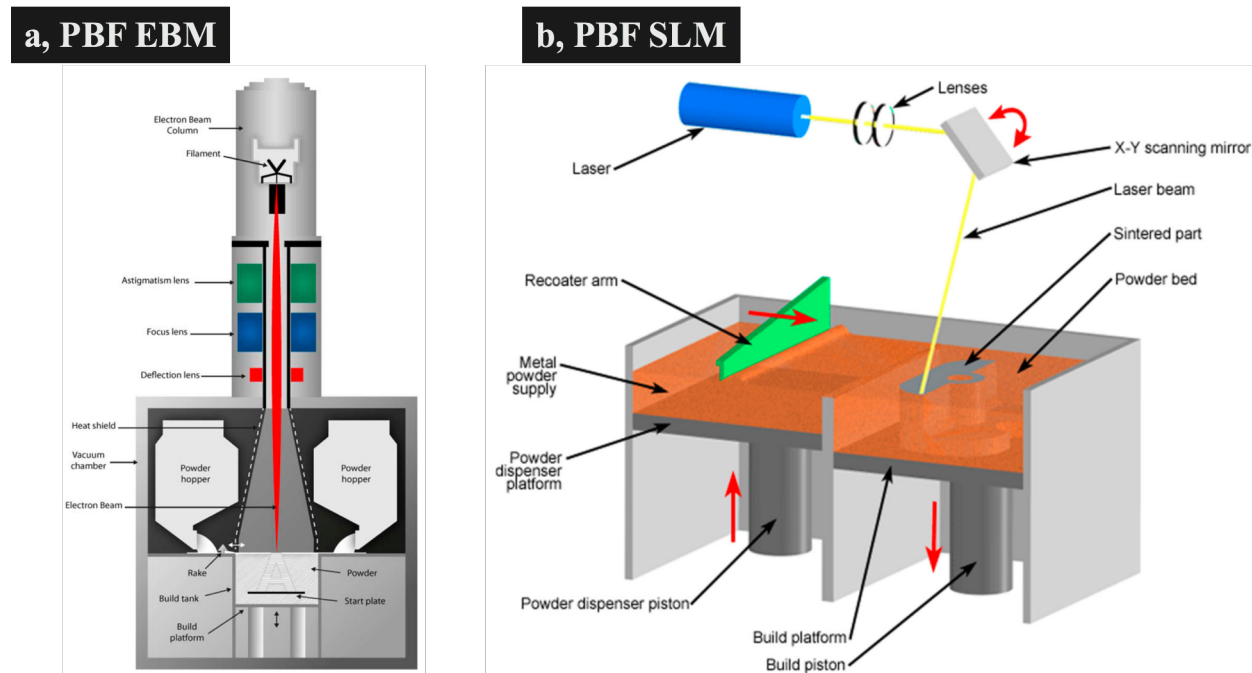


Figure 1-1 PBF technologies schematics (a) EBM and (b) SLM. Reprinted from [18].

Although, both systems use the same powder-bed principle for layer-by-layer deposition there are fundamental differences in hardware between technologies. EBM systems hardware are

configured as a high-power Scanning Electron Microscope (SEM). Meanwhile, in general, SLM systems relies on lenses and a scanning mirror or galvanometer to manoeuvre the position of the beam. With respect to powder distribution, SLM technologies typically use a powder hopper system and soft distribution blades (other systems may use a dispersing piston and roller), whereas EBM platforms use powder hoppers and a metal rake. Moreover, additional differences between EBM and SLM platforms are summarized in Table 1-1.

Table 1-1 Comparison of PBF technologies [18], [19]

	PBF EBM	PBF SLM
Feedstock Quality	GA, RA, PA or PREP 45-100 μm	GA, RA, PA or PREP 10-45 μm
Build Atmosphere	Vacuum ($< 5 \times 10^{-2}$ Pa chamber pressure $< 5 \times 10^{-4}$ Pa column pressure)	Inert gas (Ar, Ni) fill or flow over build surface
Build Envelope	Enclosed Volume	Enclosed Volume
Beam Diameter	0.2 – 1.0 mm	0.1 – 0.5 mm
Layer Thickness	100 μm	50 – 100 μm
Surface Finish	Ra 25/35 μm	Ra 9/12 μm
Residual Stress Levels	Low	High
Required Thermal Post-Process	HIP - optional	SR – required, HIP - preferred
Repair Remanufacture	Possible in limited applications	Not possible

GA: Gas Atomization, RA: Rotary Atomization, PA: Plasma Atomization, PREP: Plasma Atomization Electrode Process
HIP: Hot Isostatic Press, SR: Stress Relief

In order to understand the intricate correlations between processing parameters and the product of an AM process, it is useful to consider a general process flow chart (Figure 1-2) [18]. Here, the process inputs are AM hardware and software, part geometry, raster strategy, build chamber atmosphere and feedstock quality. Moreover, the process outputs are mechanical properties, failed builds and geometric conformity (feature size, geometry scaling). Thermal interactions, enclosed on a box, are due to applied energy, beam interactions, heat transfer and process temperature. For a complete discussion of the interplay between the aforementioned factors readers are referred to [18].

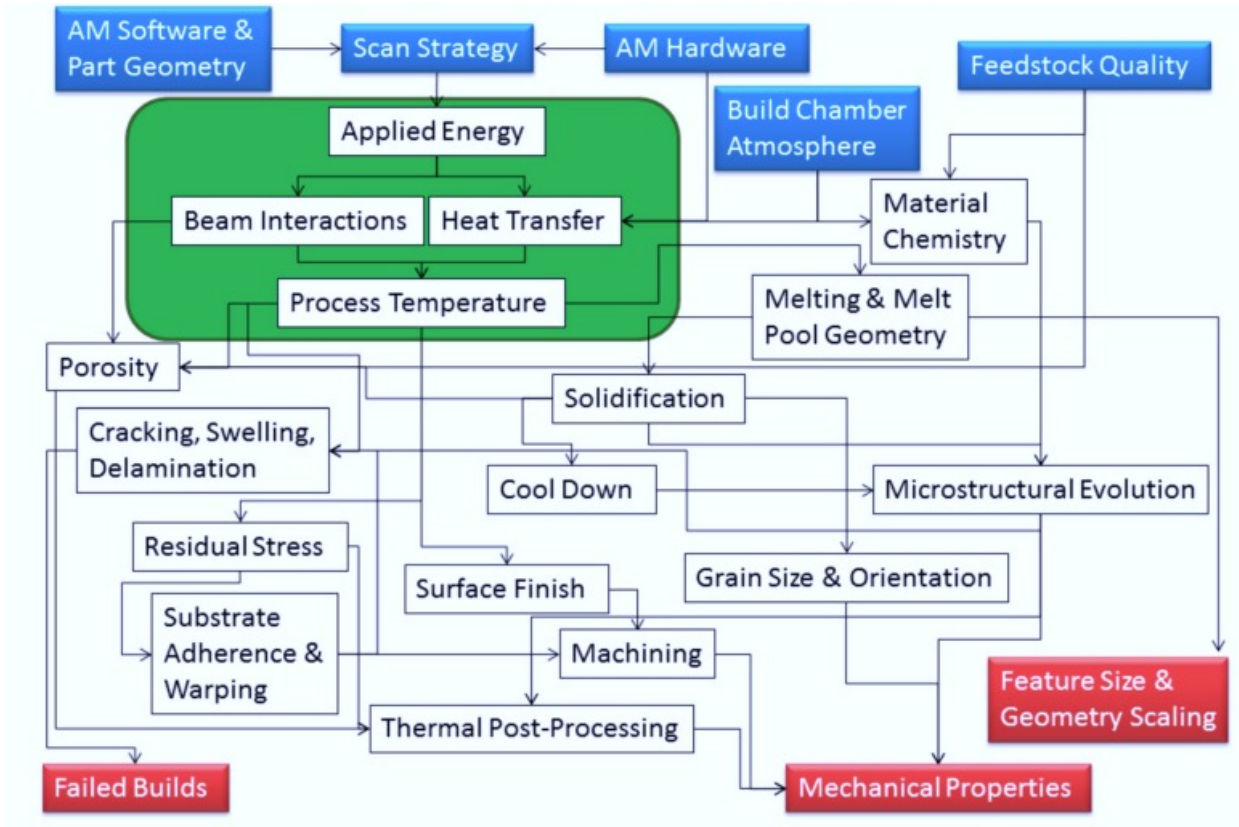


Figure 1-2 Overview of relationship between input parameters and underlying physics to meet the expected outcome of metal AM. Reprinted from [18].

1.3 Microstructure and Mechanical Properties: Ti6Al4V

Of paramount importance is the meticulous mechanical characterization of materials intended for high velocity impact, shock waves and/or ballistic service conditions. Consequently, the response of Ti and Ti alloys, and their sensitivity to deformation rate, temperature and stress state, has been extensively reported in literature from watershed publications by Meyers et al. [20], da Silva and Ramesh [21] Liao and Duffy [22] and Nemat-Nasser and coworkers [23] to recent articles centered on characterizing Ti6Al4V [24]–[28] and AM Ti6Al4V [29]–[33]. In addition to researching deformation rate, temperature and stress state influences, several researchers have investigated the flow stress dependence on initial microstructures [34]–[36]. In

fact, studies have shown that the strain rate dependence on flow stress for Ti6Al4V is different when comparing stress states [37].

In separate studies, Nemat-Nasser et. al [38] and Chichili and coworkers [39] reported the dynamic flow stress of α -Ti. While Chichili and collaborators [39] shed light to the strain rate sensitivity and work hardening of α -Ti plastic flow, Nemat-Nasser's [38] thermomechanical studies correlates temperature and strain rate to a three-stage strain hardening response.

Furthermore, both investigations identified the underlying deformation micro-mechanism controlling macroscopic dynamic response. For instance at the submicron level, Chichili observed both dislocations and twins [39]. Chichili also pointed out that twin density increased with strain and deformation rate, and that although dislocation glide accounted for the majority of the plastic strain, twin-dislocation interaction plays an important role in strain hardening [39]. Meanwhile, Nemat-Nasser et al. [38] identified a three-stage deformation pattern at a temperature range from 23-525 °C which was ascribed to dynamic strain aging of dislocations caused by solute atoms. Nevertheless, this explanation does not apply to ambient temperature deformation since dynamic strain aging is only essential in Ti in the 225-525 °C temperature range [40]. As later researched in Ti plasticity, a second strain hardening stage usually coincides with the onset of twinning and their resistance to dislocation glide, an initial domain signifies dynamic recovery (typical of metals with high stacking fault energy) and a final-third regime reflects flow saturation [41], [42].

Kapoor and Nemat-Nasser measured the fraction of energy converted into heat during high rate plastic deformation on commercially pure Ti [43]. Based on infrared detector thermal signals, the researchers reported that nearly all the work done during high strain rate plastic deformation was converted into heat, with the temperatures quantified being strongly dependent

on strain rate. In spite that the empirically determined cooling rate lies within the $10^7 \text{ }^\circ\text{C s}^{-1}$ range, the rate of heat generation due to plastic flow exceeds the rate of heat dissipation to the surrounding material [22], [44]. When localized, such a mismatch produces plastic flow instabilities that are manifested as zones of highly localized deformation commonly referred to as Adiabatic Shear Bands (ASB). The ASB phenomena has been noted as the dominant failure mode for metals and alloys subjected to high rate loading conditions observed in ballistic impact, explosive fragmentation and high velocity fabrication [29], [45]. Additionally, several authors have documented that the localization occurs more easily in materials with low thermal conductivity and a high thermal softening rate [29], [30], [46] thus demonstrating that Ti alloys are susceptible to the formation of and subsequent failure by ASB.

Research conducted by Liao and Duffy [22], Rittel and Wang [26] and Landau et al. [27] presents a comprehensive examination of the localized shear zone's microstructural evolution in dynamically-loaded Ti6Al4V. Liao and Duffy [22] reported local strain and strain rate values (75-350% and 8000 s^{-1} respectively) on patterned thin-walled tubular specimens tested in a torsional Kolsky bar. In addition, the authors used an array of infrared detectors to interrogate the local temperature rise during the deformation process; temperature readings within the $440\text{-}550$ $^\circ\text{C}$ range were recorded inside the sheared region. Based on the measured temperature raise and fractography analysis, the authors concluded that there was no clear evidence to suggest that the material within the shear band region had undergone phase transformation. Subsequently, Rittel and Wang [26] research leads to the identification of the three distinct stages in ASB formation (homogeneous, inhomogeneous and localized strain); their findings concur with earlier experimental results reported by Marchand and Duffy [47]. While the latter based their conclusion on high-speed photography of a fiducial grid pattern Rittel and Wang [26] research

rely solely on infrared radiometer measurements. Landau and coworkers [27] expand on the work of Rittel and Wang [26] by examining the shear concentration zone at its vicinity via Transmission Electron Microscopy (TEM) analysis. Both, interrupted and fractured shear compression specimens, presents pronounced microstructural refinement from dislocation cells with increasing misorientation until the formation of dynamically recrystallized grains (DRX).

Although, as shown in the referenced work, there has been a number of dynamic studies on Ti and its alloys, there is scarce work in Ti systems manufactured by AM methods. Understanding the dynamic response of AM materials is of uppermost importance for impact or shock applications, particularly if AM products are intended to substitute their conventional wrought counterparts. In one study, uniaxial dynamic and static compression experiments coupled with microstructural analyses, Biswas et al. [30] identified ASB as the predominant failure mode on Laser-Engineered-Net-Shaped (LENSTM) porous Ti6Al4V. By similar analyses Li and collaborators [31] reported the presence of ASB on dynamically loaded laser-deposited Ti6Al4V. Additionally, the tension-compression asymmetry under high strain rate conditions was discussed. Interesting to note, these studies show that AM process does indeed affect the microstructure and subsequent mechanical properties. Given the wide breath of dynamic reporting of wrought Ti6Al4V in literature, and the current rise of AM methodologies of Ti6Al4V, there exist much to understand regarding the dynamic structure-property relations of AM produced Ti6Al4V.

As in the prior mention, the EBM AM is an attractive process that warrants further investigation of the dynamic response of Ti6Al4V; mainly, since EBM has already been successfully utilized in other Ti6Al4V studies [48]–[52]. In these studies, EBM has shown uniqueness in microstructures that are heavily dependent on the AM input parameters.

Furthermore, the prior work by the authors [20], the first study on dynamic response of EBM AM Ti4Al4V, only focused on the tensile response and therefore lacks information on how the stress state may affect the performance of components made by EBM. Being that the EBM process has already been shown by the authors to present interesting dynamic properties, connecting this unique microstructure to the stress state dependent dynamic mechanical properties, especially damage and failure, is of great advantage to AM manufacturing of components that may undergo dynamic events in service. As referenced previously, Ti6Al4V has already been shown to have significant strain rate dependence on stress state [37].

1.4 Microstructure and Mechanical Properties: INCONEL718

Inconel 718 (IN718) is a nickel-chromium based superalloy strengthened by disk-shaped ordered body centered tetragonal (BCT) γ'' -Ni₃Nb and spheroidal or cuboidal ordered face centered cubic (FCC) γ' -Ni₃(Al,Ti)-precipitates in coherent austenitic γ matrix . Other major intermetallic precipitates are: acicular, orthorhombic (D0a) δ -Ni₃Nb, discrete metal-carbide (MC) particles and amorphous Laves. Based on its excellent creep properties, oxidation and hot corrosion resistance and superior mechanical properties in a broad range of temperatures alloy 718 is most widely used in aerospace, nuclear and petrochemical industries [53].

IN718 alloy is usually fabricated using conventional melting and casting techniques. However, as often existent in wrought products made from large size ingot, segregation of high-concentration refractory elements (Nb and Mo) will result in some problems such as macro-segregation, formation of freckles, Laves phases, and white spots thus leading to a large variation in mechanical properties [54]. Suitable thermal treatment have been developed to eradicate elemental segregation and precipitate strengthening phases [55].

Thermal treatments are required for many aerospace alloys to achieve their desired properties. In particular, nickel-chromium based IN718 alloy requires a solution and precipitation heat treatment that generates the microstructure required for the realization of the alloy's high strength. In terms of mechanical properties, solution treatment (ST) dissolve detrimental phases while precipitation heat treatment (aging) precipitate and coarsen strengthening intermetallics (γ' and γ'').

With the characters that can produce more homogeneous and finer microstructures, AM techniques are currently being investigated as prospective candidates to complement or replace conventional production processes [56]. In particular, PBF platforms are generally encountered in the open literature as the IN718 AM technique of predilection for IN718 production [54], [57]–[61]. However, material produced via SLM requires at least one additional post-process. A hot isostatic pressing treatment (HIP) recrystallizes the alloy microstructure and close internal pores and cracks, allowing subsequent heat treatments to be effective at generating desired properties. Additionally, a stress relief (SR) treatment may facilitate microstructure recrystallization and reduce residual stress and the resulting distortion that can occur upon part removal from the build platform. Therefore, SLM components are typically SR-processed prior to removal from the substrate.

Amato and collaborators [59] studied the influence of thermal post-processes on the SLM IN718 hardness. As reported, as-built components exhibited a columnar microstructural arrangement composed of primarily <200> textured γ'' phase precipitates within directionally solidified and similarly textured grains. Upon HIP treatment (1163 °C for 4 hours) preceded by SR at 982 °C for 0.5 hours the Vickers microindentation hardness increased to 5.7 GPa from an as-built value of 3.9 GPa. HIP treatment also resulted in a 5–10% volume fraction of

recrystallized material in which the γ'' phase precipitate columns dissolved, and a homogeneous precipitation of primarily coherent spherical or cuboidal-like precipitates occurred. Similarly, Zhang et al. [54] investigated SLM IN718 microstructure and mechanical properties after standard heat treatments (based on Aerospace Material Specification - AMS - standard for wrought IN178). As concluded, after sequential solution treatment and aging the tensile strengths were increased to levels comparable to the wrought material properties while the ductility decreased dramatically due to the precipitation of fine γ' and γ'' phases in the austenitic matrix and needle-like δ phases in the grain interior and grain boundaries. Similarly, Rao and coworkers [53] a uniform precipitation of γ' and γ'' phases after standard AMS heat treatment resulting in substantial improvement of yield strength and slight improvement in ultimate tensile strength.

1.5 Microstructure and Mechanical Properties: High Entropy Alloys

Multicomponent HEAs are a relative new concept in alloy design in which a system is defined to have five or more principal elements with the concentration of each principal constituent varying between 5 and 35 at.%. HEAs could also contain minor elements to modify the properties of the base material system. Consequently, the atomic percentage of each minor element is hence less than 5 at%. The above represents the standard definition as exemplified by the work of Yeh [62]. Hence, this can be expressed as:

$$n_{\text{major}} \geq 5, 5 \text{ at. \%} \leq X_i \leq 35 \text{ at. \%} \text{ and } n_{\text{minor}} \geq 0, X_j \leq 5 \text{ at. \%}$$

where n_{major} and n_{minor} are the number of major and minor elements, respectively, while X_i and X_j are the atomic percentages of major element i and minor element j . This explanation, a composition-based definition, prescribes only elemental concentration while placing no bounds on the magnitude of entropy. Thus, an alternate definition, in terms of configurational entropy

($\Delta S_{\text{conf.}}$), separating low, medium and high entropy alloys was developed [63]. Alloys having configurational entropies at a random state larger than $1.5R$ (where R is the gas constant), notwithstanding if they are single or multi-phase at ambient temperature, are considered HEAs. This definition implies that an alloy has a single $\Delta S_{\text{conf.}}$ value. In that regard, the entropy-based definition assumes that the alloy can be represented by the liquid solution and high temperature solid solution states, therefore one characterizes it by the maximum possible entropy. Although each definition covers a wide range of alloys, both definitions overlap in most part. The compositions in non-overlapping regions are also regarded as HEAs [64]. From the two definitions, which should be regarded as guidelines rather than laws, one should realize that to enhance the formation of solid solution phases and inhibit the formation of intermetallic compounds HEAs should have high $\Delta S_{\text{conf.}}$. This principle guarantees not only the avoidance of intermetallic phases responsible for structural brittleness, but also their feasibility to be synthesized, processed, analyzed, manipulated and used [62], [65].

In spite of the presence of a large number of components, HEAs may show simple phases such as FCC, BCC and FCC+BCC [66]. AlCoCrFeNi [8], [12], [67]–[76] and the Cu version (AlCoCrCuFeNi) [77]–[82], are the most comprehensively studied HEA systems, which depict one of the aforementioned crystallographic arrangements [8], [12], [67]–[76]. The most critical factor affecting the FCC or BCC phase formation appears to be its Valence Electron Concentration (VEC) although the underlying mechanisms are not well understood and require additional research [83]. A published investigation by Guo et. al. [84] proposed a relationship between VEC and microstructure for a myriad of HEA systems. The researchers reported that when the VEC of the alloy is larger than 8, the FCC structure is stabilized where a VEC < 6.8 corresponds to a BCC structures alloy. Coexistence of FCC and BCC phase is observed at VEC

values between 6.87 and 8. In the context of a $\text{Al}_x\text{CoCrFeNi}$, the variation of the Al ratio leads to a variation in the crystal structures [69], [85]. Increasing the Al content induces larger lattice strain and the ensuing distortion leads to relaxation via phase transformation in the crystal structure [86]. Aided by the wide composition range offered by HEAs, researchers started to investigate the multiphase field in the materials with the intention of discovering alloy combinations that benefits not only from a solid solution hardening mechanism, but also from the precipitation strengthening possible in multiphase microstructures.

Wang and coworkers [85] studied the effect of Al content on the crystal structure, morphology and mechanical properties of an $\text{Al}_x\text{CoCrFeNi}$ ($x = 0 - 2.0$ in molar ratio) HEA. Guided by X-Ray Diffraction (XRD) results, the researchers concluded that low Al content ($\text{Al}_{0-}\text{Al}_{0.4}$) forms a single FCC crystal structure. Minor reflection of the BCC phase appears in $\text{Al}_{0.5}$ specimens while FCC reflection peaks disappear in $\text{Al}_{0.8}$ samples. With the aid of Transmission Electron Microscopy (TEM) techniques, a closer inspection revealed the presence of disordered BCC (A2) and ordered BCC (B2) for Al contents larger than a 0.8 molar ratio. In terms of morphology, researchers observed that the solidified microstructure varies from columnar cellular structure ($\text{Al}_0\text{-}\text{Al}_{0.3}$) to columnar dendrite structure ($\text{Al}_{0.4}\text{-}\text{Al}_{0.6}$), then to equiaxed nondendritic grains ($\text{Al}_{0.7}\text{-}\text{Al}_{0.8}$) to equiaxed dendritic grains ($\text{Al}_{0.9}\text{-}\text{Al}_{1.5}$) and finally to non-equiaxed dendritic grain structures ($\text{Al}_{1.8}\text{-}\text{Al}_{2.0}$). Additionally, Wang and collaborators [85] noted that for single FCC structured alloys ($\text{Al}_0\text{-}\text{Al}_{0.4}$) a low hardness of about 120 HV was obtained, however, by adding Al atoms the hardness increased up to a maximum value of 527 HV for the $\text{Al}_{2.0}$ alloy. These results suggested that the formation of BCC structures is the main hardening factor, i.e. precipitation strengthening. Compared with the BCC crystal structure, FCC alloys usually have higher ductility but lower strength since BCC structures have stronger directional

bonding and lack of a truly close-packed slip plane [83]. Furthermore, the increase in interphase area between FCC and BCC phases could be a contributing factor to the material strength since the mean free path of dislocations is reduced in a mixed structure.

The relationship between deformation rate and structural damage for low Al content FCC- structured $\text{Al}_x\text{CoCrFeNi}$ HEAs was documented by Kumar and coworkers [67] and Li and collaborators [76], while the plastic flow dependence on temperature was reported by Li et. al [68], [70] and Komarasamy, Alagarsamy and Mishra [71]. Initial investigations of high strain rate compressive behavior on as-cast FCC-structured $\text{Al}_{0.1}\text{CoCrFeNi}$ suggests that the deformation behavior is similar to low stacking fault energy (SFE) materials where twinning is a dominant mode of plasticity [67]. This is because the surface energy in a twin boundary is closely related to that of a stacking fault since a large part of the work to form a twin goes to creating the twin boundaries [87]. Therefore, as generally seen in FCC materials, a decrease in the SFE results in a decrease in the stress required to nucleate twins. As expected, the authors [67] attributed the rise in strain hardening rate for quasi static (0.001 s^{-1}) and high rate (2600 s^{-1}) compression specimens to dislocation-twin boundary interactions. The investigators also noted that the onset of twinning was dependent on the strain-rate and an exceptional work hardening rate was observed irrespective of the strain-rates. A recent publication [76] expanded on the work by Kumar et. al [67] by investigating the mechanical response of an FCC-structured $\text{Al}_{0.3}\text{CoCrFeNi}$ HEA. In FCC metals, the SFE decreases by increasing the concentration of the solute atom [87], consequently, the SFE of $\text{Al}_{0.3}\text{CoCrFeNi}$ is lower than the $\text{Al}_{0.1}\text{CoCrFeNi}$ alloy. This lead to the formation of profuse mechanical twins although they were only detected in high rate (1800 s^{-1}) compression specimens. On the other hand, TEM studies concluded that the

steady strain hardening during plastic deformation on quasi-static specimens (0.001 s^{-1}) was a product of forest dislocations.

Li and colleagues [70] studied the plasticity of forged $\text{Al}_x\text{CoCrFeNi}$ ($x = 0.1, 0.3$ in molar ratio) under quasi-static (0.002 s^{-1}) uniaxial tensile deformation conditions at different temperatures (-196 °C – RT). As documented, the tensile strength and ductility increased with decreasing temperature in clear contrast to traditional FCC metals. As found in a later study [68], the property enhancement was due to the fact that mechanical nanotwining was the structural flow unit instead of planar slip of dislocations. Deformation-induced nanotwining delays the onset of necking instability (i.e., localized plastic deformation that can lead to premature failure) to higher strains [76].

For higher Al content $\text{Al}_x\text{CoCrFeNi}$ HEAs, the clear majority of literature reporting mechanical properties are focused on one deformation path, compression [8], [69], [74], [85]. This could be related to the lack of ductility associated to the BCC phase that solidifies when the Al concentration exceeds 0.5 molar ratio [83], [85]. Initial results obtained by Tang et al. [13] agrees with the previous statement; a tensile ductility of just 1% was reported for the as-cast equimolar primarily-BBC-structured AlCoCrFeNi tested at 700 °C. The poor ductility was attributed to the difficulty of dislocation movement through the finely-spaced BCC A2+B2 lamellar structure interface. However, the researchers reported in the same study that after a hot isostatic homogenization treatment on the equimolar AlCoCrFeNi specimens, the elongation to fracture improved to 11.7%. The improvement in ductility may be due to the breakage of the BCC A2+B2 lamella into larger domains thus giving longer glide-lengths for the dislocations before hitting an obstacle.

1.6 Objectives

Considering the results discussed in this brief overview it can be concluded that:

1. In PBF AM techniques, the process physical descriptors (sintering and melting temperatures, scan speed and raster strategy, cooling rate, etc.) dictate the microstructure, which in turn affects the mechanical properties. A correlation between processing parameters, the resulting microstructure and mechanical behavior could be used not only as criteria for optimization of processing parameters and alloy selection, but also as data necessary to calibrate and validate constitutive equations used on material models.
2. The field of HEAs offer unique challenges in establishing composition-microstructure-properties correlations. The vast composition space significantly increases the number of possible alloys to characterize. Moreover, even minor adjustments to the ratio of elemental composition may substantially influence the resulting microstructure and properties. Inherently, the vastness of the HEAs compositional space that represents a challenge also offers the potential for alloy development of scientific and practical applications. Consequently, the development of a material database that contains information about the processing history, composition, microstructural features and mechanical response, on a material system that does not necessarily abide the established principles of physical metallurgy, is crucial to guide scientists and engineers on selecting the appropriate alloy for any particular application.

Therefore, this dissertation aims to:

1. Characterize the plastic behavior, and resulting microstructures, under different deformation conditions (stress states, strain rates and temperatures) of an as-built, EBM AM Ti4Al4V.

2. Quantify the influence of thermal post-processes on the plastic behavior of an SLM

IN718

3. Investigate the plastic behavior, and resulting microstructures, under different

deformation conditions (stress states, strain rates and temperatures) of an as-cast HEA

system ($\text{Al}_x\text{CoCrFeNi}$).

CHAPTER 2 STRAIN RATE EFFECT ON THE TENSION AND COMPRESSION STRESS-STATE ASYMMETRY FOR ELECTRON BEAM ADDITIVE MANUFACTURED Ti6Al4V

Omar L. Rodriguez¹, Paul G. Allison^{1*}, Oscar G. Rivera¹, Lin Li², Wilburn R. Whittington³, Haitham El Kadiri³ and Mark E. Barkey⁴

¹ The University of Alabama, Department of Mechanical Engineering, Tuscaloosa, AL, 35487

² The University of Alabama, Department of Metallurgical and Materials Engineering, Tuscaloosa, AL, 35487

³ Mississippi State University, Department of Mechanical Engineering, Starkville, MS, 39762

⁴ The University of Alabama, Department of Aerospace Engineering, Tuscaloosa, AL, 35487

* Corresponding Author: pallison@eng.ua.edu

Keywords: Additive Manufacturing, Electron Beam Melting, Ti6Al4V, High Strain Rate, Stress Asymmetry, Adiabatic Shear Band

Abstract

The present investigation lays the groundwork for coupling the plastic flow stresses of an Additive Manufactured (AM) Ti6Al4V with its corresponding strain hardening rate responses and fracture morphologies at varying strain rates, temperatures and stress states for the first time. The macroscopic response was obtained under different stress states (tension and compression) and deformation rates (ranging from quasi-static at 0.001 s^{-1} to the high rate domain at 1500 s^{-1}) to elucidate the tension-compression asymmetry and strain rate dependence of the material. The results identified that, (a) compressive yield strengths are higher than their tensile counterparts and (b) the strength differential effect is more prominent under high strain rates. The mechanical behavior is explained in terms of deformation mechanism reasoned from close inspection of strain hardening rate curves. Dislocation glide and mechanical twinning contribution as the dominant plastic unit was identified in stages and their relation with deformation mode and rate

was established. Based on fractography analysis of the tensile samples, a rate dependence showed a shift from classic cup-cone fracture at quasi-static rates to fracture along the shear plane at high strain rates. The high strain rate compression samples also show an interesting fracture morphology with high speed video capturing adiabatic shear localization. Close inspection of elevated temperature – high rate flow stress data suggest that the thermal softening effect overrides the strengthening due to high strain rate deformation. Microstructural transformations, especially those occurring in the hot working temperature range (825-1000 °C) requires future investigations.

2.1 Introduction

Of paramount importance is the meticulous mechanical characterization of materials intended for high velocity impact, shock waves and/or ballistic service conditions. Consequently, the response of Ti and Ti alloys, and their sensitivity to deformation rate, temperature and stress state, has been extensively reported in literature from watershed publications by Meyers et al. [1], da Silva and Ramesh [2] Liao and Duffy [3] and Nemat-Nasser and coworkers [4] to recent articles centered on characterizing Ti6Al4V [5]–[9] and AM Ti6Al4V [10]–[14]. In addition to researching deformation rate, temperature and stress state influences, several researchers have investigated the flow stress dependence on initial microstructures [15]–[17]. In fact, studies have shown that the strain rate dependence on flow stress for Ti6Al4V is different when comparing stress states [18].

With the aforementioned in mind, this research effort attempts to develop an understanding of the stress state and strain rate, and deformation temperature dependence of EBM AM Ti6Al4V. The emphasis is placed on the correlation of the macroscopic flow response to failure where the

possible mechanism controlling damage and microstructural aspects of fracture behavior are discussed.

2.2 Experimental Procedures

An ARCAM S12 EBM system located at NASA Marshall Space Flight Center (MSFC) was used to fabricate the samples for this study. Fine pre-alloyed bimodal ($\alpha + \beta$) Ti6Al4V powder, with particle diameter between 45 and 100 μm was used as feedstock precursor. The nominal chemical composition of the as-supplied powder was 6Al, 4V, 0.03C, 0.10Fe, 0.15O, 0.01N, 0.003H, balance Ti (w.t.%). Target pre-heat temperature was set to 730°C. Scan speed was 0.376 m/s with a beam current of approximately 6 mA. Layer thickness was predefined at 70 μm . A detailed microstructural characterization of the precursor powder and discussion of the EBM processing parameters can be found in prior research [19]. The H-shaped, sub-standard sized tensile coupons previously used for both QS and HR tensile experiments on cast, wrought, and AM alloys [20]–[22] (gage length, gl = 4.50 mm, width, w = 2.30 mm thickness, t = 1.50 mm) and cylindrical compression specimens (diameter, φ and length, l = 4.5 mm) were machined from a printed block with their loading axis parallel to build orientation.

To quantify the deformation rate and stress state influence on flow stress, a series of uniaxial experiments were performed on specimens. An INSTRON 5581 load frame equipped with a 50 kN load cell performed the quasi-static tension and compression experiments on sub-standard sized specimens. An optical extensometer technique was employed to capture axial displacement. Dynamic tension and compression experiments were performed with a 350-margaging steel tension-compression Kolsky recovery apparatus ($\varphi = 12.7$ mm) used previously for a variety of wrought and AM materials [20], [22]–[25]. The striker bar had a length of 458

mm while the incident and transmitted lengths equals 2438 mm. Copper pulse shapers ($t,\varphi = 1.5, 5$ mm) were used to eliminate the Pochhammer-Chree oscillations in the incident pulse as suggested by previous researchers [26]. Strain metrology data, obtained using semiconductor strain gages cemented on the bars, was processed by the Split Hopkinson Pressure Bar Graphical Analysis Tool open-source MATLAB® code [27].

Ti6Al4V's dynamic – high temperature compression mechanical dataset is a product of collaboration between The University of Alabama and the National Institute of Standards and Technology (NIST). An exhaustive description of the NIST rapid resisting heated compression Kolsky bar apparatus and testing methodology can be found in published literature [28], however, for the sake of completeness, a brief explanation is provided.

NIST's dynamic compression testing arrangement (maraging steel bars, $l = 1.5$ m, $\varphi = 15$ mm) is outfitted with a rapid heating electrical circuit. Compression pulses are produced in a usual fashion, using a gas gun-striker bar arrangement. Electrical current is conducted directly through the specimen using the bar ends as electrodes. The heating circuit is connected to the compression bars using low-friction graphite bushings located approximately 8 cm from either side of the cylindrical compression specimen. The power source consists of a 2.5V lead acid battery bank connected in series. The amount of power, and the heating rate, is controlled by the number of batteries in the circuit. The specimen temperature is controlled using a millisecond resolution Near Infrared Micro Pyrometer (NIMPY) that serves as a feedback sensor for the power supply.

Ti6Al4V samples were prepared for microstructural observations with standard metallographic procedures including sectioning, mounting, grinding. Optical (OM) and Scanning Electron Microscope (SEM) samples were etched in Keller's reagent (2 mL HF, 4 mL HNO₃,

and 100 mL H₂O). Both, KEYENCE VHX-1000 series digital microscope and a TESCAN LYRA SEM were used for microstructural and fractography analyses. Electron Backscatter Diffraction Analysis (EBSD) characterization was carried out on a TESCAN LYRA SEM on a condition of an accelerating voltage of 20 kV and step size of 0.1 μm.

2.3 Results and Discussion

The as-built microstructure is presented by the bright field 3D optical reconstruction in Figure 2-1. SEM insets illustrates higher magnification micrographs for different planar orientations of the as-built unit cell. Notice the orientation dependence of the initial microstructure with respect to the built axis (z-axis). The equiaxed grain morphology (49.33 μm ± 15.22 μm) observed in the planar region XY resulted from the cross-hatching EBM scanning technique. Epitaxial prior β grains (69.00 μm ± 26.00 μm in thickness), which are delineated by allotriomorphic α grain boundaries (α_{GB}) are direct consequence of the thermal gradient that exists along the deposition direction due to the repeating melting-solidification process. In contrast to other AM processes, for instance laser deposition technology, no layer stratification was observed. Both, equiaxed and columnar grain structures were reported in previous investigations for this material [29], [30].

Inside prior β grains, typical Widmanstätten morphology (colonies and basketweave arrangements) is observed for the transformed α + β alloy. Furthermore, α-laths (1.15 μm ± 0.22 μm in thickness) surrounded by a small amount of β in α boundaries are illustrated by the secondary electron detector (SE) SEM micrograph in Figure 2-1. Another microarchitectural feature revealed by the metallographic analysis is the presence of α' martensitic phase. The martensitic α' plates form as long orthogonally oriented acicular grains with a substructure

consisting of dislocations, stacking faults and some twins [31]. The β - α' solid diffusion-less transformation is responsible for the acicular structures. Albeit, acicular (plate-like) structures can appear in Ti alloys without the presence of the α' secondary phase, several researchers such as Facchini et al. [32], Dehghan-Manshadi, Reid and Dippennaar [33] and Gong [34] had acknowledge the presence on EBM Ti6Al4V.

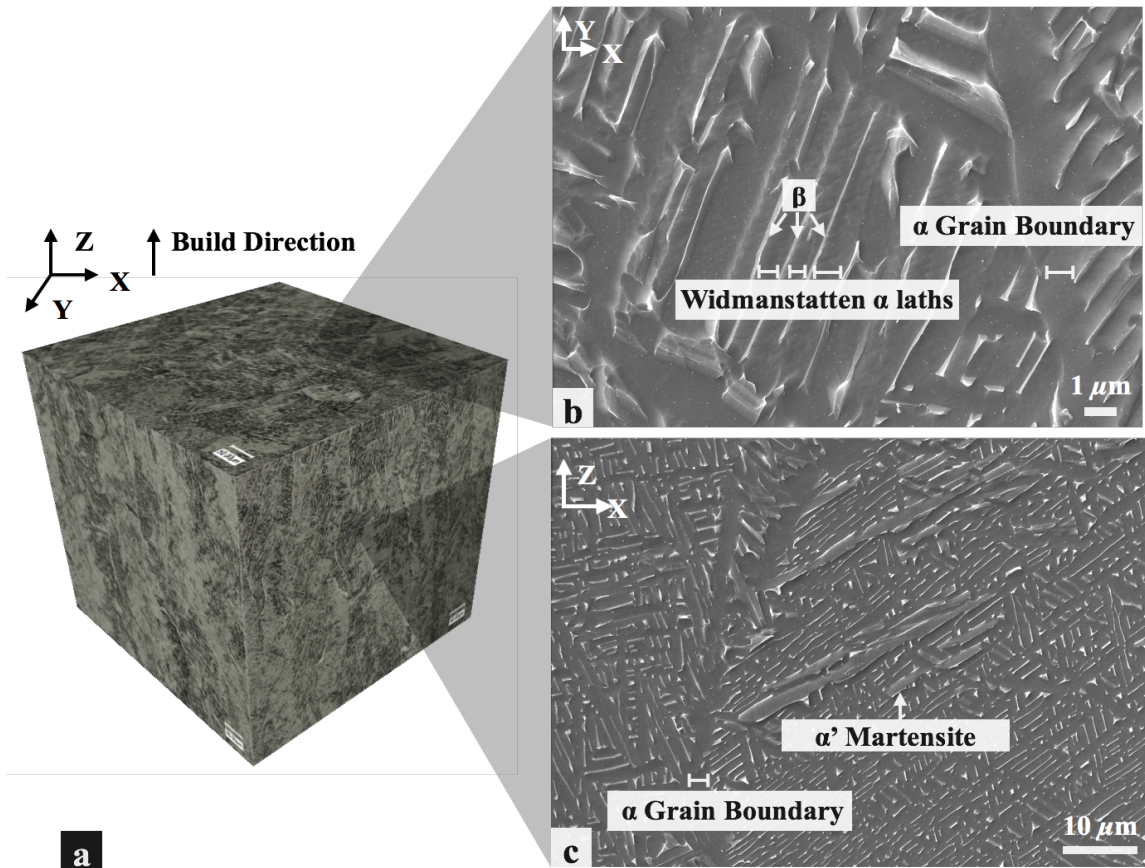


Figure 2-1 (a) Bright field 3D OM composite for as-built EBM Ti6Al4V. Z axis indicates build direction. (b) SE SEM metallography insets presents grain morphology; equiaxed grain structures at XY plane. Meanwhile (c) depicts the columnar micro-architecture parallel to the building direction. Both micrographs illustrate α (HCP), β (BCC) and α' (HCP) phases in detail.

Table 2-1, adapted from a recent publication by Lewandowski and Seifi [35] signifies a comparasion between the QS tensile mechanical properties presented by Figure 2-2 and published data on PBF (EBM and Selective Laser Melting –SLM) Ti6Al4V. Here, “condition” column specifies the level of thermal post-processing on the test article at the time of testing whereas the

build orientation with respect to loading direction, as itemized by the “specimen orientation” column, follows ASTM conventions [36]. In addition, Table 2-1 specifies the AM platform manufacturer. Some general remarks:

- Althougth not reflected on Table 2-1 it is worth to consider that EBM platform manufacturer influence the reported properties [35] . Furthermore, properties variations have been documented on specimens manufactured by the same machine [37], [38].
- It has been concluded by previous investigators that the level of macroscopic residual stresses tends to be higher on components processed by SLM platforms without preheating than on as-built articles deposited by EBM technique [39], [40]. This, in-turn, influence the mechanical response and the thermal post-processing route.
- Notice the orientation-dependent results for σ_y , σ_{UTS} and elongation to failure (ϵ_f). Interestingly, the stress anisotropy level is higher on SLM-processed test articles.
- Thermal post-processes in the form of Hot Isostatic Press (HIP) and Stress Relief (SR) are intended to reduce the inherent anisotropy by modifying the microstructure.
- Given the differences in specimen gage lengths across multiple studies, and the absence of a standarized procedure for mechanical testing of AM materials, a comparison between ϵ_f values is difficult [35].

Table 2-1 Summary of AM PBF Ti6Al4V QS tensile properties for different orientations and post-processing conditions. Adapted from [35].

Powder Bed Fusion (PBF) Electron Beam Melting (EBM) Ti6Al4V						
Machine Type	Condition	Specimen Orientation	σ_y , [MPa]	σ_{UTS} , [MPa]	ϵ_p , [%]	Ref.
ARCAN S12	As-Built	ZX	957 ± 8.3	1104 ± 17.6	11 ± 1.3	This Investigation
		XY	783 ± 15	833 ± 22	2.7 ± 0.4	
ARCAN A1		ZY	812 ± 12	851 ± 19	3.6 ± 0.9	[41]
	ARCAN	As-Built	XY	870 ± 12	971 ± 3.1	12.1 ± 0.9
		Z	879 ± 8	953 ± 8.8	13.8 ± 0.8	[42]
		HIP	XY	866 ± 6.4	959 ± 8.2	13.6 ± 0.6
		Z	868 ± 2.9	942 ± 2.6	12.9 ± 0.8	
ARCAN ELI	As-Built	XY	817 ± 8	918 ± 1	12.6 ± 0.8	[42]
		Z	802 ± 6	904 ± 6	13.8 ± 0.9	
	HIP	XY	814 ± 2.4	916 ± 2.5	13.6 ± 0.8	
		Z	807 ± 8.4	902 ± 8.7	14.8 ± 1.2	
ARCAN A2X ELI	As-Built	Z	928 ± 13.3	1011 ± 14.8	13.6 ± 1.4	[43]
	HIP	Z	813 ± 14.3	908 ± 3.2	17.7 ± 0.9	
Powder Bed Fusion (PBF) Laser-Melted Ti6Al4V						
Machine Type	Condition	Specimen Orientation	σ_y , [MPa]	σ_{UTS} , [MPa]	ϵ_p , [%]	Ref.
EOS	As-Built	XYZ	938 ± 7.7	1140 ± 5	-	[44]
	SR	XYZ	862 ± 3.1	936 ± 3.6	-	
	HIP	XYZ	835 ± 3.8	910 ± 2.9	-	
EOS M280	As-Built	ZX	1017 ± 7	1096 ± 7	12 ± 0.5	[45]
Renishaw MTT 250	As-Built	XY	910 ± 9.9	1035 ± 2.9	3.3 ± 0.7	[46]
Renishaw AM 250	As-Built	XZ	978 ± 5	1143 ± 6	11.8 ± 0.5	[47]
		ZX	967 ± 10	1117 ± 3	8.9 ± 0.4	
		XY	1075 ± 25	1199 ± 49	7.6 ± 0.5	
		XZ	958 ± 6	1057 ± 8	12.4 ± 0.7	
	SR	ZX	937 ± 9	1052 ± 11	11 ± 9.6	
		XY	974 ± 7	1065 ± 21	21 ± 7	
Concept Laser M2	As-Built	X	1070 ± 50	1250 ± 50	5.5 ± 1	[48]
		Z	1050 ± 40	1180 ± 30	8.5 ± 1.5	

HIP – Hot Isostatic Press

SR – Stress Relief

Build orientation on tensile specimens are documented using XYZ designation in accordance to ASTM standard [36]. In this terminology Z designates the build direction.

True stress - true strain curves obtained from static and dynamic uniaxial tension

experiments are presented in Figure 2-2. As observed in the flow stress curves, deformation rate sensitivity is negligible after the accumulation of plastic strain. Higher average yield stress (σ_y) values were calculated for dynamic high strain (HR) rate (avg. $\dot{\epsilon} 1500 \text{ s}^{-1}$) fractured specimens ($\sigma_y = 1030 \pm 17.15 \text{ MPa}$) when compared to those obtained at quasi-static (QS) rates ($\dot{\epsilon} 0.001 \text{ s}^{-1}$) for the tested samples ($\sigma_y = 957 \pm 8.30 \text{ MPa}$). After yielding, the curves experience an increase in flow stress with increasing deformation until the ultimate tensile strength (σ_{UTS}) is reached. Specifically, the curves show that the QS specimens exhibit more hardening after yielding leading up to the σ_{UTS} than the HR specimens. Moreover, for QS tensile specimens the mean σ_{UTS} value reached $1104 \pm 17.55 \text{ MPa}$ while the HR tensile σ_{UTS} reached a similar level at $1105 \pm 3.85 \text{ MPa}$. Besides reinforcing the fact that the effect of deformation rate upon tensile flow stress is weak, the σ_{UTS} marked the onset of softening at both rates tested. After the σ_{UTS} , there is an observable rate dependence on softening where more softening occurs at HR than QS. Fracture occurs at similar elongation levels for QS ($11 \pm 1.30\%$) and HR ($11 \pm 0.06\%$) tensile specimens.

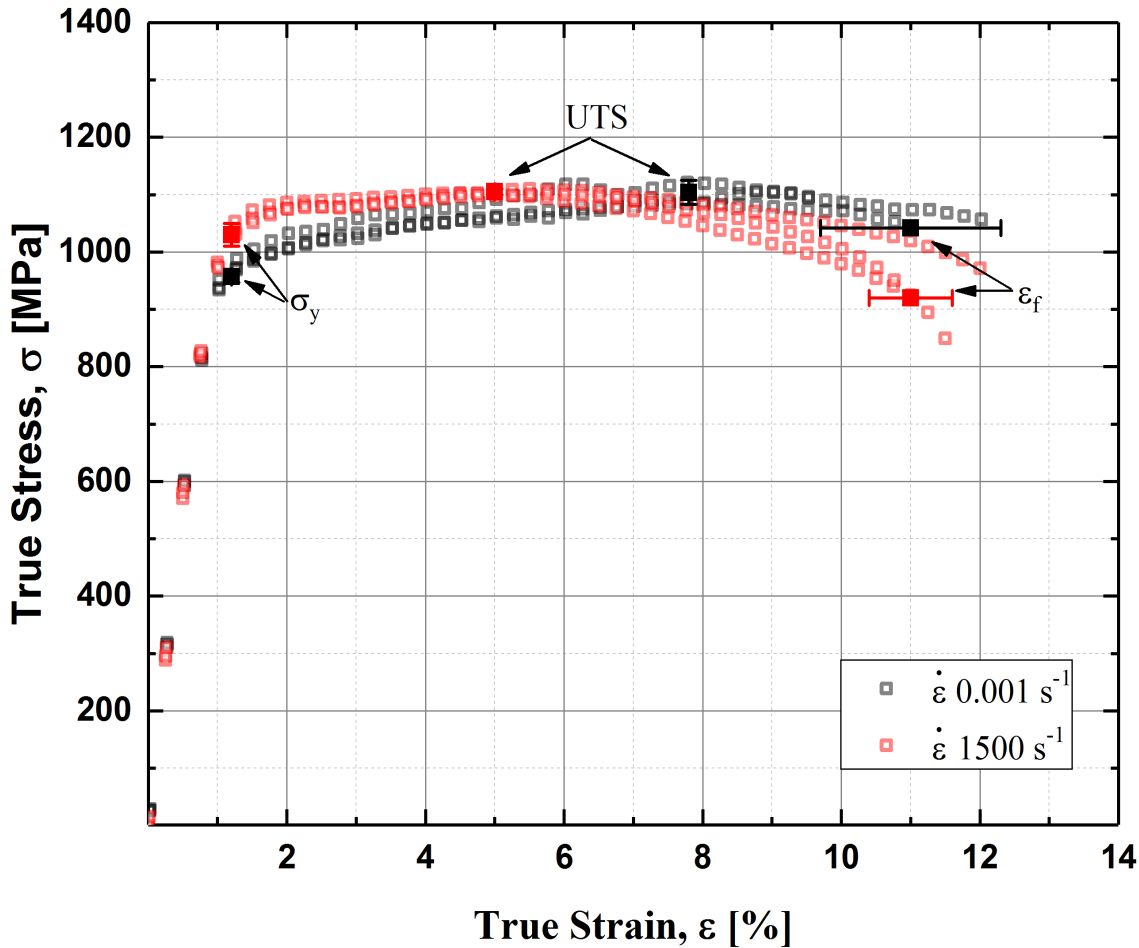


Figure 2-2 True stress - true strain relations for quasi-static ($\dot{\varepsilon} = 0.001 \text{ s}^{-1}$), and dynamic ($\dot{\varepsilon} = 1500 \text{ s}^{-1}$) tensile results. Unlike the previous publication [14], the effects to load frame compliance and elastic wave propagation equilibrium were considered here for the static and dynamic samples by correcting the elastic portion of the deformation curves. Also, the flow stress curves reveal the weak dependence of the plastic flow on deformation rate.

As presented by Figure 2-3 the strain hardening behavior (with associated error bars) is further analyzed by plotting the evolution of the strain hardening rate ($\Theta = d\sigma/d\varepsilon$) in relation to true strain ($\Theta(\varepsilon)$). As often reported for Ti and Ti alloys the Θ dependency on deformation is featured as a multi-stage curve [49]–[52]. More precisely, an initial region (hereafter called Region I) characterized by a decreasing Θ is followed by an increase in the Θ levels (Region II) ending in a new decreasing stage (Region III). There are cases that instead of an increase in Θ during the occurrence of Region II a reduction in the decreasing rate, when compared against the

previous stage, is recorded. This case still supports a three-stage deformation behavior. Moreover, stage transitions as the plastic deformation progresses suggest changes in the underlying deformation micro-mechanisms. For instance, a decrease in Θ suggests a dislocation-slip-driven plasticity while a positive rate usually coincides with the onset of mechanical twining.

Close inspection of the averaged strain hardening rate curve in Figure 2-3 for QS fractured tensile samples reveals the presence of the three distinct stages. After the elastoplastic transition the initial easy glide stage – Region I – culminates in a sharp bend at a strain level of 2.5%. Meanwhile, in Region II, shown here as a compound-stage where there is a plateau followed by a decrease on the Θ . Here, the plateau indicates the onset of mechanical twinning while the Θ decay signifies dislocation-twin boundary interactions via a Hall-Petch type hardening mechanism. The transition to the dislocation-dominated Region III is marked at 3.9% ϵ . By similar means, the dynamic HR tensile averaged strain hardening rate curve shows a three-stage-deformation characteristic with local minima at 2.5% ϵ and local maxima at 3.9% ϵ . Those inflection points marked boundaries between the deformation stages. In the dislocation slip stages, Region I and Region III, the (a) yield point was regulated by dislocation mechanisms and (b) the latter slip-driven region is preceded by the occurrence of mechanical twins. Notice here that Region II is presented as a stage where an abrupt increase in the Θ materialized. Twining and slip are competitive deformation processes with, generally, slip dominating [53]. However, in the case here at high strain rates, twinning became a primary contributor to the plastic deformation [54]–[56].

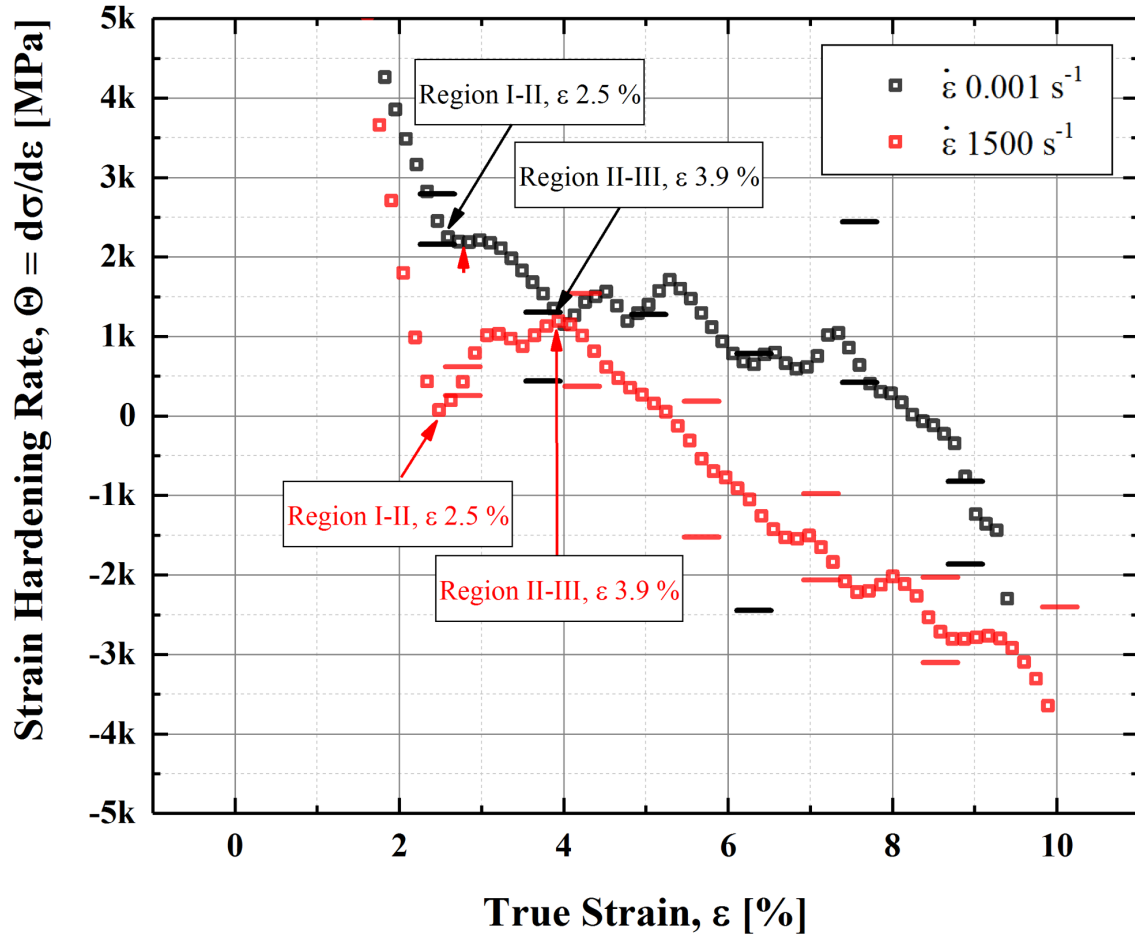


Figure 2-3 The strain hardening rate dependence on tensile ductility ($\Theta(\epsilon)$) identified the dominant deformation mechanism as elongation progress. As often reported for Ti and Ti alloys the Θ dependency on deformation is featured as a multi-stage curve [49]–[52].

Corresponding tension-overload fracture morphologies are presented by Figure 2-4.

Representative OM and SEM micrographs of the QS fractured tensile specimen are provided in Figure 2-4 a where the fracture surface of the specimens display the classic cup-and-cone failure mode. As illustrated in the OM light micrograph in Figure 2-4 a, the typical fractographic features, shear lips and rough flat central region, are present. The SEM analysis performed at the central region of the fracture surface reveals further details of the ductile fracture with equiaxed dimples exhibiting nearly-constant size distribution. Likewise, Figure 2-4 b illustrates the post-mortem analysis results for the specimen fractured at HR conditions. The OM micrograph

displays the fracture path oriented 45° to the plane of the tensile load (maximum shear plane). Since the direction of maximum shear stress with the respect to the loading axis coincides with the fracture path orientation, elongated dimples were observed on the SEM analysis in Figure 2-4 b thus suggesting shear mechanism.

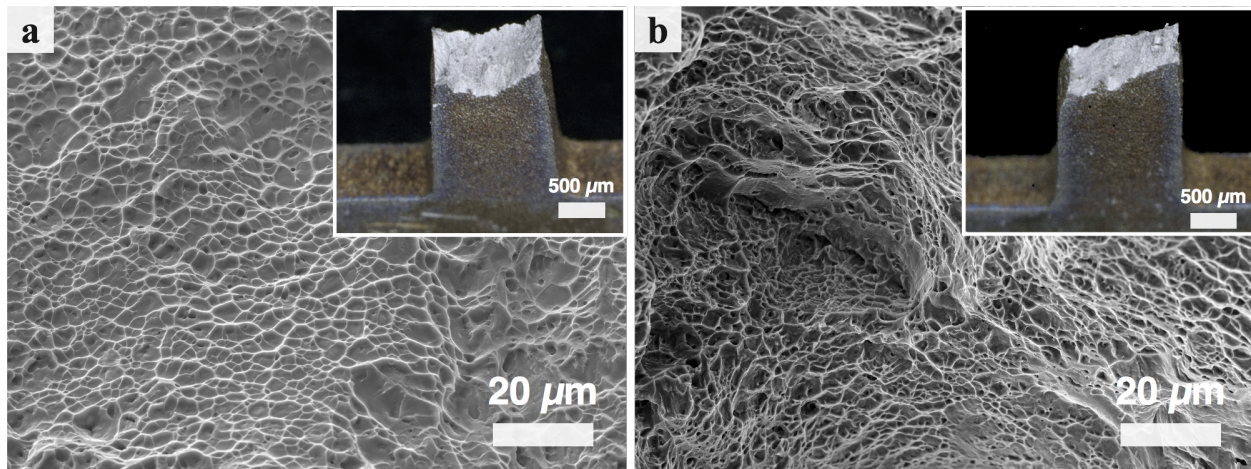


Figure 2-4 OM fractograph (a) depicts a cup-and-cone fracture topography for the quasistatically deformed ($\dot{\varepsilon} = 0.001 \text{ s}^{-1}$) uniaxial tensile specimen. As observed on the SE SEM micrograph the central zone fracture topography is characterized by equiaxed dimple rupture. The same fractographic analysis demonstrates the shear nature of the dynamic fractured specimen ($\dot{\varepsilon} = 1500 \text{ s}^{-1}$). OM micrograph presented at (b) shows that the fracture surface of the dynamic specimen is aligned with the maximum shear plane (45°). Shear dimples are observed on the SE SEM photomicrograph.

To capture the stress-state dependence of the Ti6Al4V material under investigation, uniaxial compression tests were performed at QS (0.001 s^{-1}) and HR (avg. 1000 s^{-1}) strain rate levels. Examination of the QS and HR compression curves (Figure 2-5) reveals that the effective flow stress increases dramatically with increasing strain rate. For the static-isothermal data set a σ_y equal to $1114 \pm 34.50 \text{ MPa}$ was calculated whereas $1549 \pm 38.95 \text{ MPa}$ was obtained for the HR compression specimens. The macroscopic compression responses also revealed a pronounced strain hardening behavior with an increase at higher deformation rates during an initial deformation period (strain levels below 4%).

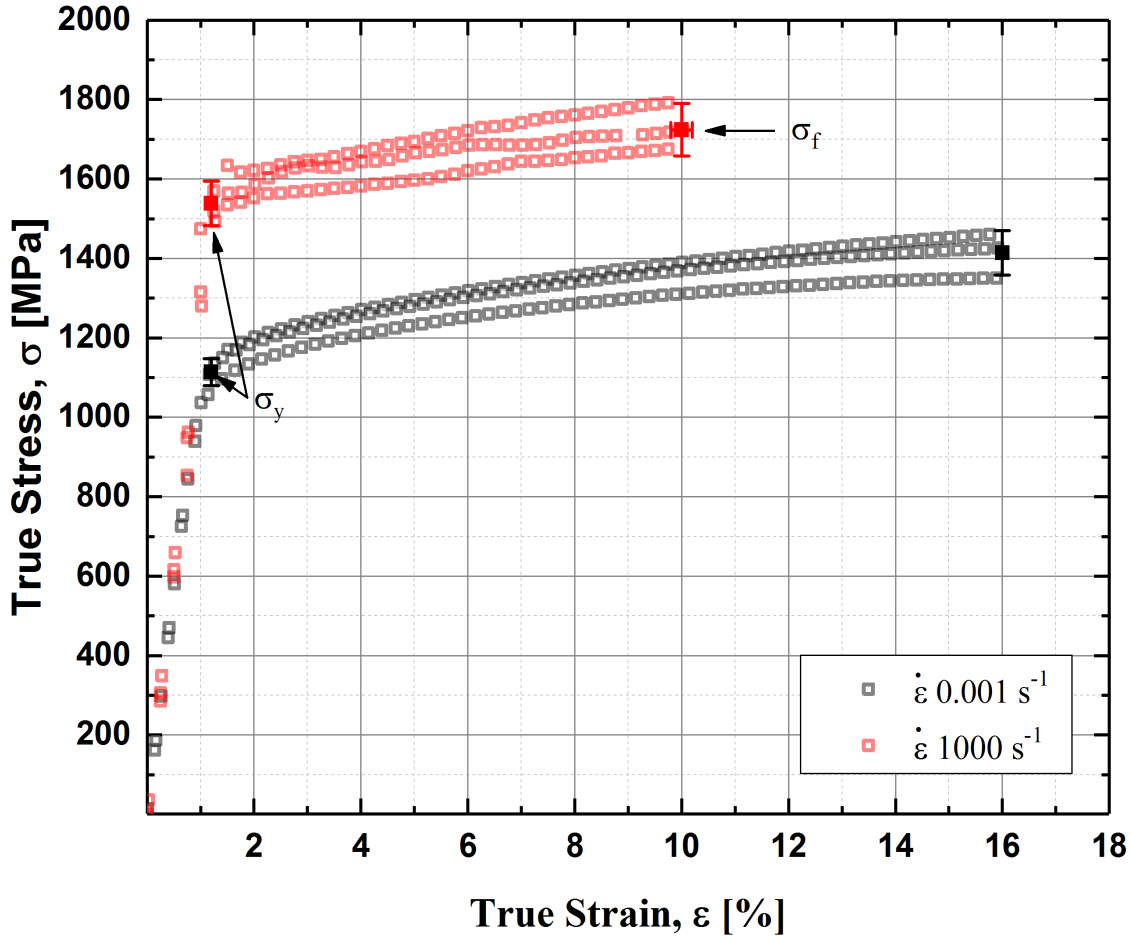


Figure 2-5 True stress – true strain flow curves for compression mode under different deformation rates ($\dot{\varepsilon} = 0.001$, and 1000 s^{-1}). At the macroscopic level compression results exhibit a rate sensitivity of the flow stress and prominent strain hardening.

The deformation nature of compression specimens was better appreciated in Θ curves (with associated error bars) plotted on Figure 2-6. On that regard, QS compression specimens had a strain hardening rate evolution that could be classified as a three-stage behavior with stage transitions at 3.6% and $7.5\% \varepsilon$ if a linear intercept method is adopted. Meanwhile, it should point out the pronounced stage transitions, and overall region behavior, of the strain hardening rate curve for the HR compression samples after Region I. At this point, the effect of the adiabatic thermal softening could be such that may reduce the apparent strain hardening. Therefore, the true isothermal hardening, and hardening rate, is higher than the values presented in Figure 2-6.

Moreover, after approximately $7\% \epsilon$, the material loses defect accumulation abilities (strain hardening capacity), which could be caused by dislocation annihilation at grain boundaries [51]. This observation provide evidence that dislocations provide the main contribution to strain. On the subject of failure (discuss in greater detail on a later section) Rittel and Wang's [7] thermomechanical studies under high rate conditions concluded that the flow stress stage after peak stress represents "heterogeneous deformation". After an initial stage (Stage I) were the plastic deformation is homogeneously distributed across the test article volume the deformation on Stage II is not strictly homogeneous, but it is not yet fully localized (as on ASB's). According to the authors, strain softening at Stage II is not necessarily thermal but may also indicate or result from a microstructural evolution. Stage III starting point, defined as the intersection of the empirical and experimental thermal curves, signals a fully formed ASB. Although in-situ thermal measurements were not performed on this study the interpretation of flow stress curves proposed by Rittel and Wang [7] was adopted. Hence, HR flow stress curves, as shown by Figure 2-5, are bounded to Stage I, where deformation is homogeneous. On that regard, peak strength for the HR specimens resulted in 1732 ± 48.08 MPa with a strain equals to $10.04 \pm 0.01\%$. Lastly, while average test fracture strength for the HR specimens are marked on the deformation curves QS compression test results are not reported to fracture since data was recorded to a fixed strain of 16%. Such strength magnitude for the QS samples was calculated to be 1414 ± 56.20 MPa whereas the fracture strength, here represented as the loss of load carrying capacity, for the HR specimens resulted in 1732 ± 48.08 MPa with a fracture strain equals to $10.04 \pm 0.01\%$.

Metallographic analysis in Figure 2-7 and Figure 2-8 illustrates the degree of structural damage sustained by a HR specimen that was tested but not fractured (no physical separation). The transverse section (parallel to the loading axis) morphology of the non-fractured HR

specimen in Figure 2-7 reveals the V-shaped adiabatic shear band (ASB) that propagated at an approximate 45° angle to the perpendicular plane of the specimen. Inset A depicts higher magnification SEM and Electron Backscatter Diffraction (EBSD) analyses of the ASB region in Figure 2-7. Per published literature [57], the unresolvable features of the material within the ASB are the results from rotational assisted dynamic recrystallization (DRX) mechanisms. The sequence of microstructural rearrangements leading to DRX in Ti6Al4V was previously investigated by Landau and collaborators [8]. As the deformation progressed, the material rearranged itself into cell-like structures with most dislocations residing in the cell walls while the interior remains relatively dislocation-free [54]. Interrogation of progressively closer regions to the ASB demonstrated that the cell size decreased and the cell boundaries become denser, i.e., the cells evolved to subgrains. Additionally, Landau [8] described the presence of DRX nanograins within an area comprised of avalanched dislocation cells (ASB). A schematic, illustrating the microstructural evolution process, is superimposed on the EBSD inset on Figure 2-7.

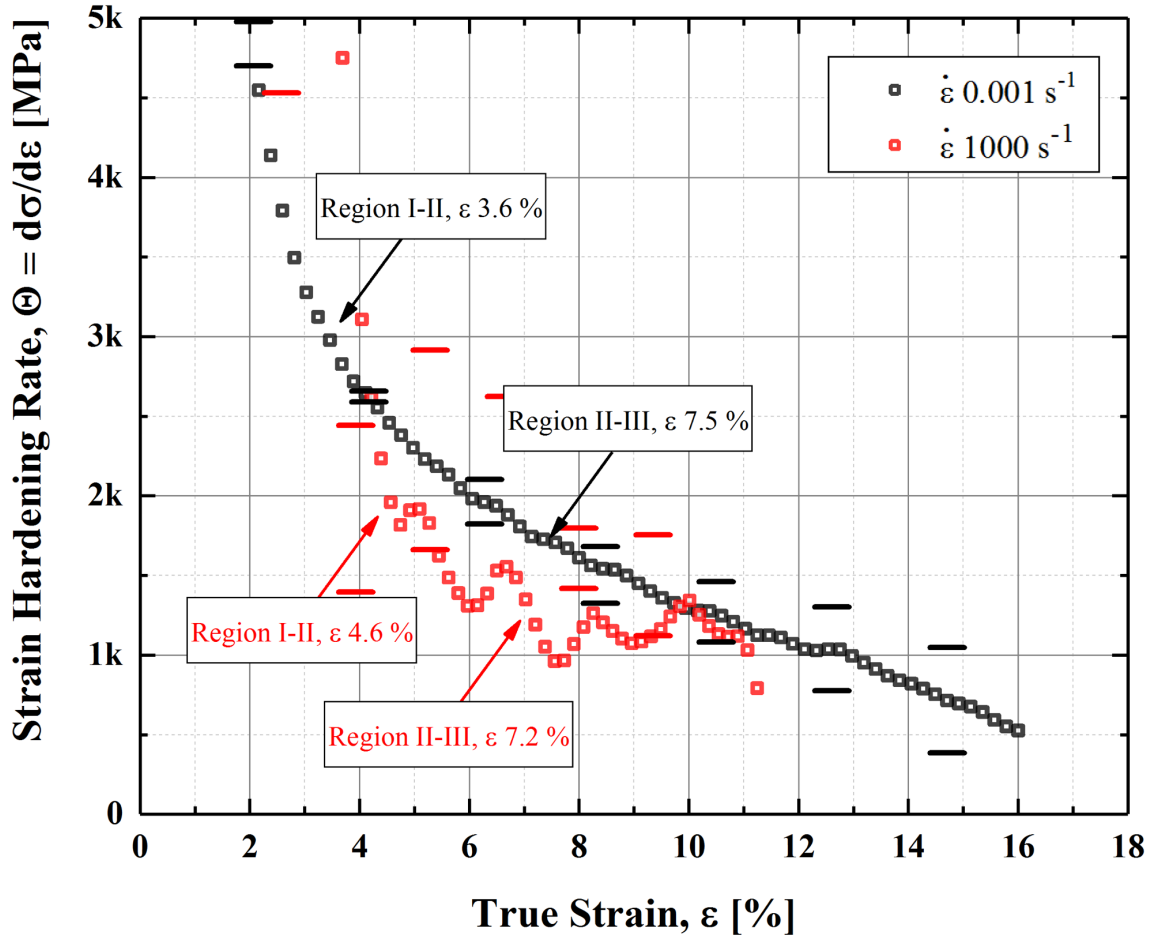


Figure 2-6 The strain hardening rate dependence on true compression strain ($\Theta(\varepsilon)$), maps the dominant deformation mechanisms as the contraction evolved. Notice that the progression of the static strain hardening rate follows a similar behavior that their tensile counterpart. Meanwhile, the strain hardening rate response of high rate compression specimens shows pronounced stage transitions.

As seen in Figure 2-7, microvoid nucleation, growth and coalescence occurs within the ASB region. Although, contrary to previous studies [8], [57], [58] microvoids did not grow to the full width of the band along the direction of the shear moment before coalescence for crack generation. Regarding the microstructure besides the ASB, intricate variants of Widmanstätten α -laths, which were shortened or elongated, due to severe localized deformation. Also, band bifurcation is shown on by the light micrograph.

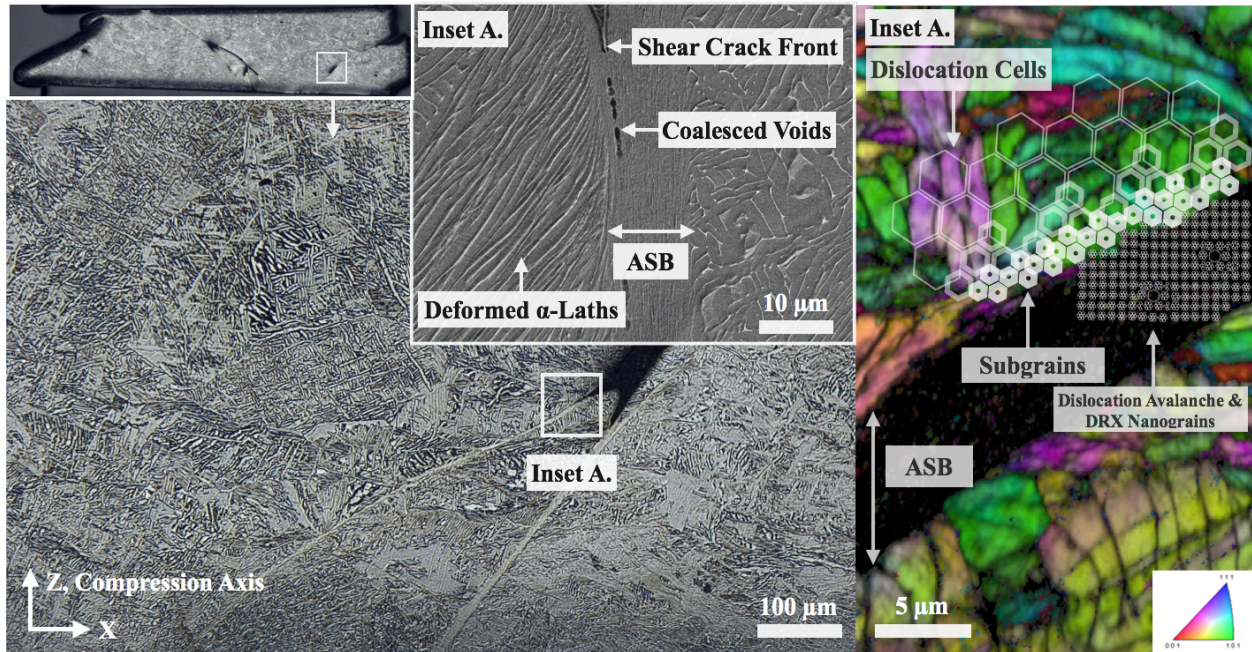


Figure 2-7 Low magnification OM metallographs illustrates the V-shaped ASB that propagated through a non-fractured HR compression sample. The transverse section morphology also reveals band bifurcation and intricate variants of Widmanstätten α -laths, which were shortened or elongated, due to severe localized deformation. Void coalescence and shear crack front are depicted by SE SEM's Inset A. Meanwhile, a not-to-scale schematic illustrating the microstructural evolution process, is superimposed on the EBSD inset. The grain orientations are represented by the color-coded Inverse Pole Figure (IPF) map.

The SEM image in Figure 2-8 details the fracture topography of the HR compression sample depicts the presence of shear dimples and smeared surfaces characteristic of a fracture along the shear plane. Similar fractographic features were observed by other investigators [3], [4], [58]. As concluded by Timothy and Hutchings [58] the ductile nature of the fracture topography is associated with the thermal softening arising from the adiabatic temperature rise. Recall that, as reported by Lia and Duffy [3], the temperature rise inside the sheared region lies within the 440-550 °C range.

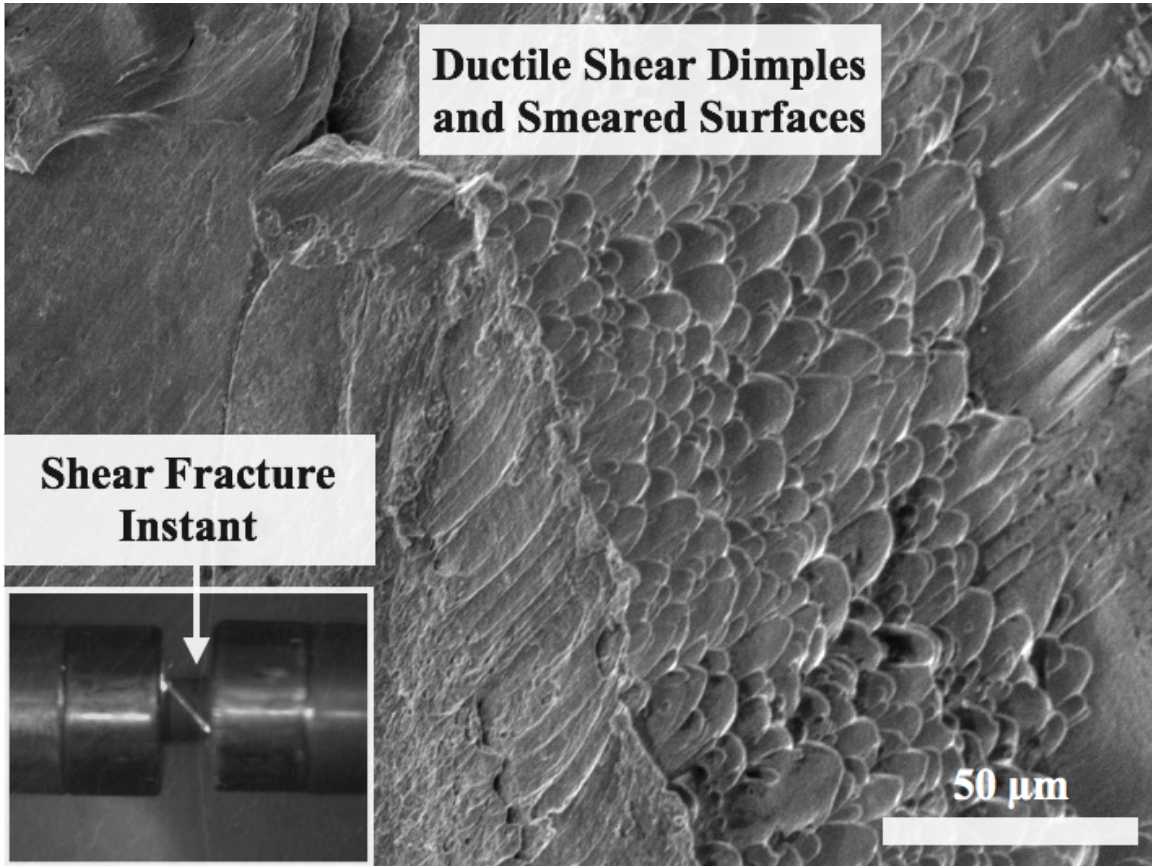


Figure 2-8 SE SEM micrograph illustrating the topography of a dynamically fractured ($\dot{\epsilon} = 1000 \text{ s}^{-1}$) compression specimen with ductile-shear dimples and smeared surface regions. The relatively smooth and smeared regions are products of the opposite surfaces rubbing. The inset shows a still frame of the high-speed fracture video (25 kfps). Notice light emission oriented diagonally with respect to the loading direction; this is an indication of ASB occurrence after peak stress was attained.

In Figure 2-9, the average experimental deformation curves show the level of asymmetry about the stress state. Recall that under tension, the initial yield stress was nearly insensitive to strain rate. Furthermore, while under tension, there was a sharp transition to the elasto-plastic regime at all rates, and with a very similar appearance to the single crystal behavior, substantial microplasticity occurred under compression. Both the absence of strain rate sensitivity under microplasticity under tension but not under compression indicate that the yield stress is controlled by slip under compression, and by twinning under tension. Except for $\{11\bar{2}2\}$ twin mode in Ti [59], twinning is in fact known to be athermal [60]–[64], and will only appear at

temperatures where pyramidal $\langle c + a \rangle$ slip becomes harder to activate (low temperatures and high rates). Under tension the alpha grains with $\langle c \rangle$ -axis closely parallel to the stress direction will be the first to plastically deform by virtue of their high Schmid's factor and low critical resolved shear stress (CRSS) for $\{10\bar{1}2\}$ twinning. In fact, Antonyamy [65] demonstrated that the basal planes of the alpha grains are mostly normal to the building direction. Thus, increasing the strain rates will not modify this behavior as the CRSS for twinning remains unchanged. However, those same grains will deform primarily by pyramidal slip under compression, while twinning activity will be minimalistic in the matrix, leaving off the flow stress to be dominated by non-basal slip. As such, the yield stress is generally higher under compression and will be very sensitive to strain rate with extended microplasticity. Microplasticity is another indication of slip dominance as texture allows for a broad variation of the Schmid's factors of active slip modes across all the grains. Also, note that this interpretation is consistent with the yield stress level which is generally higher in compression than tension, which is dominated by twinning having a lower CRSS.

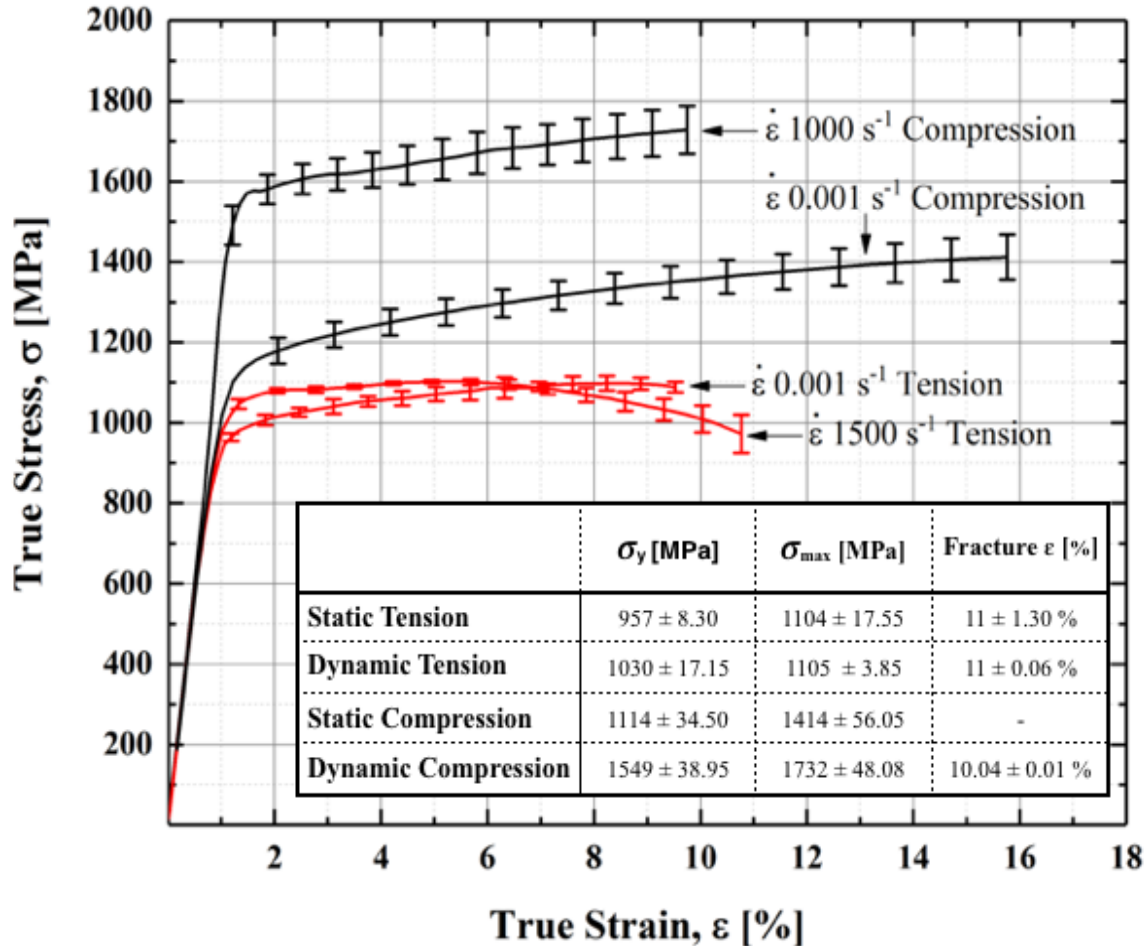


Figure 2-9 Averaged true stress vs true strain comparison of compression and tension results at both QS and HR. The macroscopic response curves show the asymmetry about the stress state increased as strain rate increased. The deformation rate effect on flow stress proves to be more pronounced in compression as expected. Also, strain hardening appeared increased at the lower QS loading rates. Uncertainty bands, representing the standard deviation, are included on the curves.

As seen in Figure 2-10 the resistance to plastic flow decrease with increasing temperature. It is also noted that the deformation temperature has a pronounced effect on hardening, a remarkable loss is observed with increasing temperature. This is an interesting result given the fact that the average strain rate also increases with testing temperature. When a material deforms under both, high temperature and high strain rate conditions its flow behavior is dictated by a competition process between the rates of strain hardening and thermal softening [66]. Generally, materials deformed under high strain rates experience an enhancement in

strength. On the contrary, an increase in temperature tends to reduce the resistance of flow stress by lowering the activation barriers associated with the atomic mechanism of deformation. Therefore, a reduction in strength and hardening rate is expected when the thermal softening becomes the dominant phenomena controlling the flow stress. On the present case, the true stress-true plastic strain relations (Figure 2-10) shows a decrease in flow stresses with increasing initial temperature (T_0) notwithstanding the increase in strain rate. Also notice that the curves with T_0 beyond 825 °C (hot working conditions) resembles an ideal plastic material (no strain hardening). This observation implies that at a microscopic level dislocation annihilation is occurring at a higher rate than its generation and reflected on a macroscopic level as microstructural changes due phase transformation.

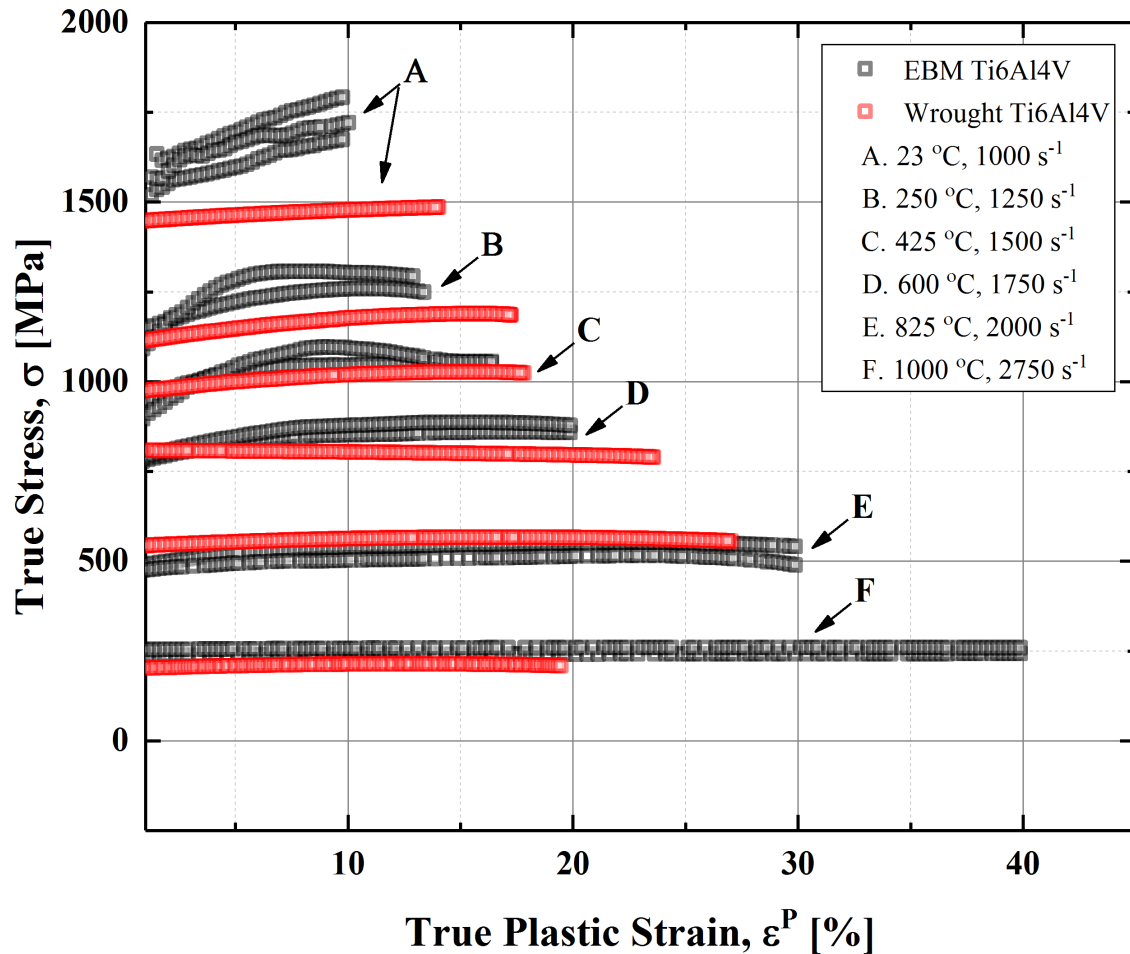


Figure 2-10 Macroscopic compression response at varying temperatures and strain rates suggest that the material's fundamental stress-strain behavior was dominated by the thermal phenomena (softening) rather than by strengthening associated with an increase in deformation rate. Fracture strain was not achieved on any of the tested specimens.

OM observations (Figure 2-11) attested the structural integrity after the deformation process. As expected, given the fact that no specimen reached its fracture strain, no ASB or ASB initiation site was observed. In terms of morphology, lamellar primary α , nonequilibrium needle-like martensitic α' and massive α (α_m) patches dominate the compressed Widmanst  ten microstructural landscape of specimens up to $600\text{ }^{\circ}\text{C}$ T_0 . Moreover, when the hot dynamic compression event is carried out near or above the β -transus temperature ($995\text{ }^{\circ}\text{C}$) the microstructural arrangement varies considerably. In the case of $825\text{ }^{\circ}\text{C}$ T_0 the microstructure is

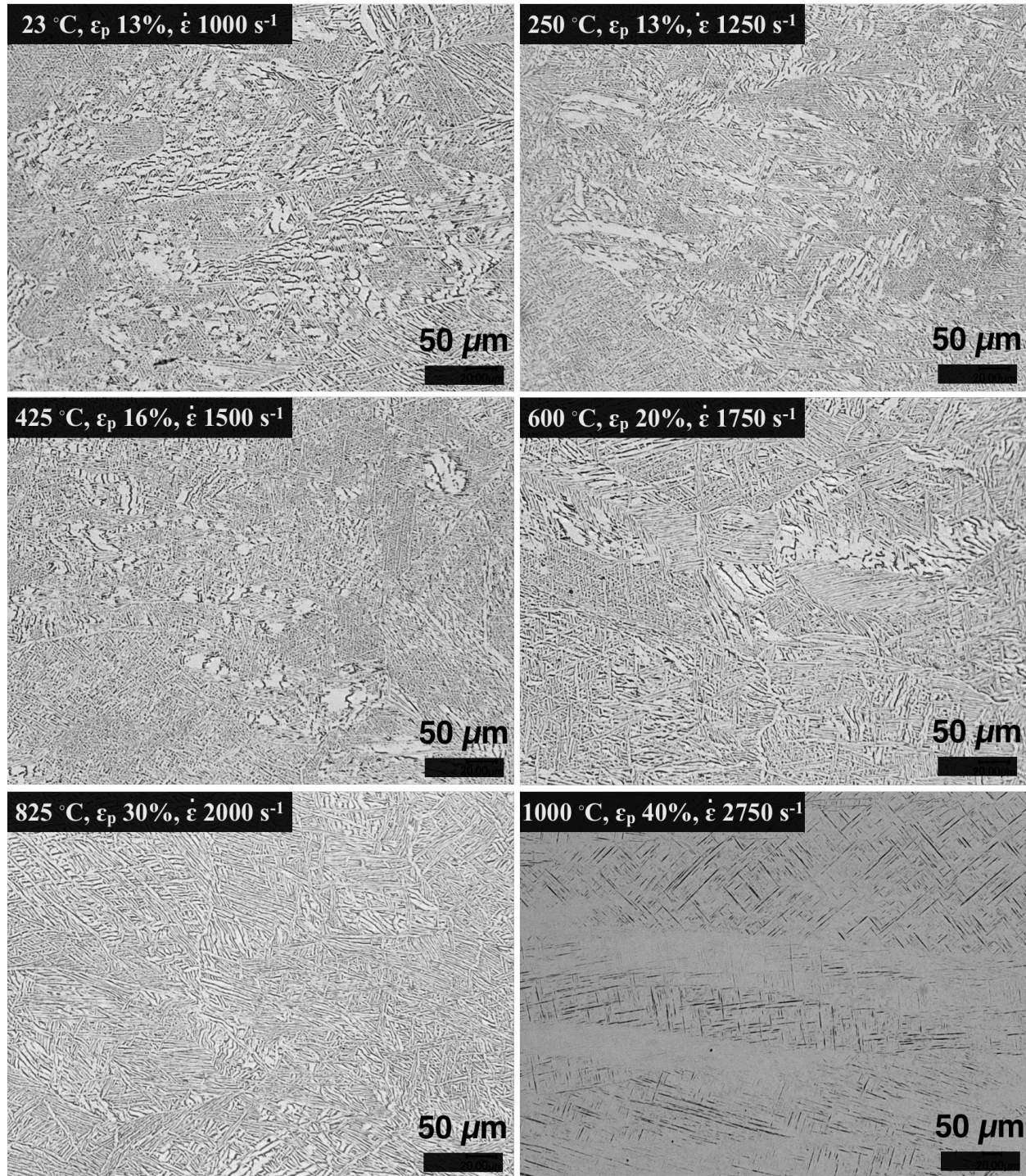


Figure 2-11 Bright field OM depict the structural damage sustained by the compression specimens tested under varying levels of temperature and strain rates. Neither fracture nor ASB initiation strains were achieved on any of the tested specimens.

2.4 Concluding Remarks

To conclude, the macroscopic flow stress response of an AM-EBM Ti6Al4V at varying stress states and deformation rates was coupled with its corresponding strain hardening rates and fracture morphologies with the goal to elucidate the underlying deformation mechanisms.

Specifically, the research identified the following:

1. While deformation rate effect on tensile flow stress is negligible, the influence is reflected on the fracture path and morphology. Fractography analyses revealed cup-and-cone fracture for the QS specimens and shear mechanisms on HR specimens.
2. Contrary to the tensile mode, cylindrical compression specimens flow stress results not only show sensitivity to deformation rate but also remarkable strain hardening. Moreover, ASB formation was identified with high-speed video of the fracture plane that correlated to SEM fractographic analysis of shear dimple formation. This microstructural feature has been reported on previous publications [4], [8], [10], [53], [67].
3. Deformation mechanisms were identified from close inspection of strain hardening rate curves. The contribution of dislocation glide and mechanical twinning as plasticity carriers was identified in stages and their relationship with deformation mode and rate was established.
4. Close inspection of elevated temperature – high rate flow stress data suggest that the thermal softening effect overrides the strengthening due to high strain rate deformation.

Microstructural transformations, especially those occurring in the hot working temperature range (825-1000 °C) requires future investigations.

By expanding on the first-tier mechanical properties library from this contribution and future investigations, the groundwork is being laid for the necessary criteria for alloy selection and data

necessary to develop and calibrate constitutive equations for physics-based material modeling of this additive material.

References

- [1] M. A. Meyers, G. Subhash, B. K. Kad, and L. Prasad, “Evolution of microstructure and shear-band formation in α -hcp titanium,” *Mech. Mater.*, vol. 17, no. 2–3, pp. 175–193, 1994.
- [2] M. G. da Silva and K. T. Ramesh, “The rate-dependent deformation and localization of fully dense and porous Ti-6Al-4V,” *Mater. Sci. Eng. A*, vol. 232, no. 1–2, pp. 11–22, 1997.
- [3] S. Liao and J. Duffy, “Adiabatic shear bands in a Ti-6Al-4V titanium alloy,” *J. Mech. Phys. Solids*, vol. 46, pp. 2201–2231, 1998.
- [4] S. Nemat-Nasser, W. G. Guo, V. F. Nesterenko, S. S. Indrakanti, and Y. B. Gu, “Dynamic response of conventional and hot isostatically pressed Ti-6Al-4V alloys: Experiments and modeling,” *Mech. Mater.*, vol. 33, no. 8, pp. 425–439, 2001.
- [5] W.-S. Lee and C.-F. Lin, “Plastic deformation and fracture behaviour of Ti-6Al-4V alloy loaded with high strain rate under various temperatures,” *Mater. Sci. Eng. A*, vol. 241, no. 1–2, pp. 48–59, 1998.
- [6] X. Liu, C. Tan, J. Zhang, F. Wang, and H. Cai, “Correlation of adiabatic shearing behavior with fracture in Ti-6Al-4V alloys with different microstructures,” *Int. J. Impact Eng.*, vol. 36, no. 9, pp. 1143–1149, 2009.
- [7] D. Rittel and Z. G. Wang, “Thermo-mechanical aspects of adiabatic shear failure of AM50 and Ti6Al4V alloys,” *Mech. Mater.*, vol. 40, no. 8, pp. 629–635, 2008.
- [8] P. Landau, a. Venkert, and D. Rittel, “Microstructural aspects of adiabatic shear failure in annealed Ti6Al4V,” *Metall. Mater. Trans. A Phys. Metall. Mater. Sci.*, vol. 41, no. 2, pp. 389–396, 2010.
- [9] C. Zheng *et al.*, “Capturing of the propagating processes of adiabatic shear band in Ti-6Al-4V alloys under dynamic compression,” *Mater. Sci. Eng. A*, vol. 658, pp. 60–67, 2016.
- [10] F. Martinez, L. E. Murr, a. Ramirez, M. I. Lopez, and S. M. Gaytan, “Dynamic deformation and adiabatic shear microstructures associated with ballistic plug formation and fracture in Ti-6Al-4V targets,” *Mater. Sci. Eng. A*, vol. 454–455, pp. 581–589, 2007.
- [11] N. Biswas, J. L. Ding, V. K. Balla, D. P. Field, and a. Bandyopadhyay, “Deformation and fracture behavior of laser processed dense and porous Ti6Al4V alloy under static and dynamic loading,” *Mater. Sci. Eng. A*, vol. 549, pp. 213–221, 2012.

- [12] P. Li, W. Guo, W. Huang, Y. Su, X. Lin, and K. Yuan, “Thermomechanical response of 3D laser-deposited Ti – 6Al – 4V alloy over a wide range of strain rates and temperatures,” *Mater. Sci. Eng. A*, vol. 647, pp. 34–42, 2015.
- [13] A. Mohammadhosseini, S. H. Masood, D. Fraser, and M. Jahedi, “Dynamic compressive behaviour of Ti-6Al-4V alloy processed by electron beam melting under high strain rate loading,” *Adv. Manuf.*, vol. 3, no. 3, pp. 232–243, 2015.
- [14] O. L. Rodriguez *et al.*, “Dynamic tensile behavior of electron beam additive manufactured Ti6Al4V,” *Mater. Sci. Eng. A*, vol. 641, pp. 323–327, 2015.
- [15] L. E. Murr *et al.*, “Microstructures and mechanical properties of electron beam-rapid manufactured Ti-6Al-4V biomedical prototypes compared to wrought Ti-6Al-4V,” *Mater. Charact.*, vol. 60, no. 2, pp. 96–105, 2009.
- [16] G. G. Yapici, I. Karaman, Z. P. Luo, and H. Rack, “Microstructure and mechanical properties of severely deformed powder processed Ti-6Al-4V using equal channel angular extrusion,” *Scr. Mater.*, vol. 49, no. 10 SPEC., pp. 1021–1027, 2003.
- [17] B. Baufeld, O. van der Biest, R. Gault, and K. Ridgway, “Manufacturing Ti-6Al-4V Components by Shaped Metal Deposition: Microstructure and Mechanical Properties,” *Mater. Sci. Eng.*, vol. 26, p. 12001, 2011.
- [18] J. T. Hammer, “Plastic Deformation and Ductile Fracture of Ti-6Al-4V under Various Loading Conditions,” The Ohio State University, 2012.
- [19] X. Gong, K. Chou, J. Lydon, and K. Cooper, “Characterization of Ti6Al4V Powder in Electron Beam Melting Additive Manufacturing,” *Int. J. Powder Metall.*, vol. 51, no. 1, 2015.
- [20] W. R. Whittington *et al.*, “Capturing the effect of temperature, strain rate, and stress state on the plasticity and fracture of rolled homogeneous armor (RHA) steel,” *Mater. Sci. Eng. A*, vol. 594, pp. 82–88, Jan. 2014.
- [21] P. G. Allison, H. Grewal, Y. Hammi, H. R. Brown, W. R. Whittington, and M. F. Horstemeyer, “Plasticity and Fracture Modeling/Experimental Study of a Porous Metal Under Various Strain Rates, Temperatures, and Stress States,” *J. Eng. Mater. Technol.*, vol. 135, no. 4, p. 41008, Sep. 2013.
- [22] P. G. Allison, M. F. Horstemeyer, Y. Hammi, H. R. Brown, M. T. Tucker, and Y.-K. Hwang, “Microstructure–property relations of a steel powder metal under varying temperatures, strain rates, and stress states,” *Mater. Sci. Eng. A*, vol. 529, pp. 335–344, Nov. 2011.
- [23] O. G. Rivera *et al.*, “Microstructures and mechanical behavior of Inconel 625 fabricated by

- solid-state additive manufacturing,” *Mater. Sci. Eng. A*, vol. 694, no. March, pp. 1–9, 2017.
- [24] S. Brauer *et al.*, “Strain rate and stress state dependence of gray cast iron,” *J. Eng. Mater. Technol.*, vol. 139, pp. 21013–1, 2017.
- [25] O. G. Rivera, Z. McClelland, W. R. Whittington, D. Francis, R. D. Moser, and P. G. Allison, “Interrupted Quasi-static and Dynamic Tensile Experiments of Fully Annealed 301 Stainless Steel,” in *2016 EPD Congress*, 2016, no. August 2014, pp. 165–172.
- [26] C. Weinong and S. BO, *Split Hopkinson (Kolsky) Bar*, vol. 1. 2013.
- [27] D. K. Francis, W. R. Whittington, W. B. Lawrimore, P. G. Allison, S. A. Turnage, and J. J. Bhattacharyya, “Split Hopkinson Pressure Bar Graphical Analysis Tool,” *Exp. Mech.*, vol. 57, no. 1, pp. 179–183, 2017.
- [28] T. J. Burns, S. P. Mates, R. L. Rhorer, E. P. Whitenton, and D. Basak, “Recent results from the NIST pulse-heated Kolsky bar,” *Proc. 2007 SEM Ann. Conf. Expo. Exp. Appl. Mech.*, no. January, p. paper 227, 2007.
- [29] L. E. Murr *et al.*, “Next-generation biomedical implants using additive manufacturing of complex, cellular and functional mesh arrays.,” *Philos. Trans. A. Math. Phys. Eng. Sci.*, vol. 368, pp. 1999–2032, 2010.
- [30] S. Al-Bermani, M. Blackmore, W. Zhang, and I. Todd, “The Origin of Microstructural Diversity, Texture, and Mechanical Properties in Electron Beam Melted Ti-6Al-4V,” *Metall. Mater. Trans. Part A*, vol. 41, no. 13, pp. 3422–3434, 2010.
- [31] S. M. Kelly, “Thermal and Microstructure Modeling of Metal Deposition Processes with Application to Ti-6Al-4V by,” Virginia Polytechnic Institute and State University, 2004.
- [32] L. Facchini, E. Magalini, P. Robotti, and A. Molinari, “Microstructure and mechanical properties of Ti-6Al-4V produced by electron beam melting of pre-alloyed powders,” *Rapid Prototyp. J.*, vol. 15, no. 3, pp. 171–178, May 2009.
- [33] A. Dehghan-Manshadi, M. H. Reid, and R. J. Dippenaar, “Effect of microstructural morphology on the mechanical properties of titanium alloys,” *J. Phys. Conf. Ser.*, vol. 240, p. 12022, 2010.
- [34] X. Gong, “Microstructural Characterization and Modeling of Ti6Al4V Parts Made By Electron Beam Additive Manufacturing,” The University of Alabama, 2014.
- [35] J. J. Lewandowski and M. Seifi, *Metal additive manufacturing: a review of mechanical properties*, vol. 46. 2016, pp. 151–186.
- [36] ASTM, “ASTM/ISO 52921: Standard terminology for additive manufacturing coordinate systems and test methodologies.” 2013.

- [37] S. Moylan and J. Slotwinski, “Assessment of Guidelines for Conducting Round Robin Studies in Additive Manufacturing,” in *ASPE Spring Tropical Meeting - Dimensional Accuracy and Surface Finish in Additive Manufacturing*, 2014, vol. 57, pp. 82–85.
- [38] S. Moylan, J. Land, and A. Possolo, “ADDITIVE MANUFACTURING ROUND ROBIN PROTOCOLS: A PILOT STUDY,” in *Solid Freeform Fabrication Proceedings*, 2015, pp. 1504–1512.
- [39] B. Dutta and F. H. Froes, “The additive manufacturing (AM) of titanium alloys,” in *Titanium powder metallurgy: science, technology and applications*, Elsevier Inc., 2015, pp. 447–468.
- [40] W. J. Sames, F. A. List, S. Pannala, R. R. Dehoff, and S. S. Babu, “The metallurgy and processing science of metal additive manufacturing,” *Int. Mater. Rev.*, vol. 6608, no. March, 2016.
- [41] P. Edwards, A. O’Conner, and M. Ramulu, “Electron Beam Additive Manufacturing of Titanium Components: Properties and Performance,” *J. Manuf. Sci. Eng.*, vol. 135, no. 6, 2013.
- [42] U. Ackelid and M. Svensson, “Additive Manufacturing of Dense Metal Parts by Electron Beam Melting,” in *Proceedings from the Materials Science & Technology Conference*, 2009.
- [43] S. L. Lu, H. P. Tang, Y. P. Ning, N. Liu, D. H. StJohn, and M. Qian, “Microstructure and Mechanical Properties of Long Ti-6Al-4V Rods Additively Manufactured by Selective Electron Beam Melting Out of a Deep Powder Bed and the Effect of Subsequent Hot Isostatic Pressing,” *Metall. Mater. Trans. A*, vol. 46, no. 9, pp. 3824–3834, 2015.
- [44] K. Rekedal and D. Liu, “Fatigue Life of Selective Laser Melted and Hot Isostatically Pressed Ti-6Al-4v Absent of Surface Machining,” in *56th AIAA/ASCE/AHS/ASC Structures, Structural Dynamics, and Materials Conference*, 2015.
- [45] D. Greitemeier, C. D. Donne, F. Syassen, J. Eufinger, and T. Melz, “Effect of surface roughness on fatigue performance of additive manufactured Ti-6Al-4V,” *Mater. Sci. Technol.*, vol. 32, no. 7, pp. 629–634, 2016.
- [46] P. Edwards, a. O’Conner, and M. Ramulu, “Electron Beam Additive Manufacturing of Titanium Components: Properties and Performance,” *J. Manuf. Sci. Eng.*, vol. 135, no. December 2013, p. 61016, 2013.
- [47] M. Simonelli, Y. Y. Tse, and C. Tuck, “Effect of the build orientation on the mechanical properties and fracture modes of SLM ti-6Al-4V,” *Mater. Sci. Eng. A*, vol. 616, pp. 1–11, 2014.
- [48] C. Qiu, N. J. E. Adkins, and M. M. Attallah, “Microstructure and tensile properties of

- selectively laser-melted and of HIPed laser-melted Ti–6Al–4V,” *Mater. Sci. Eng. A*, vol. 578, pp. 230–239, Aug. 2013.
- [49] F. Coghe, W. Tirry, L. Rabet, D. Schryvers, and P. Van Houtte, “Importance of twinning in static and dynamic compression of a Ti-6Al-4V titanium alloy with an equiaxed microstructure,” *Mater. Sci. Eng. A*, vol. 537, pp. 1–10, 2012.
- [50] H. Becker and W. Pantleon, “Work-hardening stages and deformation mechanism maps during tensile deformation of commercially pure titanium,” *Comput. Mater. Sci.*, vol. 76, pp. 52–59, 2013.
- [51] A. Roth, M. A. Lebyodkin, T. A. Lebedkina, J. S. Lecomte, T. Richeton, and K. E. K. Amouzou, “Mechanisms of anisotropy of mechanical properties of alpha-titanium in tension conditions,” *Mater. Sci. Eng. A*, vol. 596, pp. 236–243, 2014.
- [52] K. Ahn, H. Huh, and J. Yoon, “Rate-dependent hardening model for pure titanium considering the effect of deformation twinning,” *Int. J. Mech. Sci.*, vol. 98, pp. 80–92, 2015.
- [53] D. R. Chichili, K. T. Ramesh, and K. J. Hemker, “The high-strain-rate response of alpha-titanium: experiments, deformation mechanisms and modeling,” *Acta Mater.*, vol. 46, no. 3, pp. 1025–1043, 1998.
- [54] Y. Hao, X. X. Wu, X. Y. San, S. Li, and X. K. Zhu, “The influence of stacking fault energy on compression test of Cu and Cu-Al alloys,” *Procedia Eng.*, vol. 36, pp. 307–315, 2012.
- [55] G. P. Dinda, L. Song, and J. Mazumder, “Fabrication of Ti-6Al-4V scaffolds by direct metal deposition,” *Metall. Mater. Trans. A Phys. Metall. Mater. Sci.*, vol. 39, no. 12, pp. 2914–2922, 2008.
- [56] W. Zhou and K. G. Chew, “The rate dependent response of a titanium alloy subjected to quasi-static loading in ambient environment,” *J. Mater. Sci.*, vol. 37, no. 23, pp. 5159–5165, 2002.
- [57] Q. Xue, M. a. Meyers, and V. F. Nesterenko, “Self-organization of shear bands in titanium and Ti-6Al-4V alloy,” *Acta Mater.*, vol. 50, pp. 575–596, 2002.
- [58] S. P. Timothy and I. M. Hutchings, “The Structure of Adiabatic Shear Bands in a Titanium Alloy,” *Acta Metall.*, vol. 33, no. 4, pp. 667–676, 1985.
- [59] N. E. Paton and W. Backofen, “Plastic deformation of titanium at elevated temperatures,” *Metall. Mater. Trans. B*, vol. 1, no. 10, pp. 2839–2847, 1970.
- [60] A. Jain and S. Agnew, “Modeling the temperature dependent effect of twinning on the behavior of magnesium alloy AZ31B sheet,” *Mater. Sci. Eng. A*, vol. 462, no. 1–2, pp. 29–36, 2007.
- [61] L. Jiang, J. J. Jonas, A. A. Luo, A. K. Sachdev, and S. Godet, “Influence of {10-12}

extension twinning on the flow behavior of AZ31 Mg alloy,” *Mater. Sci. Eng. A*, vol. 445, pp. 302–309, 2007.

- [62] L. Jiang, J. Jonas, R. Mishra, A. Luo, A. Sachdev, and S. Godet, “Twinning and texture development in two Mg alloys subjected to loading along three different strain paths,” *Acta Mater.*, vol. 55, no. 11, pp. 3899–3910, 2007.
- [63] L. Li, J. Zhou, and J. Duszczyk, “Determination of a constitutive relationship for AZ31B magnesium alloy and validation through comparison between simulated and real extrusion,” *J. Mater. Process. Technol.*, vol. 172, no. 3, pp. 372–380, 2006.
- [64] G. Liu, J. Zhou, and J. Duszczyk, “Prediction and verification of temperature evolution as a function of ram speed during the extrusion of AZ31 alloy into a rectangular section,” *J. Mater. Process. Technol.*, vol. 186, no. 1–3, pp. 191–199, 2007.
- [65] A. A. Antonyamy, “Microstructure, texture and mechanical property evolution during additive manufacturing of Ti6Al4V alloy for aerospace applications,” 2012.
- [66] W.-S. Lee and C.-F. Lin, “High-temperature deformation behaviour of Ti6Al4V alloy evaluated by high strain-rate compression tests,” *J. Mater. Process. Technol.*, vol. 75, pp. 127–136, 1998.
- [67] M. a. Meyers, V. F. Nesterenko, J. C. LaSalvia, and Q. Xue, “Shear localization in dynamic deformation of materials: Microstructural evolution and self-organization,” *Mater. Sci. Eng. A*, vol. 317, no. 1–2, pp. 204–225, 2001.

CHAPTER 3 INFLUENCE OF THERMAL POST-PROCESSES ON MORPHOLOGY AND TENSILE RESPONSE OF INCONEL 718 FABRICATED BY SELECTIVE LASER MELTING ADDITIVE MANUFACTURING

Omar L. Rodriguez¹, Paul G. Allison^{1*}, Lin Li², Sharniece Holland² Omar Mireles³, Johnathan Woolley³ and Joshua McKinley⁴

¹ The University of Alabama, Department of Mechanical Engineering, Tuscaloosa, AL, 35487

² The University of Alabama, Department of Metallurgical and Materials Engineering, Tuscaloosa, AL, 35487

³ NASA Marshall Space Flight Center, Huntsville, AL, 35812

⁴ The University of Alabama, Department of Mechanical Engineering, Huntsville, AL, 35899

* Corresponding Author: pallison@eng.ua.edu

Keywords: Additive Manufacturing, Selective Laser Melting, INCONEL 718, High Strain Rate, Thermal Post-Processing

Abstract

The influence of a sequential, standard, thermal post-processing treatment on the morphology and tensile performance of a Selective Laser Melting (SLM) INCONEL 718 (IN718) was investigated. Examinations of the microstructural evolution revealed an orientation dependent columnar, melt-pool-dominated morphology with powder-induced voids on its as-build state. Test articles subjected to a complete standardized thermal post-process routine, involving stress relief, hot isostatic pressing and homogenization and precipitation steps, exhibited scarce spherical porosity and an isotropic microstructural distribution. Quasi-static and high rate tensile experiments examined strain rate dependence on flow stresses. As normally expected from a polycrystalline metallic material system, strength increase at the expense of elongation to failure

with increasing deformation rates. The improvement in strength was attributed to the precipitation of strengthening phases.

3.1 Introduction

Nickel-based superalloys are metallic materials of high technical importance due to their unique properties: outstanding magnetic behavior (variable or constant magnetic permeability), wear resistance and corresponding anti-friction properties, and practically zero expansion coefficient in the 0 - 100°C (approx.) temperature range [1]. In particular, the IN718 system, an austenitic nickel-chromium based superalloy, has attracted increasing attention due to its excellent creep properties, oxidation resistance, and high temperature corrosion resistance [2]. Moreover, by virtue of precipitation strengthening mechanism – i.e. D0₂₂- ordered γ'' (Ni₃Nb) and L12-ordered γ' (Ni₃(Al,Ti)) phases in the γ matrix – IN718 is capable of retaining its superior mechanical properties in a broad range of temperatures [3]. Summing these behaviors results in nickel-based superalloys as common materials used in a variety of applications such as aircraft gas turbines (e.g. disks, combustion chamber, casings, shafts, exhaust system, blades, vanes, burner, cans, stack gas reheaters), reciprocating engines (e.g. turbochargers, exhaust valves hot plugs, valve seat inserts), metal processing (e.g. hot work tools and dies), space vehicles (e.g. aerodynamically heated skins, rocket engine parts) heat treating equipment (e.g. trays, fixtures, conveyor belts, baskets, fans, furnace mufflers), nuclear power plants, chemical and petrochemical industries and heat exchangers [4].

IN718 superalloy ingots and components are usually processed via conventional melting and casting methods. Nevertheless, segregation of high-concentration refractory elements such as Nb and Mo lead to issues, such as macro-segregation, that in-turn, adversely influence the

performance by inducing a large variation on mechanical properties. Suitable heat treatments have been developed to eradicate elemental segregation and precipitate strengthening phases, however, segregation seems to be unavoidable [5]. Conversely, as trending in scientific publications, Additive Manufacturing (AM) approaches, particularly powder bed fusion (PBF) platforms, are currently investigated as a prospective candidate to complement or replace conventional IN718 production processes [6]–[11].

Selective Laser Melting (SLM), a PBF process, can fabricate components with complex geometrical arrangements while maintaining a high build density with dimensional accuracy [12]. Yet, given the high temperature gradients and rapid solidification rates, the precipitation of strengthening phases is inhibited, thus, leading to a decrease in mechanical strengths. Likewise, the existence of thermal stress also makes the material unstable. Consequently, further post-process heat treatments are required to optimize the microstructure and improve mechanical performance.

Although many aspects of SLM manufacturing of IN718 have been investigated, information on suitable post-manufacturing procedures to improve the microstructure and reduce the inherent anisotropy is still needed. In the present work, preliminary findings on the microstructural changes of the SLM-printed IN718 are reported. This includes the changes in the microstructural arrangements and quasi-static (QS) and high strain rate (HR) tensile strengths (σ_y and UTS) and ductility of IN718 specimens that were exposed to a sequential post-process of Stress Relief (SR), Hot Isostatic Press (HIP), and Solution Treated and Aged (STA). The documentation of such data is a critical tool for the optimized design of the SLM process of superalloys, as well as developing the information necessary to calibrate and validate the constitutive equations used in material models.

3.2 Experimental Procedures

An EOS M 290 (EOS, Kralling, Germany) Yb-fiber laser system with modified rake blades located at NASA MSFC was used to fabricate the samples for this study. The SLM process physical descriptors (laser power, scanning speed, hatch distance, etc.) used for fabricating test coupons are EOS standard fusion parameters under argon atmosphere. A bidirectional raster strategy, with a 67° difference between layers, was employed. The building platform was preheated, and maintained, to 80°C to reduce the thermal gradient between platform/substrate and printed geometry. Fine, pre-alloyed commercially available IN718 powder (Carpenter Powder Products) with nominal particle diameter within the $10\text{-}45 \mu\text{m}$ range and elemental composition (wt.%) of 54.7% Ni, 18.3% Cr, 18.9% Fe, 4.6% Nb, 2.0% Mo, and 0.8 Ti (wt.%) was used for this investigation. The H-shaped, sub-standard sized tensile coupons previously used for both QS and HR tensile experiments on cast, wrought, and AM alloys [13]–[15] ($gl = 4.50 \text{ mm}$, $w = 2.30 \text{ mm}$ and $t = 1.50 \text{ mm}$) were machined from printed blocks with their loading axis parallel to build orientation. Test articles were sequentially heat treated per Society of Automotive Engineers Aerospace Material Systems (SAE AMS) 5664E specifications after SR and HIP post-processes [5]. For clarity purposes, the thermal post-processing sequential steps are specified in Table 3-1.

To quantify the deformation rate and stress state influence on flow stress, a series of uniaxial tensile experiments were performed on specimens after each post-process step. For each series, three specimens were tested. An MTS Landmark servohydraulic load frame equipped with a 25 kN load cell performed the quasi-static tension experiments on sub-standard sized specimens. An optical extensometer technique previously used for subcompact specimens was employed to capture axial displacement [16], [17]. Dynamic tension experiments were

performed with a IN718 tension-compression Kolsky bar recovery apparatus ($\phi = 13.0$ mm). Aluminum pulse shapers ($t = 0.10$ mm) were used to eliminate the Pochhammer-Chree oscillations in the incident pulse as suggested by previous researchers [18]. Strain metrology data, obtained using semiconductor strain gages cemented on the bars, was processed by the Split Hopkinson Pressure Bar Graphical Analysis Tool open-source MATLAB® code [19].

Table 3-1 Thermal Post-Processes: SLM IN718 Test Articles

Thermal Post-Process	Parameters
Stress Relief (SR)	Vacuum atmosphere $1065.5^{\circ}\text{C} \pm 25^{\circ}\text{C}$ for 1.5 hours, -5/+15 minutes, furnace cool with venting air.
Hot Isostatic Press (HIP)	$1163^{\circ}\text{C} \pm 25^{\circ}\text{C}$, $102 \text{ MPa} \pm 1.72 \text{ MPa}$, 3-4 hours, -0/+15 minutes, air cool.
Solution Treated and Aged (STA)	<u>Solution Treatment:</u> $1065.5^{\circ}\text{C} \pm 25^{\circ}\text{C}$ for a time commensurate with cross-sectional thickness, argon purge cool at a rate equivalent to air cool. <u>Aging Treatment:</u> $760^{\circ}\text{C} \pm 15^{\circ}\text{C}$ for 10 hours ± 30 minutes, furnace cooling to $650^{\circ}\text{C} \pm 15^{\circ}\text{C}$, hold at $650^{\circ}\text{C} \pm 15^{\circ}\text{C}$ until a total precipitation heat treatment time of 20 hours, argon purge quench.

Stress relief (SR) and hot isostatic (HIP) processes are required per NASA MSFC-SPEC-3717 [20] and ASTM standard [21]. Solution and precipitation heat treatments (STA) in accordance with SAE AMS 5664E specifications [5].

IN718 samples were prepared for microstructural observations with standard metallographic procedures including sectioning, mounting, grinding. Specimens for microstructural evaluation were etched in waterless Kalling's with an etching time of 60 s. Both, ZEISS SmartZoom 5 series digital microscope and a Hitachi S-3700N SEM were used for microstructural and fractography analyses.

3.3 Results and Discussion

Considering the stringent requirements for minimizing defects in the aerospace industry, a detailed understanding of grain structure evolution in each of these heat treatment paths is essential. Firstly, the build process results in a complex and highly stressed microstructure. For instance, as seen on Figure 3-1a, the alternating raster strategy of the SLM process formed a complex spatial topological structure by overlapping the tracks and layers molten pools. Melt pools are identified on the surface topography in Figure 3-1a as Gaussian-shaped ($w = 118.63 \pm 39.39 \mu\text{m}$) arrangements containing fine columnar grains, parallel to the building direction, that extend across multiple deposited layers. Correspondingly, the effect of the contour scan, done after infill melting scan to refine surface finish [22], on the bulk microstructure is also depicted by Figure 3-1a. Here, small grains within a thin layer of partially melted powder attached to the wall surface from which fine inward-growing curved-columnar grains develop as far as the centerline of the contour pass. As stated by Sames and coworkers on a comprehensive review article [8]: “*solidification determines the initial phase distribution and grain morphology of the metal deposit while heat source speed, power and size determine melt pool geometry, which in turn determines solidification kinetics*”. For a detailed analysis of influence of solidification kinetics and process parameters physical descriptors on the as-built morphology readers are referred to [23]–[26]. Finally, scarce microvoids (powder-induced porosity) were observed along the building direction.

The SR treatment has two primary objectives: begin the recrystallization of the as-built microstructure and prevent built-up residual stresses from affecting the geometric tolerances of the part during removal from the build platform. As shown in Figure 3-1b, partial recrystallization promoted the nucleation of nearly-equiaxed grains from columnar-oriented

structures. Previous publications identified thermal residual stresses, accumulated from the cyclic rapid heating and cooling schemes associated to the SLM process, as the driving force for partial recrystallization [8], [27], [28]. For instance, Liu and coworkers [27] revealed that the uneven distribution of grains results from the equally inhomogeneous distribution of residual stress. Consequently, the higher residual stress values within melt pool overlapping regions offer a greater driving force for recrystallization and leads to a finer grain size; whereas the grain size in adjacent areas are coarser due to the smaller driving forces (residual stresses). It is also noted (Figure 3-1b) that the grain morphology presents a significant difference in vertical and horizontal sections, which may lead to anisotropy on mechanical properties. Similar observations on partial recrystallization of SLM materials after a SR treatment are documented by other investigators [29]–[31].

In addition to close internal volumetric defects, the HIP process, illustrated by Figure 3-1c, significantly altered the grain structure of SLM IN718. When compared against the as-built and SR microarchitectures, the dendritic microstructure is replaced with an isotropic-distribution, nearly ellipsoid shaped recrystallized grain structures, needle-like precipitates, and scarce low-circularity porosity. As found in published literature [9], the aforementioned precipitates are incoherent Ni_3Nb δ -phase. Lastly, the purpose of homogenization or solution heat treatment is to dissolve segregation particles into the γ matrix whereas precipitation (aging) treatment is intended to precipitate the strengthening phases (γ' and γ'') [28], [32]. In terms of morphology, it bears a close resemblance with the HIPed microstructure albeit larger grains can be observed.

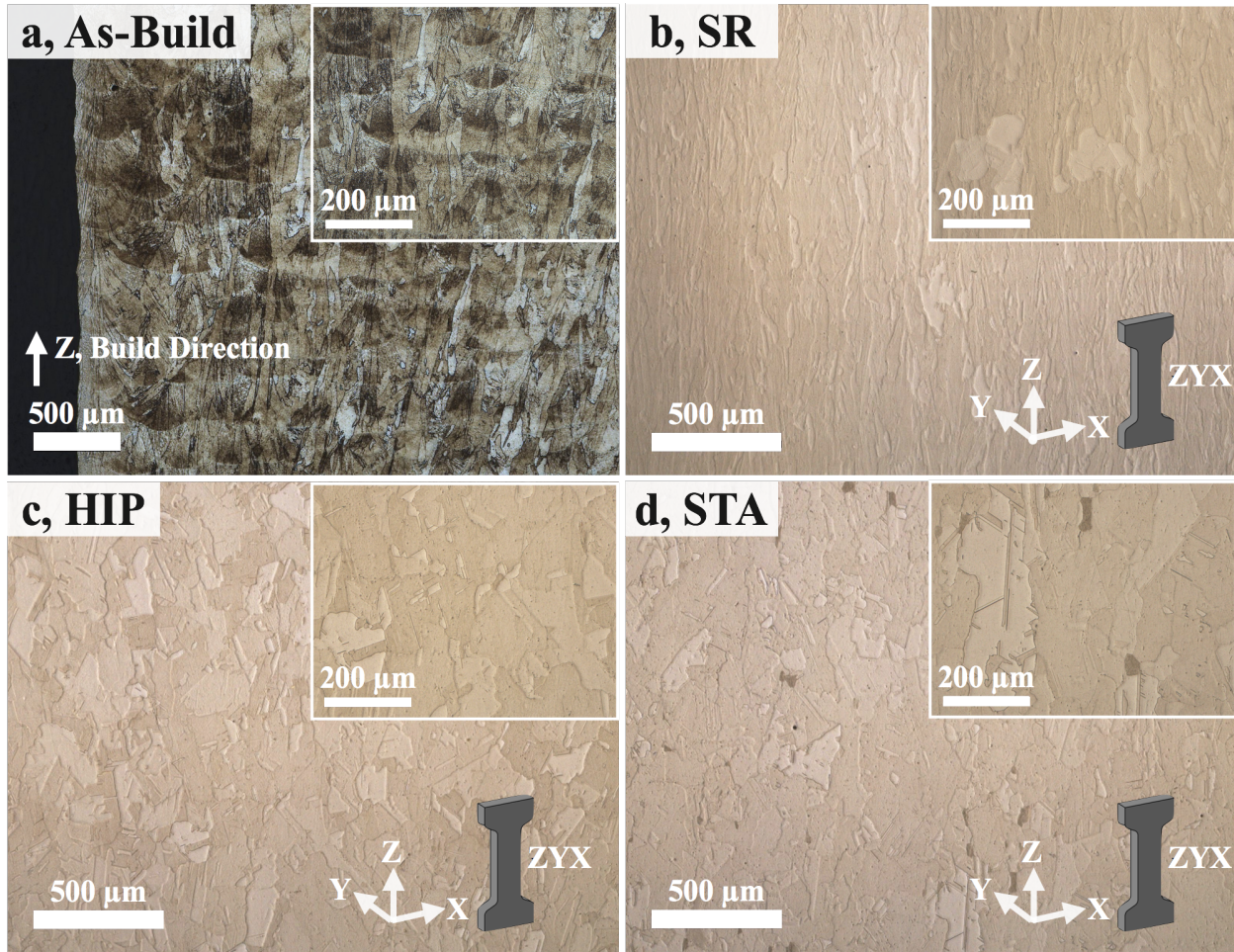


Figure 3-1 As depicted (a) the alternating raster strategy of the SLM IN718 process formed a complex spatial topological structure by overlapping multiple track layer molten pools. In order to alleviate residual stress, repair volumetric defects and spherical microdefects and precipitate strengthening phases, test articles were exposed to a progressive post-processing schedule (b-d) in agreement with specifications and standards for AM aerospace alloys (MSFC-SPEC-3717, ASTM and SAE AMS 5664E) [5], [21].

Room temperature, QS ($\dot{\epsilon} 0.001 \text{ s}^{-1}$) and HR ($\dot{\epsilon} 2000 \text{ s}^{-1}$) plastic flow tensile curves are presented by Figure 3-2. The SAE AMS specification values for cast (SAE AMS 5383) and wrought (SAE AMS 5362) IN718 are included as a reference [33], [34]. Broadly stated, yield (σ_y) and ultimate tensile (UTS) strengths increase with each sequential post-processing step while a decrease on elongation to failure (ϵ_f) was observed. As for strain rate effect, higher strengths and lower ductility values were recorded with increasing deformation velocity.

To begin with, QS, as-built inelastic curves, were tensile tested along the deposition direction. The continuous grain boundaries covering many deposited layers would not effectively inhibit the proceeding of deformation, leading to the low strength values ($\sigma_y = 696 \pm 11.95$ MPa, UTS = 1251 ± 6.12 MPa) and high ductility (23.50 ± 0.80 %) [31], [35]. In addition, the presence of volumetric defects, acting as crack initiation sites, further limits the overall tensile performance. Interestingly, although cast and wrought σ_y values outperformed SLM tensile articles (758, 1034 and 696 ± 11.95 MPa, respectively) SLM UTS results nearly matched the wrought superior performance (1251 ± 6.12 and 1276 MPa respectively). It should be mentioned that the QS as-built tensile results presented in Figure 3-2 were provided by NASA MSFC EM10 Mechanical Test Facilities. Furthermore, those test coupons were tested in accordance with ASTM E8 standard [36], i.e., standard-sized specimens were used. At the time of writing no additional tensile specimens have been supplied by NASA MSFC, consequently, no QS and HR, as-built, substandard-sized tensile results can be presented in Figure 3-2.

Compared with the as-built specimens, a considerable improvement in strength (σ_y and UTS) was observed after each post-process step. In the STA case, as depicted in Figure 3-2, σ_y improved by 72% while UTS values increased by 22% when compared to the as-built condition. The improvement in strength is attributed to precipitation of the γ' and γ'' strengthening phases and needle-like incoherent δ -phase [28], [31], [37]. As the researchers reported [28], dispersively distributed strengthening phases cause dislocation pinning and impede their movement, therefore the dislocation density is higher than the as-fabricated specimens. With an increase in piled-up dislocations, the driving force for dislocation motion is increase and finally able to cut through the strengthening phases and keep moving until they encounter acicular δ phases. Since the δ phases remain an incoherent relationship with the matrix and can contain little plastic

deformation, which will become crack sources and promote crack propagation, the dislocation motion will terminate in δ phases and develop into a ductile dimpled fracture.

In this context, Table 3-2 shows the quasi-static tensile strength dependence on loading direction and thermal post-process. In agreement with the current study, researchers observed an enhancement in tensile strength values (σ_y and UTS) and a decrease in ε_f on post-processed test coupons therefore demonstrating the importance of establishing processing parameters-microstructure-performance correlations.

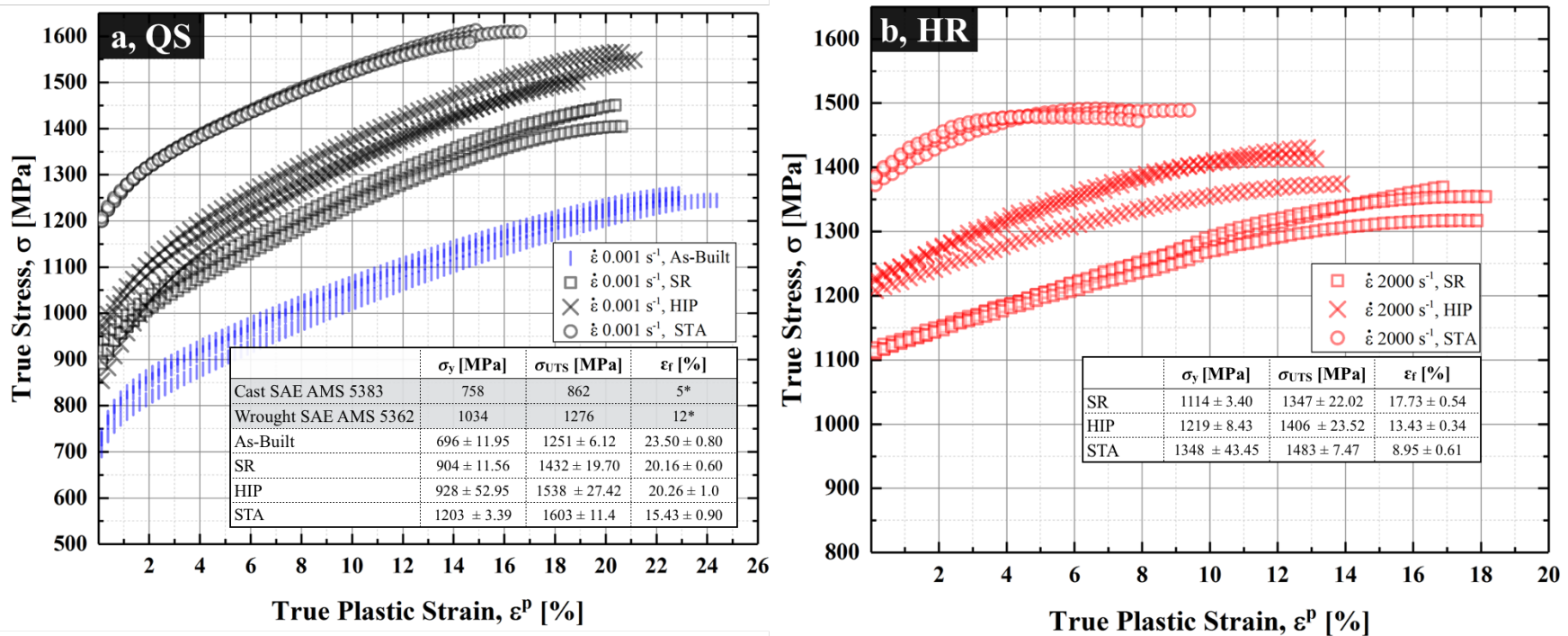


Figure 3-2 True stress - true strain relations for quasi-static ($\dot{\epsilon} = 0.001 \text{ s}^{-1}$) and high rate ($\dot{\epsilon} = 2000 \text{ s}^{-1}$) tensile results for SLM IN718 specimens in as-built, SR, HIP and STA conditions. Cast and wrought IN718 values per SAE AMS specifications [33], [34]. As-built, quasi-static results, not published in the open-scientific literature, were provided by NASA MSFC; specimen geometry in accordance with ASTM E8 standard [36], i.e., standard-sized specimens were used. Broadly stated, yield (σ_y) and ultimate tensile (UTS) strengths increase with each sequential post-processing step while a decrease on elongation to failure (ϵ_f) was observed. *Total strain (elastic + plastic).

Table 3-2 Summary of AM PBF and DED Laser-Melted IN718 QS tensile properties for different orientations and post-processing conditions. Adapted from [38].

Powder Bed Fusion (PBF) Laser-Melted IN718						
Machine Type	Condition	Specimen Orientation	σ_y , [MPa]	UTS, [MPa]	ϵ_p , [%]	Ref.
EOS M 290	As-Built		696 ± 11.9	1251 ± 6.1	23.5 ± 0.8	
	SR	XY	904 ± 11.9	1432 ± 19.7	20.1 ± 0.6	This Investigation
	HIP		928 ± 52.9	1538 ± 27.4	20.3 ± 1	
	STA		1203 ± 3.4	1603 ± 11.1	15.4 ± 0.9	
SLM	As-Built	XY	816 ± 24	1085 ± 11	19.1 ± 0.7	
		Z	737 ± 4	1010 ± 10	20.6 ± 2.1	[6]
	HT	XY	1227 ± 1	1447 ± 10	10.1 ± 0.6	
		Z	1136 ± 16	1357 ± 5	13.6 ± 0.2	
EOS M280	HT	Z	1034	1309	27	[7]
		XY	1068	1344	27	
Direct Energy Deposited (DED) Laser-Melted IN718						
SMD	As-Built	XY	473 ± 6	828 ± 8	28 ± 2	[39]
DLD	As-Built	Z	650	1000	-	
	HT		1257	1436	-	[40]
Laser	As-Built	Not Specified	590	845	11	
	HT		1133	1240	9	[41]
EBF3	As-Built	XY	580	910	22	[42]
EBF3	As-Built	XY	655	978	-	
		YX	699	936	-	[43]
		XY	986	1114	-	
		YX	998	1162	-	
DLD	HT	Not Specified	1097	1321	9.8	[44]
DLD	HT	Not Specified	1034	1276	12	[45]
Laser Wire	HT	Not Specified	1079	1314	20.4	[46]

HT: Heat treated.

Build orientation on tensile specimens are documented using XYZ designation in accordance to ASTM standard [47]. In this terminology Z designates the build direction.

OM and SEM examined the fracture surfaces of the tested specimens. The corresponding tension-overload fracture morphologies are presented in Figure 3-3. Fracture topography exhibits a fine dimpled surface, and indicates a transgranular ductile failure mode. It is also noted that unlike in a previous study [48], no fracture mode dependence on thermal post-process was observed.

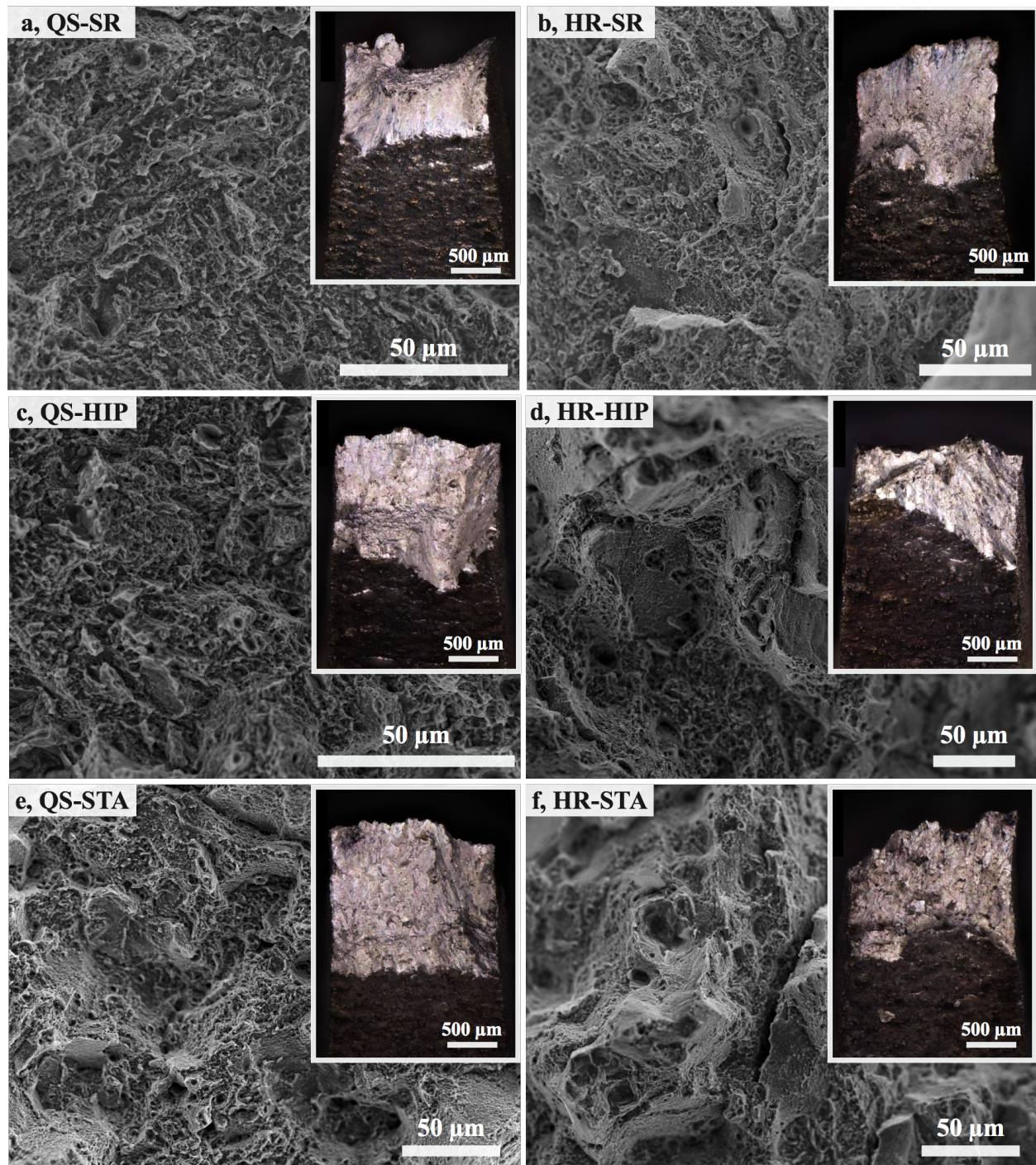


Figure 3-3 OM and SEM micrographs illustrates the tensile fracture surfaces of post-processed SLM IN718 specimens tested under different deformation rates (0.001 s^{-1} and 2000 s^{-1}). Irrespective of the post-processing condition (SR, HIP, STA) test coupons exhibit a ductile fracture.

3.4 Concluding Remarks

To summarize, the influence of a sequential, standard, thermal post-processes on the morphology and tensile performance of a SLM IN718 was studied. Microstructural investigations revealed a transformation from the as-built columnar, melt pool morphology to an isotropic, dendrite-free, architectural arrangement after a series of thermal post-processes (SR, HIP and STA). Correspondingly, mechanical characterization, performed at different deformation rates, shown that yield (σ_y) and ultimate tensile strengths (UTS) increase with each sequential post-processing step while the elongation to failure (ϵ_f) values decrease. The improvement in strength is attributed to precipitation of the γ' and γ'' strengthening phases [28], [31], [37]. Furthermore, as theorized by Zhang and coworkers [28], the decreased ductility can be due to two main reasons: on one hand, the precipitates of γ' and γ'' strengthening phases lead to a precipitation hardening of the matrix and then cause a drop in the elongation to failure (ϵ_f) whereas, on the other hand, amounts of acicular δ precipitates dramatically attribute to the decrease of ductility. Quasi-static and high rate tensile experiments examined strain rate dependence on flow stresses. As normally expected from a polycrystalline metallic material system, strength increase at the expense of elongation to failure with increasing deformation rates. Finally, irrespective of thermal post-processing and deformation rate, the tensile coupons exhibited a ductile fracture mode.

References

- [1] X. Wang, X. Gong, and K. Chou, “Review on powder-bed laser additive manufacturing of Inconel 718 parts,” *Proc. Inst. Mech. Eng. Part B J. Eng. Manuf.*, vol. 231, no. 11, pp. 1890–1903, 2017.
- [2] X. Wang and K. Chou, “Effects of thermal cycles on the microstructural evolution of Inconel 718 during selective laser melting process,” *Addit. Manuf.*, vol. 18, pp. 1–14, 2017.
- [3] A. Thomas, M. El-Wahabi, J. M. Cabrera, and J. M. Prado, “High temperature deformation of Inconel 718,” *J. Mater. Process. Technol.*, vol. 177, no. 1–3, pp. 469–472, 2006.
- [4] E. Akca and A. Gürsel, “A Review on Superalloys and IN718 Nickel-Based INCONEL Superalloy,” *Period. Eng. Nat. Sci.*, vol. 3, no. 1, 2015.
- [5] SAE AMS F Corrosion Heat Resistant Alloys Committee, “AMS5664E: Nickel Alloy, Corrosion and Heat Resistant, Bars, forgings, and Rings, 52.5Ni - 19Cr - 3.0Mo - 5.1Cb - 0.90Ti - 0.50Al - 18Fe, Consumable Electrode or Vacuum Induction Melted, 1950 °F (1066 °C) Solution Heat Treated, Precipitation Hardenable.” SAE International, p. 9, 2006.
- [6] J. Strößner, M. Terock, and U. Glatzel, “Mechanical and Microstructural Investigation of Nickel-Based Superalloy IN718 Manufactured by Selective Laser Melting (SLM),” *Adv. Eng. Mater.*, vol. 17, no. 8, pp. 1099–1105, 2015.
- [7] O. Scott-Emuakpor, J. Schwartz, T. George, C. Holycross, C. Cross, and J. Slater, “Bending fatigue life characterisation of direct metal laser sintering nickel alloy 718,” *Fatigue Fract. Eng. Mater. Struct.*, vol. 38, no. 9, pp. 1105–1117, Sep. 2015.
- [8] W. J. Sames, F. A. List, S. Pannala, R. R. Dehoff, and S. S. Babu, “The metallurgy and processing science of metal additive manufacturing,” *Int. Mater. Rev.*, vol. 6608, no. March, 2016.
- [9] L. M. Sochalski-Kolbusz *et al.*, “Comparison of Residual Stresses in Inconel 718 Simple Parts Made by Electron Beam Melting and Direct Laser Metal Sintering,” *Metall. Mater. Trans. A*, vol. 46A, no. March, pp. 1419–1432, 2015.
- [10] L. E. Murr *et al.*, “Metal Fabrication by Additive Manufacturing Using Laser and Electron Beam Melting Technologies,” *J. Mater. Sci. Technol.*, vol. 28, no. 1, pp. 1–14, 2012.
- [11] Z. Wang, K. Guan, M. Gao, X. Li, X. Chen, and X. Zeng, “The microstructure and mechanical properties of deposited-IN718 by selective laser melting,” *J. Alloys Compd.*, vol. 513, pp. 518–523, 2012.

- [12] I. Gibson, D. Rosen, and B. Stucker, *Additive Manufacturing Technologies*. 2015.
- [13] W. R. Whittington *et al.*, “Capturing the effect of temperature, strain rate, and stress state on the plasticity and fracture of rolled homogeneous armor (RHA) steel,” *Mater. Sci. Eng. A*, vol. 594, pp. 82–88, Jan. 2014.
- [14] P. G. Allison, H. Grewal, Y. Hammi, H. R. Brown, W. R. Whittington, and M. F. Horstemeyer, “Plasticity and Fracture Modeling/Experimental Study of a Porous Metal Under Various Strain Rates, Temperatures, and Stress States,” *J. Eng. Mater. Technol.*, vol. 135, no. 4, p. 41008, Sep. 2013.
- [15] P. G. Allison, M. F. Horstemeyer, Y. Hammi, H. R. Brown, M. T. Tucker, and Y.-K. Hwang, “Microstructure–property relations of a steel powder metal under varying temperatures, strain rates, and stress states,” *Mater. Sci. Eng. A*, vol. 529, pp. 335–344, Nov. 2011.
- [16] O. G. Rivera *et al.*, “Microstructures and mechanical behavior of Inconel 625 fabricated by solid-state additive manufacturing,” *Mater. Sci. Eng. A*, vol. 694, no. March, pp. 1–9, 2017.
- [17] O. G. Rivera *et al.*, “Influence of Texture and Grain Refinement on the Mechanical Behavior of AA2219 Depositions Fabricated by Solid State Additive Manufacturing,” *Mater. Des.*
- [18] C. Weinong and S. BO, *Split Hopkinson (Kolsky) Bar*, vol. 1. 2013.
- [19] D. K. Francis, W. R. Whittington, W. B. Lawrimore, P. G. Allison, S. A. Turnage, and J. J. Bhattacharyya, “Split Hopkinson Pressure Bar Graphical Analysis Tool,” *Exp. Mech.*, vol. 57, no. 1, pp. 179–183, 2017.
- [20] “NASA MSFC-SPEC-3717: Specification for Control and Qualification of Laser Powder Bed Fusion Metallurgical Processes,” Huntsville, 2017.
- [21] ASTM-International, “Standard specification for additive manufacturing nickel alloy (UNS N07718) with powder bed fusion, F3055-14,” West Conshohocken, PA, 2014.
- [22] L. N. Carter, M. M. Attallah, and R. C. Reed, “Laser Powder Bed Fabrication of Nickel-Base Superalloys: Influence of Parameters; Characterisation, Quantification and Mitigation of Cracking,” in *Superalloys 2012: 12th International Symposium on Superalloys*, 2012, pp. 577–586.
- [23] W. Dhifeng, L. Shuai, W. Qungsong, C. Yan, Z. Sheng, and S. Yusheng, “Effect of molten pool boundaries on the mechanical properties of selective laser melting parts,” *J. Mater. Process. Tech.*, vol. 214, no. 11, pp. 2660–2667, 2015.
- [24] I. Yadroitsev and I. Smurov, “Surface Morphology in Selective Laser Melting of Metal Powders,” *Phys. Procedia*, vol. 12, pp. 264–270, 2011.

- [25] Q. Shi, D. Gu, M. Xia, S. Cao, and T. Rong, “Effects of laser processing parameters on thermal behavior and melting / solidification mechanism during selective laser melting of TiC / Inconel 718 composites,” *Opt. Laser Technol.*, vol. 84, pp. 9–22, 2016.
- [26] B. Zhang and C. Coddet, “Selective Laser Melting of Iron Powder: Observation of Melting Mechanism and Densification Behavior Via Point-Track-Surface-Part Research,” *J. Manuf. Sci. Eng.*, vol. 138, no. May, pp. 1–9, 2016.
- [27] F. Liu, X. Lin, G. Yang, M. Song, J. Chen, and W. Huang, “Microstructure and residual stress of laser rapid formed Inconel 718 nickel-base superalloy,” *Opt. Laser Technol.*, vol. 43, no. 1, pp. 208–213, 2011.
- [28] D. Zhang, W. Niu, X. Cao, and Z. Liu, “Effect of standard heat treatment on the microstructure and mechanical properties of selective laser melting manufactured Inconel 718 superalloy,” *Mater. Sci. Eng. A*, vol. 644, pp. 32–40, 2015.
- [29] K. N. Amato *et al.*, “Microstructures and mechanical behavior of Inconel 718 fabricated by selective laser melting,” *Acta Mater.*, vol. 60, no. 5, pp. 2229–2239, 2012.
- [30] A. Mostafe, I. Picazo Rubio, V. Brailovski, M. Jahazi, and M. Medraj, “Structure, Texture and Phases in 3D Printed IN718 Alloy Subjected to Homogenization and HIP Treatments,” *Metals (Basel)*, pp. 1–23, 2017.
- [31] L. I. U. Fencheng, L. I. N. Xin, Y. Gaolin, S. Menghua, C. Jing, and H. Weidong, “Recrystallization and its influence on microstructures and mechanical properties of laser solid formed nickel base superalloy Inconel 718,” *Rare Met.*, vol. 30, pp. 433–438, 2011.
- [32] E. Chlebus, K. Gruber, B. Ku??nicka, J. Kurzac, and T. Kurzynowski, “Effect of heat treatment on the microstructure and mechanical properties of Inconel 718 processed by selective laser melting,” *Mater. Sci. Eng. A*, vol. 639, pp. 647–655, 2015.
- [33] SAE AMS, “AMS 5383.” SAE International, 2012.
- [34] SAE AMS, “AMS 5362.” SAE International, 2009.
- [35] J. Cheng, S. Y. Zhang, L. Xue, O. H. Yang, X. Lin, and W. D. Hunag, “Mechanical properties of Ti-6Al-4V alloy by laser rapid forming,” *Rare Met.*, vol. 36, no. 475, 2007.
- [36] A. International, “Standard Test Methods for Tension Testing of Metallic Materials,” 2010.
- [37] H. Qi, M. Azer, and A. Ritter, “Studies of Standard Heat Treatment Effects on Microstructure and Mechanical Properties of Laser Net Shape Manufactured INCONEL 718,” *Metall. Mater. Trans. A*, vol. 40, no. 10, pp. 2410–2422, Oct. 2009.
- [38] J. J. Lewandowski and M. Seifi, *Metal additive manufacturing: a review of mechanical properties*, vol. 46. 2016, pp. 151–186.

- [39] B. Baufeld, "Mechanical Properties of INCONEL 718 Parts Manufactured by Shaped Metal Deposition (SMD)," *J. Mater. Eng. Perform.*, vol. 21, no. 7, pp. 1416–1421, Jul. 2012.
- [40] P. L. Blackwell, "The mechanical and microstructural characteristics of laser-deposited IN718," *J. Mater. Process. Technol.*, vol. 170, no. 1–2, pp. 240–246, Dec. 2005.
- [41] X. Zhao, J. Chen, X. Lin, and W. Huang, "Study on microstructure and mechanical properties of laser rapid forming Inconel 718," Apr. 2008.
- [42] R. K. Bird and J. Hibberd, "Tensile Properties and Microstructure of Inconel 718 Fabricated with Electron Beam Freeform Fabrication," 2009.
- [43] W. A. Tayon, R. N. Shenoy, M. R. Redding, R. Keith Bird, and R. A. Hafley, "Correlation Between Microstructure and Mechanical Properties in an Inconel 718 Deposit Produced via Electron Beam Freeform Fabrication," *J. Manuf. Sci. Eng.*, vol. 136, no. 6, p. 61005, Oct. 2014.
- [44] Y.-N. Zhang, X. Cao, P. Wanjara, and M. Medraj, "Tensile properties of laser additive manufactured Inconel 718 using filler wire," *J. Mater. Res.*, vol. 29, no. 17, pp. 2006–2020, 2014.
- [45] H. Qi, M. Azer, and A. Ritter, "Studies of standard heat treatment effects on microstructure and mechanical properties of laser net shape manufactured INCONEL 718," *Metall. Mater. Trans. A Phys. Metall. Mater. Sci.*, vol. 40, no. 10, pp. 2410–2422, 2009.
- [46] X. Cao, B. Rivaux, M. Jahazi, J. Cuddy, and A. Birur, "Effect of pre- and post-weld heat treatment on metallurgical and tensile properties of Inconel 718 alloy butt joints welded using 4 kW Nd:YAG laser," *J. Mater. Sci.*, vol. 44, no. 17, pp. 4557–4571, Sep. 2009.
- [47] ASTM, "ASTM/ISO 52921: Standard terminology for additive manufacturing coordinate systems and test methodologies." 2013.
- [48] G. A. Rao, M. Kumar, and D. S. Sarma, "Effect of standard heat treatment on the microstructure and mechanical properties of hot isostatically pressed superalloy inconel," *Mater. Sci. Eng. A*, vol. 355, pp. 114–125, 2003.

CHAPTER 4 PROCESSING, MICROSTRUCTURE AND MECHANICAL PERFORMANCE OF THE $\text{Al}_x\text{CoCrFeNi}$ HIGH-ENTROPY ALLOY SYSTEM WITH MULTIPRINCIPAL ELEMENTS

Omar L. Rodriguez¹, Paul G. Allison^{1*}, Lin Li², Haoyan Diao³ and Peter K. Liaw³

¹ The University of Alabama, Department of Mechanical Engineering, Tuscaloosa, AL, 35487

² The University of Alabama, Department of Metallurgical and Materials Engineering, Tuscaloosa, AL, 35487

³ The University of Tennessee, Department of Material Science and Engineering, Knoxville, TN, 37996

* Corresponding Author: pallison@eng.ua.edu

Keywords: High Entropy Alloys, High Strain Rate

Abstract

High Entropy Alloys (HEAs) are equiatomic, multicomponent metallic systems, that presents exceptional microstructural stability. This work focuses on understanding the strain rate, stress state and temperature influence on plastic flow of $\text{Al}_x\text{CoCrFeNi}$ ($x = 0.3$ and 0.7 in molar ratio) HEAs. The $\text{Al}_{0.3}$ HEA exhibited a FCC microstructure according to neutron diffraction analysis with sigmoidal plastic behavior suggesting multiple deformation mechanisms occurring in the material. As expected, higher values of flow stresses were recorded as the strain rate increase. Additionally, compressive flow data at elevated temperatures exhibited sustained high flow stresses and extended ductility. On the contrary, neutron diffraction analysis identified that the $\text{Al}_{0.7}$ HEA consisted of a multi-phase FCC and BCC type microstructure that exhibited a linear hardening behavior. As shown by the mechanical data across strain rate scales, the precipitation of a second phase, BCC type, influence positively the alloy strength. Although,

while benefitting from the multiplicity of strengthening mechanisms considerable softening was observed on the compressive flow curves at elevated temperatures. Overall, the combination of high elevated-temperature strength, excellent thermal stability, and enhanced ductility makes HEAs a potential candidate material system for high-temperature applications, however, stringent controls over the manufacturing processes are required to ensure their success.

4.1 Introduction

Multicomponent HEAs are a relative new concept in alloy design in which a system is defined to have five or more principal elements with the concentration of each principal constituent varying between 5 and 35 at.%. HEAs could also contain minor elements to modify the properties of the base material system. Consequently, the atomic percentage of each minor element is hence less than 5 at%. In spite of the presence of a large number of components, HEAs may show simple phases such as FCC, BCC and FCC+BCC [1]. AlCoCrFeNi [2]–[13] and the Cu version (AlCoCrCuFeNi) [14]–[19], are the most comprehensively studied HEA systems, which depict one of the aforementioned crystallographic arrangements [2]–[13].

In the context of a $\text{Al}_x\text{CoCrFeNi}$, the variation of the Al ratio leads to a variation in the crystal structures [6], [20]. Increasing the Al content induces larger lattice strain and the ensuing distortion leads to relaxation via phase transformation in the crystal structure [21]. Wang and coworkers [20] studied the effect of Al content on the crystal structure, morphology and mechanical properties of an $\text{Al}_x\text{CoCrFeNi}$ ($x = 0 – 2.0$ in molar ratio) HEA. Guided by X-Ray Diffraction (XRD) results, the researchers concluded that low Al content ($\text{Al}_0\text{-}\text{Al}_{0.4}$) forms a single FCC crystal structure. Correspondingly, reflections of the BCC phase appear in specimens

with Al concentration larger than 0.5 molar ratio. Additionally, Wang and collaborators [20] noted that for single FCC structured alloys ($\text{Al}_0\text{-Al}_{0.4}$) a low hardness of about 120 HV was obtained, however, by adding Al atoms the hardness increased up to a maximum value of 527 HV for the $\text{Al}_{2.0}$ alloy. These results suggested that the formation of BCC structures is the main hardening factor, i.e. precipitation strengthening. Compared with the BCC crystal structure, FCC alloys usually have higher ductility but lower strength since BCC structures have stronger directional bonding and lack of a truly close-packed slip plane [22]. Furthermore, the increase in interphase area between FCC and BCC phases could be a contributing factor to the material strength since the mean free path of dislocations is reduced in a mixed structure.

HEAs have four core effects that set them apart from the conventional alloys, which usually have one or two principal components [21]. These core effects are high-entropy effect, sluggish diffusion effect, severe lattice distortion effect and cocktail effect. Given their influences on thermodynamics and kinetics relations, the properties of HEAs are not as simple as those predicted from the rule of mixture, i.e. physical metallurgy principles of HEAs deviate from those of conventional alloys thus requiring significant research efforts. As such, the investigation presented here studies the interplays between composition, processing, microstructure and mechanical behavior. By assessing the influence of strain rate and temperature on the flow stress, and their influence on substructural evolution for $\text{Al}_x\text{CoCrFeNi}$ ($x = 0.3$ and 0.7 in molar ratio) HEAs, therefore, this study set the foundation for their insertion into relevant structural applications at various strain rates and temperatures.

4.2 Experimental Methods

Bulk HEA buttons and/or ingots with an $\text{Al}_x\text{CoCrFeNi}$ ($x = 0.3$ and 0.7 in molar ratio) elemental composition were synthesized at the University of Tennessee – Knoxville following a liquid-state arc-melting route (Large Bell Jar model ABJ-900 - Materials Research Furnaces, Inc.). The melting of the constituent elements, 99% purity level, was done under a Ti-gettered argon atmosphere. Multiple repetitive melting and solidification processes were performed to ensure the chemical homogeneity of the alloys. The H-shaped, sub-standard sized tensile coupons previously used for both QS and HR tensile experiments on cast, wrought, and AM alloys [23]–[25] (gage length, $gl = 4.50$ mm, width, $w = 2.30$ mm thickness, $t = 1.50$ mm) and cylindrical compression specimens (diameter, φ and length, $l = 4.5$ mm) were machined from cast-ingots.

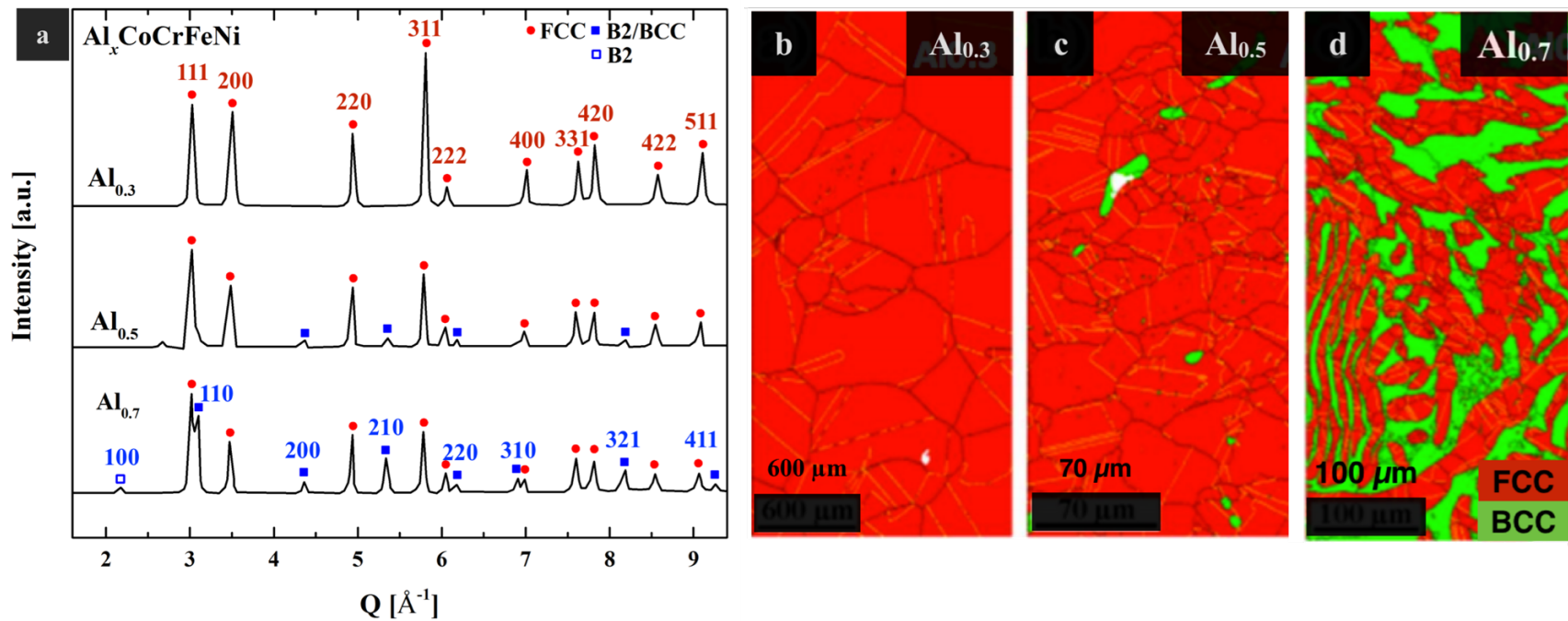
To quantify the deformation rate and stress state influence on flow stress, a series of uniaxial experiments were performed on specimens. An MTS thermo-mechanical load frame equipped with an induction coil programmable heating system performed the quasi-static tension and compression experiments on sub-standard sized specimens. An optical extensometer technique was employed to capture axial displacement. Dynamic tension and compression experiments were performed with an Inconel 718 tension-compression Kolsky bar recovery apparatus ($\varphi = 13.0$ mm) equipped with an induction coil programmable heating system. Copper pulse shapers ($t = 1.5$ mm) were used to eliminate the Pochhammer-Chree oscillations in the incident pulse as suggested by previous researchers [26]. Strain metrology data, obtained using semiconductor strain gages cemented on the bars, was processed by the Split Hopkinson Pressure Bar Graphical Analysis Tool open-source MATLAB[®] code [27].

Specimens were prepared for microstructural observations with standard metallographic procedures including sectioning, mounting, grinding. Optical (OM) and Scanning Electron Microscope (SEM) samples were etched in Aqua Regia (3:1 hydrochloric acid and nitric acid). Both, KEYENCE VHX-1000 series digital microscope and a TESCAN LYRA SEM were used for microstructural and fractography analyses. Energy-dispersive X-ray Diffraction Spectroscopy (EDS) characterization was carried out on a TESCAN LYRA SEM.

4.3 Results and Discussions

The tendency of HEAs to form simple solid-solution microstructures was established from early efforts by Yeah et al. [28] and Tong and coworkers [14] on $\text{Al}_x\text{CoCrFeNi}$ with varying Al concentrations. In the current work, neutron-diffraction experiments at room temperature (Figure 4-1) were used to identify the crystals structures in the $\text{Al}_x\text{CoCrFeNi}$ HEAs and the composition where the transition from a single-phase to a duplex system occurs. Two cubic crystal structures, FCC and BCC were identified on the as-cast $\text{Al}_{0.3,0.5,0.7}$ ingots. Low Al concentration ($\text{Al}_{0.3}$) alloy nucleates a single FCC crystalline phase. Minor reflections of BCC structures, illustrated as blue squares, appear on the $\text{Al}_{0.5}$ alloy while their intensity increases in the $\text{Al}_{0.7}$ diffraction pattern. Also notice, for the $\text{Al}_{0.7}$ alloy system, the presence of the B2 superstructure, thus indicating disordered BCC plus B2 phase. These diffraction observations are consistent with published scientific data [20]. Once the phases were identified, EBSD microstructural characterization established the phase fractions and average grain size. As expected, the $\text{Al}_{0.3}$ alloy contained single phase FCC coarse equiaxed grains with representative sizes averaging $600 \mu\text{m}$. As for the $\text{Al}_{0.7}$ alloys, EBSD analysis revealed a Widmanst  ten morphology in equiaxed grains similar to Ti alloys microstructures [29]. Widmanst  ten FCC sideplates, averaging $26 \mu\text{m}$ in width,

accounts for roughly 70% percent of the total volume fraction. The remaining regions, BCC intersideplates (avg. $19 \mu\text{m}$ in width), spinodally decompose into a NiAl-type ordered BCC B2 structure. Hereinafter only $\text{Al}_{0.3}$ and $\text{Al}_{0.7}$ alloys combinations will be discussed.



Quasi-static (QS) and high rate (HR) compression true stress-true plastic strain relations for the single-phase FCC Al_{0.3} and duplex FCC+BCC type Al_{0.7} specimens are plotted in Figure 4-2. An interrupted testing methodology was adopted for the QS strained specimens to investigate the evolution of the deformed microstructures at varying strain levels. Specifically, Al_{0.3} and Al_{0.7} specimens were compressed to specified strain levels without achieving fracture. Incidentally, HR specimens compressed by a single loading pulse did not experience fracture. Irrespectively of strain rate, Al_{0.3} specimens present a sigmoidal flow stress curve typical of FCC-structured polycrystalline materials. Furthermore, higher average yield stress (σ_y) values were calculated for dynamic HR (avg. $\dot{\varepsilon} 1500 \text{ s}^{-1}$) specimens ($\sigma_y = 342 \pm 33 \text{ MPa}$) when compared to those obtained at QS rates ($\dot{\varepsilon} 0.001 \text{ s}^{-1}$) for the tested samples ($\sigma_y = 157 \pm 24 \text{ MPa}$). Meanwhile the compressive behavior of duplex FCC+BCC type Al_{0.7} appears to be dominated by the increase in Al concentration thus inciting a collaboration between strain, solution and precipitation strengthening mechanisms. An increase in Al concentration cause an intensification of the lattice distortion in consideration of the non-symmetrical neighboring atoms. For instance, hardness and strength effectively increase because of large solution hardening in a heavily distorted lattice [5], [22], [31], [32]. Furthermore, apart from the fact that the BCC phase is stronger than the FCC phase [21], the interphase area between phases is a contributing factor on the hardening of duplex Al_{0.7} since the mean free path of dislocations is reduced [22]. Not surprisingly, the interaction between the multiplicities of hardening mechanisms is reflected on the Al_{0.7} stress-strain relations as higher flow stresses than those presented by the Al_{0.3} specimens. Lastly, the influence of the strain rate effect on Al_{0.7} yield behavior was similar to the one shown by Al_{0.3}. For HR (avg. $\dot{\varepsilon} 1500 \text{ s}^{-1}$) specimens, a $\sigma_y = 750 \pm 50 \text{ MPa}$ was computed; higher when compared to those obtained at QS ($\dot{\varepsilon} 0.001 \text{ s}^{-1}$) conditions ($\sigma_y = 480 \pm 13 \text{ MPa}$). This type of σ_y

dependence on strain-rate is typical of low SFE materials [2] Regarding their hardening behavior, signs of recovery after an initial hardening region are shown by the QS specimens. On the contrary, HR specimens exhibited no recovery. Hardening behaviors are explained in greater details in a following section.

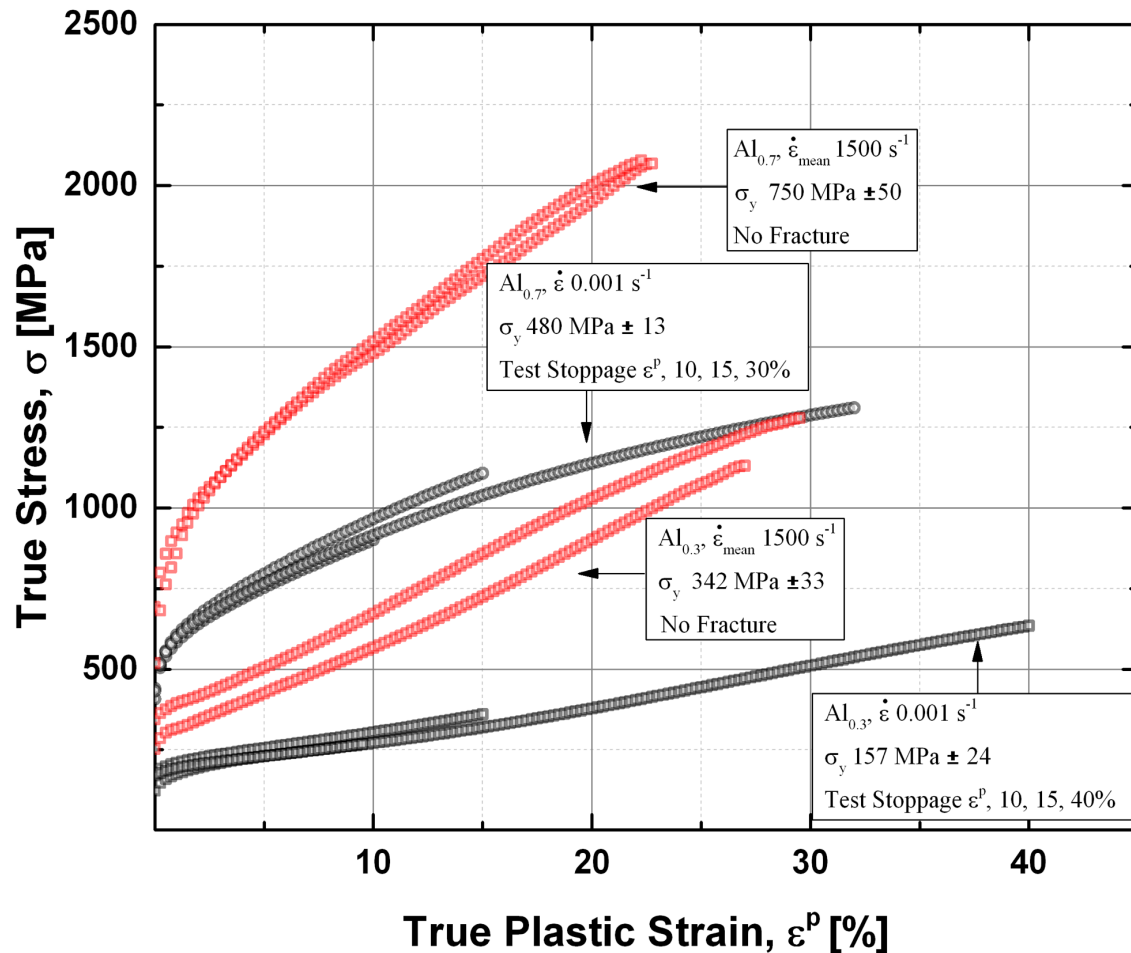


Figure 4-2 Room temperature (23 °C) macroscopic behavior of Al_{0.3} and Al_{0.7} obtained by compression testing at different deformation rates (0.001, 1500 s⁻¹). Interrupted compression testing was performed on the quasi-static specimens to study the substructural evolution. As observed, Al concentration and microstructural phases influence the flow stress levels (solution and precipitation hardening). Strength values calculated for Al_{0.3} specimens (FCC lattice) are significantly lower than those obtained from the Al_{0.7} specimens (FCC + BCC type lattice).

Figure 4-3 presents the compressive behavior under different testing temperatures (23, 250 and 500 °C) at various strain rates (0.001, 1500 s⁻¹) of lower (Al_{0.3}) and higher (Al_{0.7}) Al

content HEAs. As depicted, the flow stresses curves of $\text{Al}_{0.3}$, with an FCC structure, have the benefit of sustained high flow stresses and extended ductility at elevated temperatures. Although compressive σ_y values experienced the expected negative correlation with temperature (σ_y 23 °C = 157 ± 24 MPa, σ_y 250 °C = 135 ± 1.46 MPa and σ_y 500 °C = 91 ± 7.23 MPa), the alloy retained its work hardening capability, i.e., no thermal softening was detected. Moreover, the sigmoidal strain hardening behavior displayed by the specimens tested at room temperature is not obviously exhibited by the elevated temperature strained test articles. Similar to QS tested specimens, the HR results (Figure 4-3b) depicts sustained work hardening capacity as temperature increases. Regarding σ_y values, the anomalies on the results (σ_y 500 °C > σ_y 250 °C and σ_y 250 °C ≈ σ_y 23 °C) could be associated to data scatter product of the Kolsky bar experimental method and/or data reduction procedure [33].

As demonstrated in Figure 4-3 c and d, dual phase FCC + BCC type $\text{Al}_{0.7}$ alloy exhibits higher strength values than lower Al content specimens. Compressive σ_y values are substantially higher than those exhibited by $\text{Al}_{0.3}$ at any testing condition (temperature and/or strain rate). As mentioned earlier, the presence of a second phase incites the collaboration between strain, solution and precipitation strengthening mechanisms. On the contrary, the lower thermal resistance of $\text{Al}_{0.7}$ alloy indicated that the BCC phase lacked the positive temperature effect of strength thus causing a considerable softening of the alloy at elevated temperatures. With respect to the compression samples, both the $\text{Al}_{0.3}$ and $\text{Al}_{0.7}$ were not tested to fracture, but only have data reported until the testing was stopped due to user-defined load frame operational parameters. Hence, to conclude, in agreement with a published article by Tong and coworkers [14], the combination of high elevated-temperature strength, excellent thermal stability, and enhanced ductility makes these alloys good candidates for high-temperature applications.

Generally, due to the large number of equivalent slip systems, plastically deformed FCC crystals slip on more than one octahedral plane [34]. In early plastic stages, FCC crystals deform by slip on a single plane. As deformation progresses, in a high SFE material, several intersecting planes are activated at the same time inducing an increase in the stress required to produce additional deformation (strain hardening). Dislocations, in high SFE materials, tends to rearrange themselves into cell-like structures with the majority of the dislocations residing on the cell walls [35]. On the other hand, cross-slip is inhibited in low SFE materials causing dislocations to arrange themselves into planar arrays. In addition to controlling the dislocation substructure, SFE also affects the propensity of a material to nucleate mechanical twins, with low SFE materials favoring twinning. As stated in published literature, twinning and slip are competitive deformation processes with slip generally dominating [36]. However, at high strain rates and/or at low temperatures, twinning can contribute to the plastic deformation in addition to the slip mechanism. Systematic studies of the Θ behavior and substructure evolution of low SFE FCC alloys has been carried out by Rohatgi et. al [36], Guitierrez-Urrita and Raabe [37], El-Danaf et. al. [38] and Caballero and Varma [39] clearly stating the SFE transition value from dislocation to planar cell arrangements and from slip-dominated plasticity to twin-induced deformation. Lastly, as reported in several investigations on low SFE FCC metals, plasticity stacking faults assist on the progression of plastic deformation although their presence on HEAs has not been detected [40]–[43].

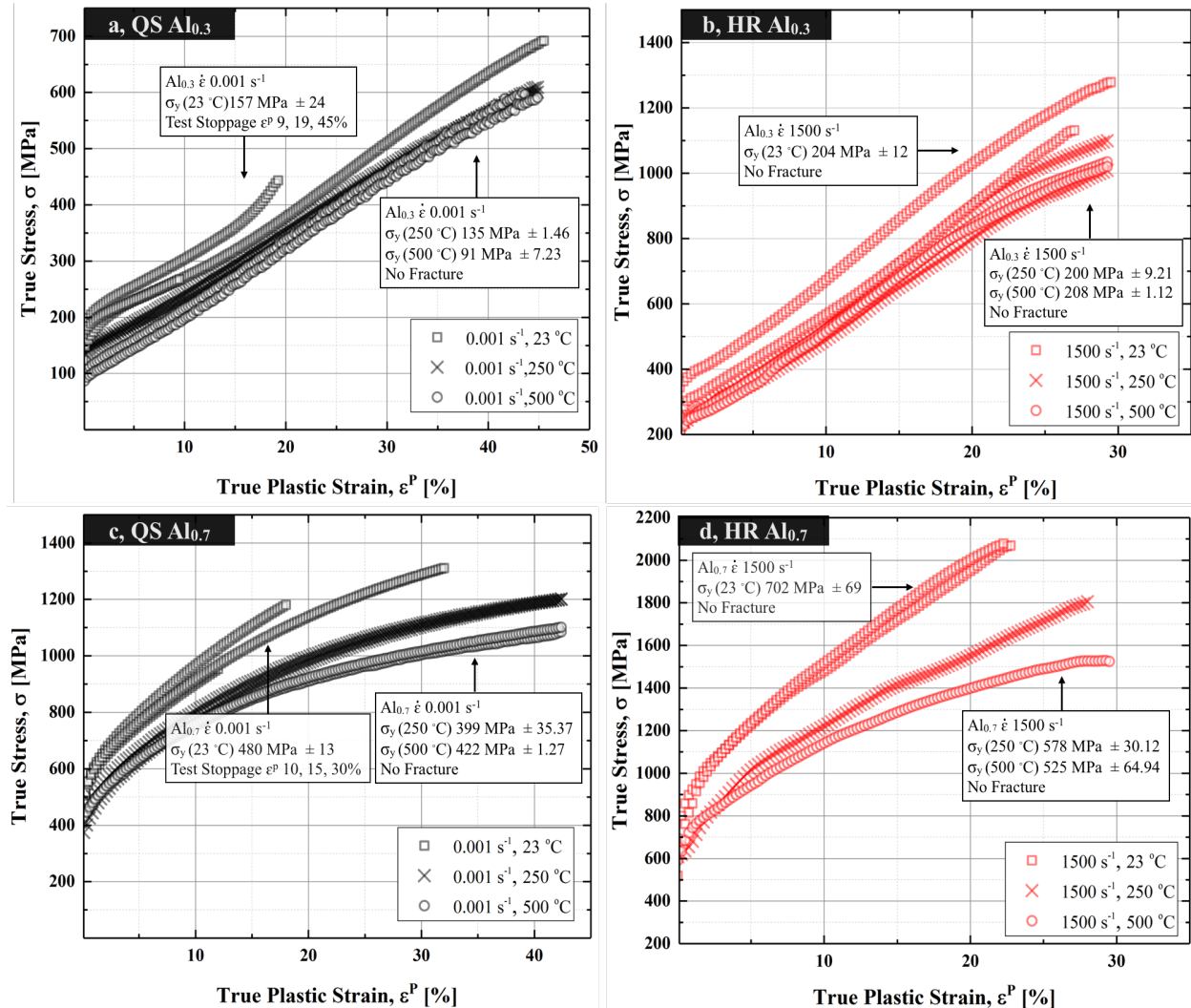


Figure 4-3 Room (23 °C) and elevated (250, 500 °C) temperature macroscopic behavior of Al_{0.3} and Al_{0.7} obtained by compression testing at different deformation rates. Interrupted compression testing was performed on the room temperature quasi-statically deformed specimens to study the substructural evolution. Irrespectively of strain rate, Al_{0.3} alloy exhibited minimum thermal effect on work hardening capacity. Regarding the anomalies of the σ_y results ($\sigma_y 500^\circ\text{C} > \sigma_y 250^\circ\text{C}$ and $\sigma_y 250^\circ\text{C} \approx \sigma_y 23^\circ\text{C}$), those could be associated to data scatter product of the Kolsky bar experimental method [33]. Unlike the lower Al content alloy (Al_{0.3}) considerable thermal softening was observed at elevated temperatures on Al_{0.7} test articles.

Figure 4-4 conveys the strain hardening rate dependence on true plastic strain ($\Theta(\varepsilon^p)$) for

QS and HR Al_{0.3} and Al_{0.7} compression specimens. As a solely FCC structure, its Θ behavior

could be conceptualized into three distinct stages. Region I, dominated by dislocation glide

plasticity, is presented as a stage where the Θ decrease sharply. Region II, characterized by an

enhancement in Θ , signals the presence of additional strengthening mechanisms i.e. mechanical twins providing barriers to dislocation motion thus inducing an increase in strength and strain hardening. Finally, Region III exhibits a decreasing slope similar to Region I: dislocation-slip-dominated plastic deformation.

The influence of the imposed strain rate on Θ for the $\text{Al}_{0.3}$ alloys is evident. While the magnitude of Θ increase with increasing strain, suggesting higher dislocation and twin densities, the onset of Region II (where twinning becomes a dominant deformation mechanism) decreases at a higher strain rate (from 3 to 1.5 % ε^p). Meanwhile, the $\text{Al}_{0.7}$ compression specimens illustrate an interesting Θ dependence on strain rate. QS macroscopic Θ behavior of FCC+BCC $\text{Al}_{0.7}$ is characterized by a two-stage hardening region which resembles the hardening response of FCC copper [44]. While the initial stage, exhibiting a low hardening rate, is associated with single slip plasticity, Region II displays a steadily decreasing Θ , which is related to a dynamic recovery process. In agreement with the computed QS Θ curves, the corresponding OM photomicrographs (Figure 4-5) shows no indications of mechanical twins or deformation marks. On the contrary, HR Θ response signaled the introduction of mechanical twins to the microstructure with a transition from Region I to Region II occurring at 10% ε^p .

The evolution of the QS $\text{Al}_{0.3}$ deformed microstructure, and their relation to Θ , is presented by OM micrographs in Figure 4-6. All OM micrographs presented on Figure 4-6 are from the longitudinal sections of the specimens with the loading axis parallel to the vertical direction of the micrographs. Figure 4-6a shows the Θ behavior and microstructure of an $\text{Al}_{0.3}$ compression specimen strained to approximately 10% ε^p . The total strain imposed on the specimen placed itself at the onset of Region II. With respect to the corresponding deformed

microstructure, notice the presence of annealing twins and the apparent absence of their mechanical counterparts. The microstructure equivalent to a plastic strain at the onset of Region's II plateau ($15\% \varepsilon^p$) is shown by Figure 4-6b. Similar to the observation by Asgari et. al [44] on FCC – structured low SFE α -brass, a new set of deformation markings (hardly discernable due to their thickness and indicated by arrows) are seen in this micrograph. It is not clear at this moment if the deformation marks correspond to mechanical twins, however, their presence is supported not only by the TEM conclusions of Asgari et. al [44], but also by Deng and coworkers [45] study on non-equiautomic $\text{Fe}_{40}\text{Mn}_{40}\text{Co}_{10}\text{Cr}_{10}$ HEA and by Li and collaborators [13] work on $\text{Al}_{0.3}\text{CoCrFeNi}$. Furthermore, a deformed specimen at a plastic strain of about 40% showed a similar morphology, as shown in Figure 4-6c, except that the density of deformation markings and the lattice curvatures were increased.

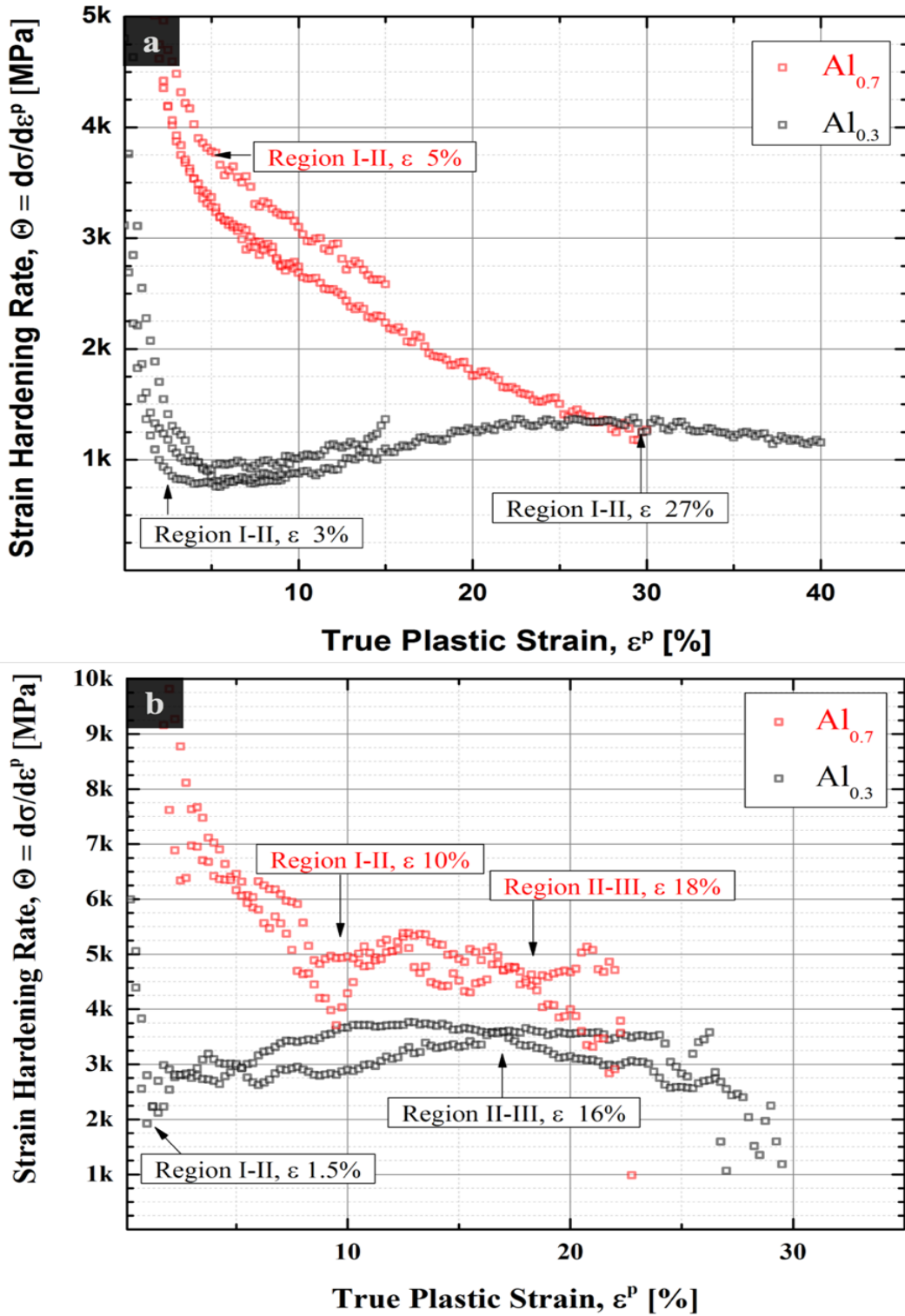


Figure 4-4 Strain hardening rate dependence on true plastic strain $\Theta(\varepsilon^p)$ for quasi-static (b) and high rate compression specimens. It is noted on $\text{Al}_{0.3}$ specimens that the onset of twining is strain rate dependent. Meanwhile, in contrast to the three-stage deformation presented by $\text{Al}_{0.3}$ specimens, a two-stage hardening behavior is observed for the $\text{Al}_{0.7}$ alloy.

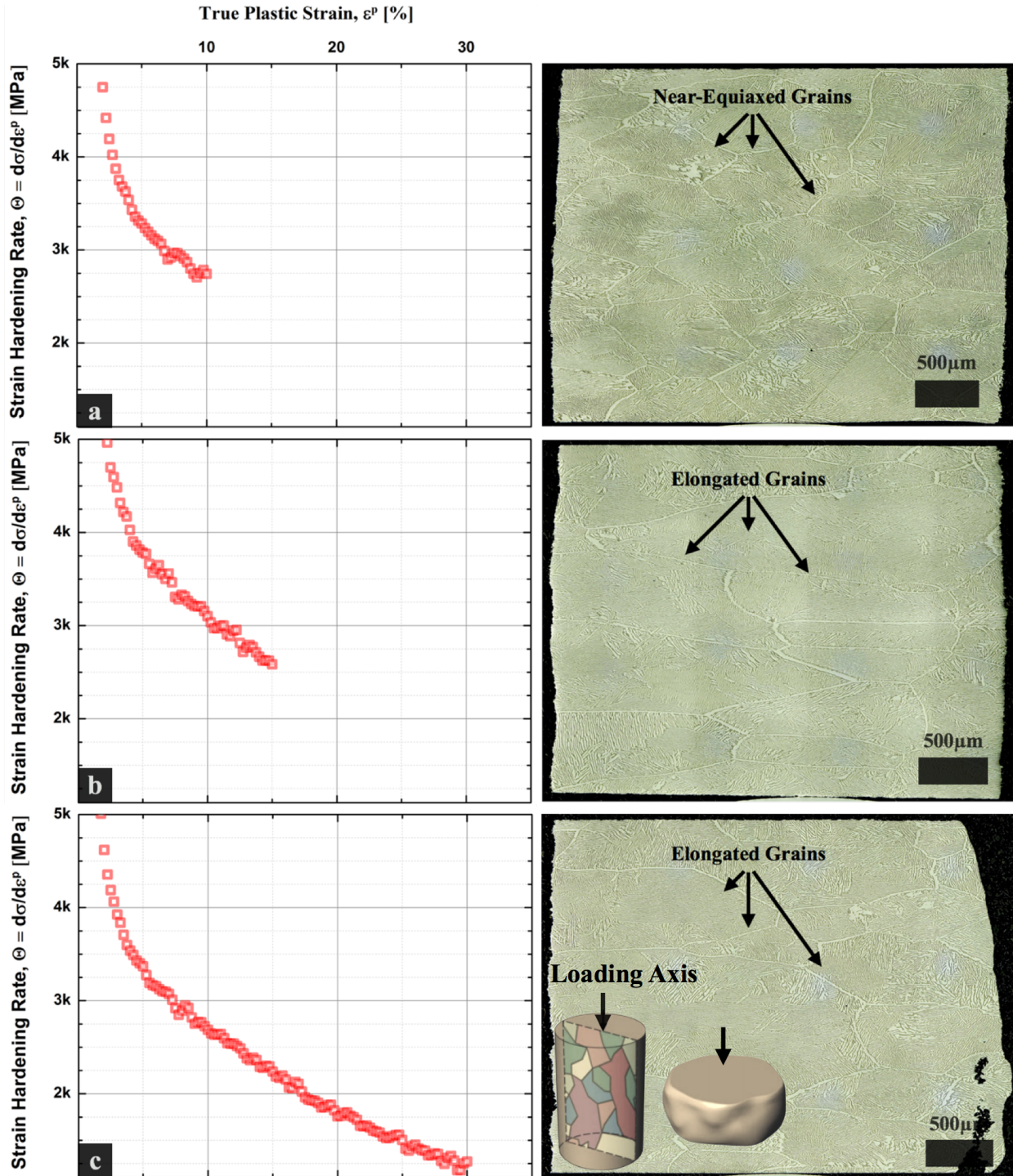


Figure 4.5 Optical photomicrographs documented the microstructural phenomena associated with the various strain hardening stages observed in Al_{0.7} deformed compression specimens. All optical micrographs presented here are from the longitudinal cross-sections of the specimens with the loading direction parallel to the vertical direction on the micrographs. An schematic of a deformed cylindrical specimen with a coarse grain distribution is included as visual reference (reprinted from [46]).

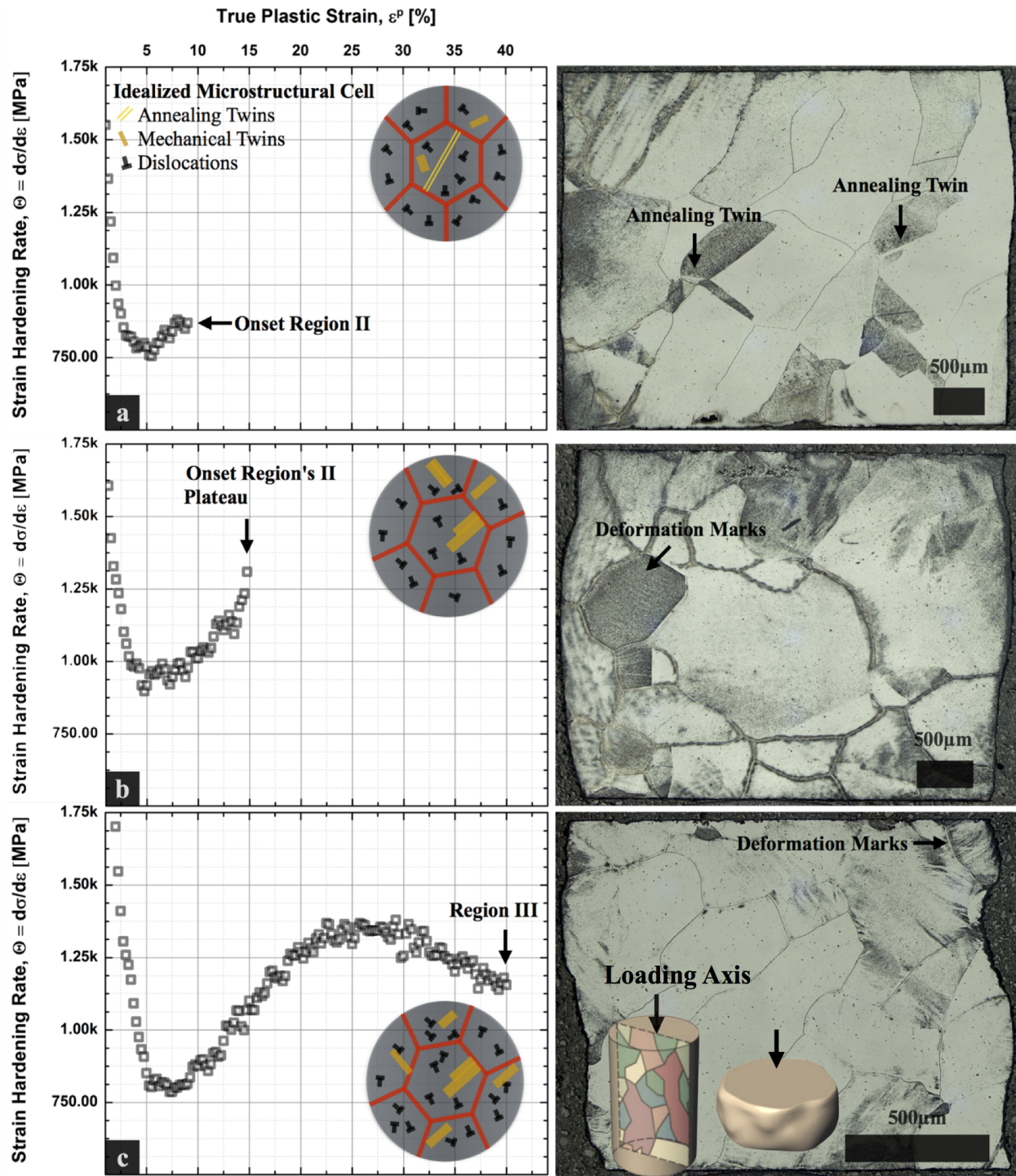


Figure 4.6 Optical photomicrographs documented the microstructural phenomena associated with the various strain hardening stages observed in $\text{Al}_{0.3}$ deformed compression specimens. All optical micrographs presented here are from the longitudinal cross-sections of the specimens with the loading direction parallel to the vertical direction on the micrographs. As plastic deformation progressed the density of deformation marks increased. An schematic of a deformed cylindrical specimen with a coarse grain distribution is included as visual reference (reprinted from [46]).

One should note that the compressive response of the material is a representation of only a few grains as depicted by the cross-section of the deformed specimens. Per optical analysis of cross sections, Al_{0.7} compression specimens exhibited between 7-12 complete grains while 5-9 completed grains per test article were quantified for Al_{0.3}. Grain size effect on flow stress occurs in both the macro and micro-sized specimens, while the specimen geometry size effect is only significant when there is less than 10 grains in the cross-section of specimens [47]. For instance, Komarasamy and collaborators [48] reported not only the expected increase in σ_y after grain refinement for an Al_{0.1}CoCrFeNi HEA, but also a change in the strain hardening mechanism with the reduction in grain size. As concluded by the study, with a reduction in grain size, twin nucleation is suppressed which leads to limited dislocation–twin interactions. Also, as observed in Figure 4-5 and Figure 4-6, and later depicted by Figure 4-8 for tensile specimens, the inhomogeneous deformation, as reflected on the specimen's side profile, is caused by the coarse grain distribution and anisotropic nature [46].

QS ($\dot{\varepsilon} 0.001 \text{ s}^{-1}$) and HR (avg. $\dot{\varepsilon} 1400 \text{ s}^{-1}$) tensile data for the single-phase FCC Al_{0.3} and duplex FCC+BCC type Al_{0.7} specimens are displayed in Figure 4-7 while OM micrographs of the tested gage sections are presented in Figure 4-8. Extensive ductility, and remarkable hardening after yielding, characterized the QS Al_{0.3} specimens. Furthermore, tensile flow curve bears a close resemblance with its QS compression equivalent, i.e., sigmoidal flow pattern. Inside the gage section, inhomogeneous deformation was observed until loss of load bearing capability was recorded by the load cell, although, not physical rupture was attained. Higher σ_y values were computed for the HR dataset Al_{0.3} ($242 \pm 22 \text{ MPa}$) when compared to those obtained at QS rates for the tested samples ($165 \pm 8 \text{ MPa}$). Also in the Al_{0.3} HR dataset, an apparent dynamic recovery region observed at an advanced deformation stage ($>20\% \varepsilon^p$) gives the false impression of flow

softening and subsequent fracture. Rather than this being part of the constitutive behavior of the material, such a response is a product of the analysis tool. The current HR data post-processing software capability is limited to the first loading pulse. High speed imagery shows that the HR Al_{0.3} tensile specimens fracture after the fifth loading pulse. A further numerical treatment would be needed to analyze the stress-strain data after the first loading wave [49], [50].

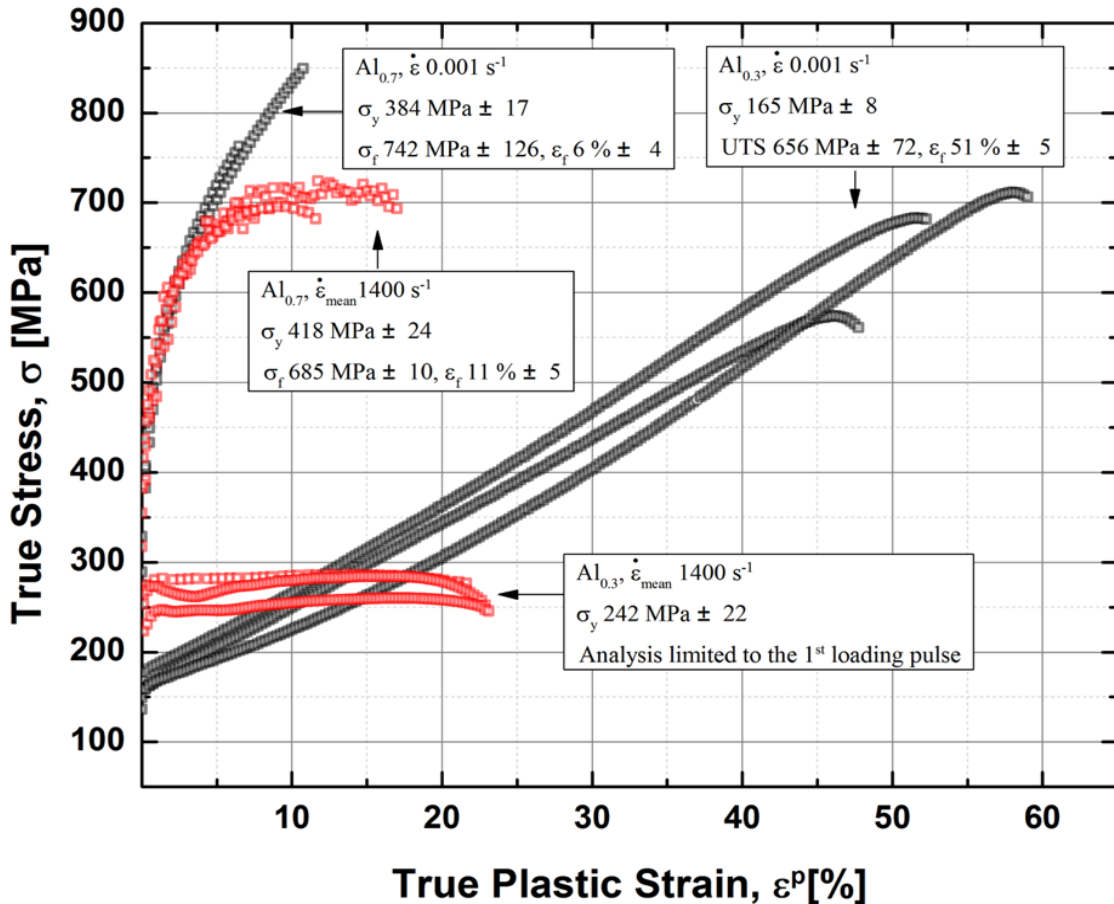


Figure 4-7 Macroscopic response of Al_{0.3} and Al_{0.7} obtained by tensile testing at different deformation rates (0.001, 1400 s⁻¹). Here, the influence Al concentration and microstructural phases is reflected on the strength and ductility levels. Whereas Al_{0.7} specimens present higher strength values its tensile ductility is minimal when compared to Al_{0.3}. Higher σ_y values were computed for the HR dataset when compared against QS counterparts. While Al_{0.7} HR test articles achieved elongation to fracture high speed imagery shows that Al_{0.3} tensile specimens fractured on the fifth loading pulse.

Analogously to the compression deformation mode, Al_{0.7} tensile specimens exhibit greater strength and hardening levels when compared to the Al_{0.3} specimens. Calculated values for the

yield strength for Al_{0.7} QS (348 ± 17 MPa) and HR (418 ± 24 MPa) surpass their Al_{0.3} counterparts by more than 175 MPa. However, scatter in the elongation to fracture data due to grains size prevents an effective diagnostic of the macroscopic mechanical response and their underlying plasticity mechanisms.

Inspection of the Al_{0.7} OM micrographs on the gage section (Figure 4-9) revealed that fracture location coincides not only with the stress concentration region on the specimen, but also with the intersection of columnar and equiaxed-shaped grains. Regarding the stress concentration due to specimen geometry, previous investigations reported that there was not any issue associated with crack initiation at these locations [51]. As concluded, the small specimen thickness induces a prevailing plane stress condition allowing for its redistribution over a bigger area. Recalling the fact that Al_{0.7} specimens were machined from as-cast arc-melted ingots, it is therefore theorized that underformed tensile specimens contain columnar and equiaxed grains, which is a product of a rapid arc melting solidification scheme (refer to Figure 4-9a). Additionally, inhomogeneous microstructural distributions, e.g. varying morphology from surface to center of ingot, on AlCoCrFeNi as-cast HEA ingots has been reported previously [52], [53].

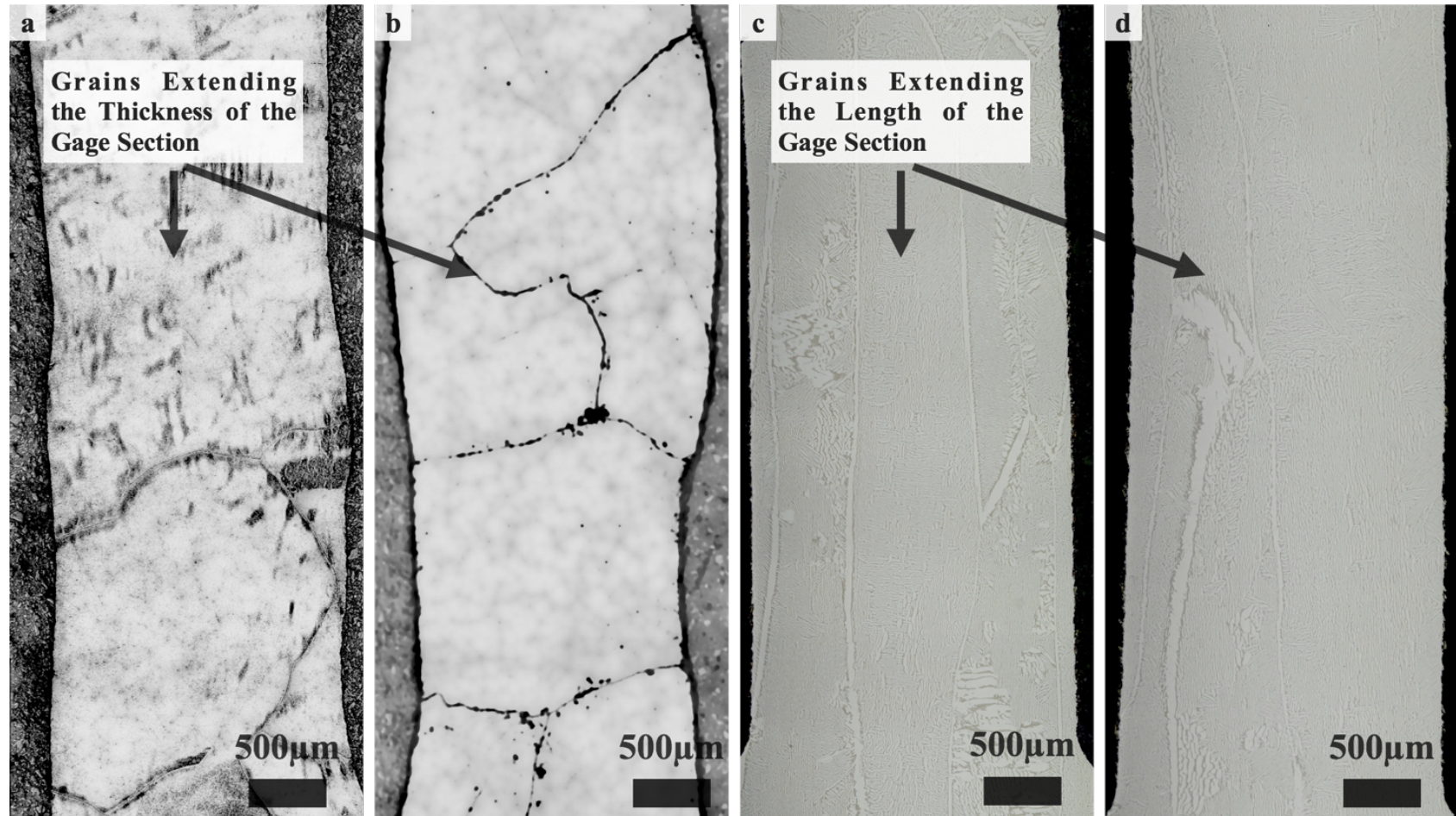


Figure 4-8 OM micrographs reveal the level of structural damage on the gage section of quasi-static (a) and high rate (b) $\text{Al}_{0.3}$ and quasi-static (c) and high rate (d) $\text{Al}_{0.7}$ tensile specimens. Tensile loading axis parallel to the vertical direction on the micrographs. It is noted the inhomogeneous deformation within gage section experienced by the $\text{Al}_{0.3}$ specimens are due to coarse grain size distribution.

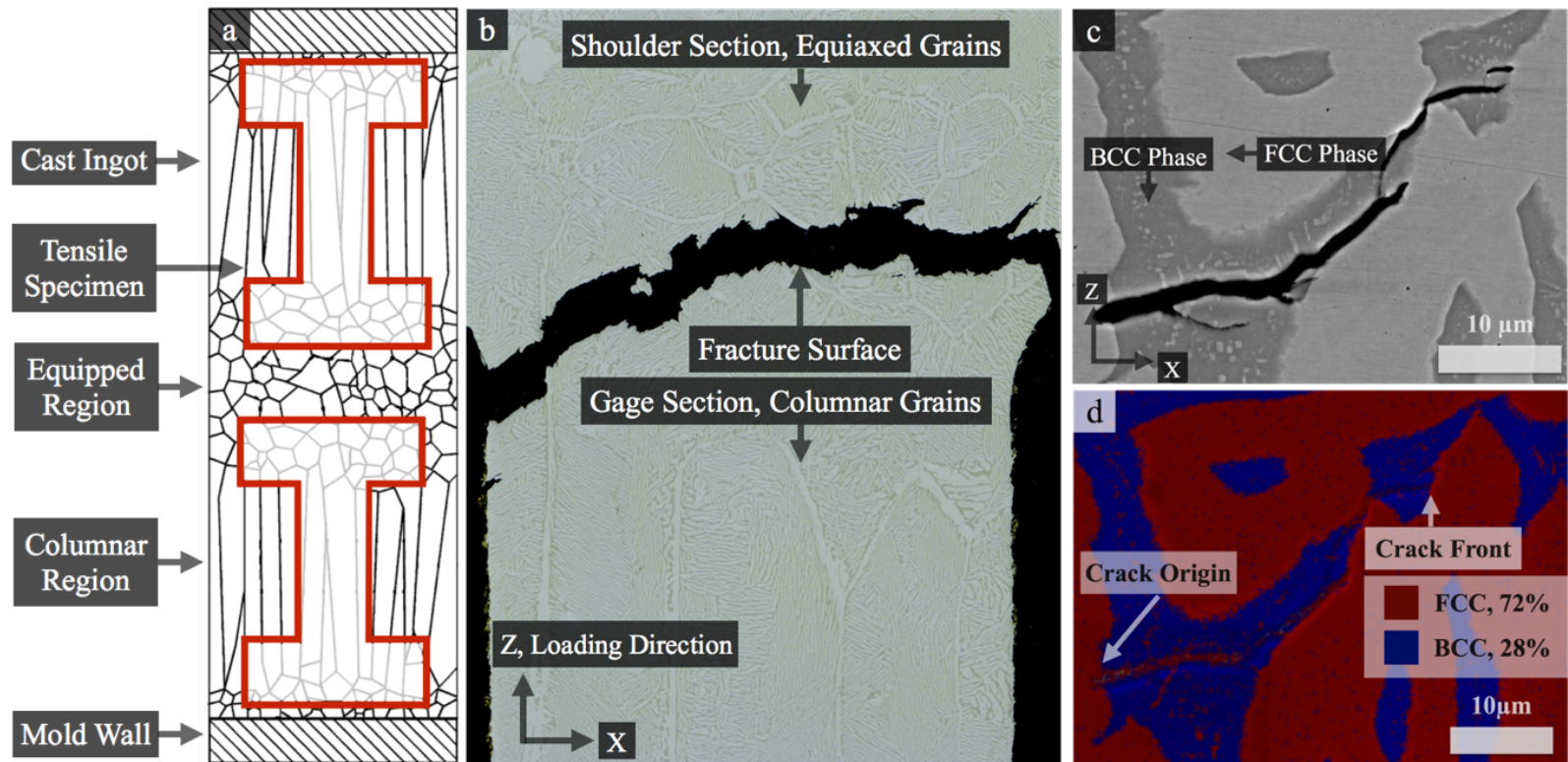


Figure 4-9 Tensile specimen's schematic, superimposed over a cast ingot, illustrates the possibility of equiaxed and columnar grains intersecting at the specimen's stress concentration region. Inserts (b), (c) and (d) displays microstructural features of the fracture on $\text{Al}_{0.7}$. Inset's (d) EDS map displays the fracture initiation and propagation occurred on the less ductile BCC phase.

Lastly, as captured by the EDS detector Figure 4-9 c and d, transgranular fracture crack initiated at the interface between FCC and BCC phased and then propagated through the BCC phase. As stated elsewhere, cracks nucleate at the interfaces as a result of the stresses produced by the elastic incompatibility of the adjacent phases [54]. In connection with, Tang and coworkers [55], investigated the discontinuities in properties between phases (crystallographic and coefficient of thermal expansion) including nanoindentation studies to investigate differences in elastic moduli. As reported, the hardness of the B2 phase (BCC) was more than twice of that of the A1 phase (FCC), and the elastic modulus of the B2 (BCC) phase was approximately 8% higher than that of the A1 (FCC) phase. Because of the difference in compositions and orientations, the elastic moduli of B2 and A1 phases are different, which result in different elastic strains. In agreement with this study Tang and collaborators [55] the SEM micrographs shows a transgranular fracture with initiation point at the interphase between B2 (BCC) and A1 (FCC) phases. Furthermore, on a separate investigation Ghassemali et al. [56] reported similar findings, transgranular crack propagation through BCC phase since a tougher FCC phase acted as a 3D network of obstacles.

In order to utilize these datasets towards insertion into relevant structural applications, it is essential to assess mechanical properties and deformation mechanisms in structures with reduced dimensions. It has been extensively researched that the characteristic microstructural dimensions (intrinsic effect) and specimen size (extrinsic effect) governs the bulk mechanical properties and post-elastic material deformation behavior [57]. As the tensile specimen size is dictated by the dynamic characterization capabilities (i.e. Kolsky bars requires a specific geometry for its specimens to achieve stress equilibrium), attention is turned to grain size dimensions. As concluded from the previous analyses, the average grain size for Al_{0.3} and Al_{0.7} are larger than

both, the thickness and width on the tensile specimens, therefore the macroscopic responses presented does not represent a polycrystalline mechanical behavior.

4.4 Concluding Remarks

To conclude, the influence of Al concentration on the microstructure and mechanical behavior of a $\text{Al}_x\text{CoCrFeNi}$ HEA system has been documented in the form of micrographs and flow stress curves experimentally determined at different stress modes, strain rates, and temperatures. At an Al concentration of a 0.3 molar ratio, a single-phase FCC structure prevails. Traces of BCC phases were detected at $\text{Al}_{0.5}$, while the volume fraction of $\text{Al}_{0.7}$ was calculated to be approximately 70-30 (%) FCC-BCC. The compressive behavior was also influenced by the Al concentration, and its effect on lattice strain and precipitation strengthening. Irrespective of strain rate, yield strength values for $\text{Al}_{0.7}$ were higher than those computed for $\text{Al}_{0.3}$. On the contrary, strain rate influences the deformation behavior of $\text{Al}_{0.7}$. In the case of elevated temperature compression testing, the thermal influence was minimum in the low Al content alloy mechanical behavior while causing considerable thermal softening on the $\text{Al}_{0.7}$ compression test articles. As concluded from strain hardening rate plots, the plastic deformation of the quasi-statically strained $\text{Al}_{0.7}$ was slip dominated while mechanical twins were implied for the dynamic specimens. Meanwhile, twining was deduced for the $\text{Al}_{0.3}$ deformed specimens under quasi-static and high rate conditions. With respect to tensile results, due intrinsic effects (grain size) the macroscopic response is not a polycrystalline representation of the mechanical behavior, although, some general conclusions could be drawn. First, whereas $\text{Al}_{0.3}$ QS tensile results show a sigmoidal flow pattern, remarkable hardening after yielding and extensive ductility interpretation of HR results was limited given the fact that fracture occurred outside the HR data analysis tool processing

window. Meanwhile, crack propagation on $\text{Al}_{0.7}$ occurred through the BCC phase since its capacity to sustain plastic deformation is less than the FCC phase. Finally, inspection of the $\text{Al}_{0.7}$ OM micrographs on the gage section revealed that fracture location coincides not only with the stress concentration region on the specimen, but also with the intersection of columnar and equiaxed-shaped grains. It was theorized that this was caused by a rapid arc melting solidification scheme.

References

- [1] I. S. Wani, T. Bhattacharjee, S. Sheikh, P. P. Bhattacharjee, S. Guo, and N. Tsuji, “Materials Science & Engineering A eutectic high entropy alloy using thermo-mechanical processing,” *Mater. Sci. Eng. A*, vol. 675, pp. 99–109, 2016.
- [2] N. Kumar *et al.*, “High strain-rate compressive deformation behavior of the Al0.1CrFeCoNi high entropy alloy,” *Mater. Des.*, vol. 86, pp. 598–602, 2015.
- [3] D. Li *et al.*, “High-entropy Al 0.3 CoCrFeNi alloy fibers with high tensile strength and ductility at ambient and cryogenic temperatures,” *Acta Mater.*, vol. 123, pp. 285–294, 2017.
- [4] G. Hu, D. Zhang, T. Tang, X. Shen, and L. Jiang, “Effects of Nd addition on microstructure and mechanical properties of Mg – 6Zn – 1Mn – 4Sn alloy,” *Mater. Sci. Eng. A*, vol. 634, pp. 5–13, 2015.
- [5] Z. Tang *et al.*, “Aluminum alloying effects on lattice types, microstructures, and mechanical behavior of high-entropy alloys systems,” *Jom*, vol. 65, no. 12, pp. 1848–1858, 2013.
- [6] C. Li, J. C. Li, M. Zhao, and Q. Jiang, “Effect of aluminum contents on microstructure and properties of Al_xCoCrFeNi alloys,” *J. Alloys Compd.*, vol. 504, pp. S515–S518, 2010.
- [7] D. Li and Y. Zhang, “The ultrahigh charpy impact toughness of forged Al_xCoCrFeNi high entropy alloys at room and cryogenic temperatures,” *Intermetallics*, vol. 70, no. July, pp. 24–28, 2016.
- [8] M. Komarasamy, K. Alagarsamy, and R. S. Mishra, “Serration behavior and negative strain rate sensitivity of Al0.1CoCrFeNi high entropy alloy,” *Intermetallics*, vol. 84, pp. 20–24, 2017.
- [9] H. Y. Yasuda, K. Shigeno, and T. Nagase, “Dynamic strain aging of Al0.3CoCrFeNi high entropy alloy single crystals,” *Scr. Mater.*, vol. 108, pp. 80–83, 2015.
- [10] T. T. Shun and Y. C. Du, “Microstructure and tensile behaviors of FCC Al0.3CoCrFeNi high entropy alloy,” *J. Alloys Compd.*, vol. 479, no. 1–2, pp. 157–160, 2009.
- [11] Y. F. Kao, T. J. Chen, S. K. Chen, and J. W. Yeh, “Microstructure and mechanical property of as-cast, homogenized, and deformed Al_xCoCrFeNi high-entropy alloys,” *J. Alloys Compd.*, vol. 488, no. 1, pp. 57–64, 2009.
- [12] J. Joseph, N. Stanford, P. Hodgson, and D. M. Fabijanic, “Tension/compression asymmetry in additive manufactured face centered cubic high entropy alloy,” *Scr. Mater.*, vol. 129, pp.

30–34, 2017.

- [13] Z. Li, S. Zhao, H. Diao, P. K. Liaw, and M. A. Meyers, “High-velocity deformation of remarkable resistance to shear failure,” *Sci. Rep.*, pp. 1–8, 2017.
- [14] C. Tong *et al.*, “Mechanical Performance of the Al x CoCrCuFeNi High-Entropy Alloy System with Multiprincipal Elements,” *Metall. Mater. Trans. A*, vol. 36, no. May, pp. 1263–1271, 2005.
- [15] C. Tsai, Y. Chen, M. Tsai, J. Yeh, T. Shun, and S. Chen, “Deformation and annealing behaviors of high-entropy alloy Al0.5CoCrCuFeNi,” *J. Alloys Compd.*, vol. 486, no. 2009, pp. 427–435, 2010.
- [16] C. Tsai, M. Tsai, J. Yeh, and C. Yang, “Effect of temperature on mechanical properties of Al 0 . 5 CoCrCuFeNi wrought alloy,” *J. Alloys Compd.*, vol. 490, pp. 160–165, 2010.
- [17] M. Tsai *et al.*, “Intermetallics Morphology , structure and composition of precipitates in Al0.3 CoCrCu 0.5 FeNi high-entropy alloy,” *Intermetallics*, vol. 32, pp. 329–336, 2013.
- [18] L. H. Wen, H. C. Kou, J. S. Li, H. Chang, X. Y. Xue, and L. Zhou, “Effect of aging temperature on microstructure and properties of AlCoCrCuFeNi high-entropy alloy,” *Intermetallics*, vol. 17, pp. 266–269, 2009.
- [19] A. V. Kuznetsov, D. G. Shaysultanov, N. D. Stepanov, G. A. Salishchev, and O. N. Senkov, “Tensile properties of an AlCrCuNiFeCo high-entropy alloy in as-cast and wrought conditions,” *Mater. Sci. Eng. A*, vol. 533, pp. 107–118, 2012.
- [20] W. Wang, W. Wang, S. Wang, Y. Tsai, C. Lai, and J. Yeh, “Effects of Al addition on the microstructure and mechanical property of AlxCoCrFeNi high-entropy alloys,” *Intermetallics*, vol. 26, pp. 44–51, 2012.
- [21] A. M. Giwa, P. K. Liaw, K. A. Dahmen, and J. R. Greer, “Microstructure and small-scale size effects in plasticity of individual phases of Al0.7 CoCrFeNi High Entropy alloy,” *Extrem. Mech. Lett.*, vol. 8, pp. 220–228, 2016.
- [22] M. Tsai, J. Yeh, M. Tsai, and J. Yeh, “High-Entropy Alloys : A Critical Review,” *Mater. Res. Lett.*, vol. 3831, no. February, 2014.
- [23] W. R. Whittington *et al.*, “Capturing the effect of temperature, strain rate, and stress state on the plasticity and fracture of rolled homogeneous armor (RHA) steel,” *Mater. Sci. Eng. A*, vol. 594, pp. 82–88, Jan. 2014.
- [24] P. G. Allison, H. Grewal, Y. Hammi, H. R. Brown, W. R. Whittington, and M. F. Horstemeyer, “Plasticity and Fracture Modeling/Experimental Study of a Porous Metal Under Various Strain Rates, Temperatures, and Stress States,” *J. Eng. Mater. Technol.*, vol. 135, no. 4, p. 41008, Sep. 2013.

- [25] P. G. Allison, M. F. Horstemeyer, Y. Hammi, H. R. Brown, M. T. Tucker, and Y.-K. Hwang, “Microstructure–property relations of a steel powder metal under varying temperatures, strain rates, and stress states,” *Mater. Sci. Eng. A*, vol. 529, pp. 335–344, Nov. 2011.
- [26] C. Weinong and S. BO, *Split Hopkinson (Kolsky) Bar*, vol. 1. 2013.
- [27] D. K. Francis, W. R. Whittington, W. B. Lawrimore, P. G. Allison, S. A. Turnage, and J. J. Bhattacharyya, “Split Hopkinson Pressure Bar Graphical Analysis Tool,” *Exp. Mech.*, vol. 57, no. 1, pp. 179–183, 2017.
- [28] J. W. Yeh *et al.*, “Nanostructured high-entropy alloys with multiple principal elements: Novel alloy design concepts and outcomes,” *Adv. Eng. Mater.*, vol. 6, no. 5, p. 299–303+274, 2004.
- [29] O. L. Rodriguez *et al.*, “Dynamic tensile behavior of electron beam additive manufactured Ti6Al4V,” *Mater. Sci. Eng. A*, vol. 641, pp. 323–327, 2015.
- [30] C. Zhang *et al.*, “Understanding phase stability of Al-Co-Cr-Fe-Ni high entropy alloys,” *Mater. Des.*, vol. 109, pp. 425–433, 2016.
- [31] D. B. Miracle and O. N. Senkov, “A critical review of high entropy alloys and related concepts,” *Acta Mater.*, vol. 122, pp. 448–511, 2017.
- [32] B. S. Murty, J.-W. Yeh, and S. Ranganathan, *High Entropy Alloys*, 1st ed. San Diego: Butterworth-Heinemann, 2014.
- [33] C. Weinong and B. Song, *Split Hopkinson (Kolsky) Bar: Design, Testing and Applications*, 1st ed. New York: Springer International Publishing, 2010.
- [34] R. Abbaschian, L. Abbaschian, and R. E. Reed-Hill, *Physical Metallurgy Principles*, 4th ed. CL Engineering, 2009.
- [35] G. Thomas and J. Washburn, Eds., *Electron microscopy and the strength of crystals*. New York: Interscience Publishers, 1963.
- [36] A. Rohatgi, K. S. Vecchio, and G. T. Gray III, “The influence of stacking fault energy on the mechanical behavior of cu and cu-al alloys: deformation twinning, work hardening, and dynamic recovery,” *Metall. Mater. Trans. A*, vol. 32, pp. 135–145, 2001.
- [37] I. Gutierrez-Urrutia and D. Raabe, “Dislocation and twin substructure evolution during strain hardening of an Fe – 22 wt.% Mn – 0.6 wt.% C TWIP steel observed by electron channeling contrast imaging,” *Acta Mater.*, vol. 59, pp. 6449–6462, 2011.
- [38] E. El-Danaf, S. R. Kalidindi, and R. D. Doherty, “Influence of grain size and stacking-fault

energy on deformation twinning in fcc metals,” *Metall. Mater. Trans. A*, vol. 30, no. May, pp. 1223–1233, 1999.

- [39] V. Caballero and S. K. Varma, “Effect of stacking fault energy and strain rate on the microstructural evolution during room temperature tensile testing in Cu and Cu-Al dilute alloys,” *J. Mater. Sci.*, vol. 4, pp. 461–468, 1999.
- [40] Y. Wei *et al.*, “Evading the strength-ductility trade-off dilemma in steel through gradient hierarchical nanotwins.,” *Nat. Commun.*, vol. 5, p. 3580, 2014.
- [41] Z. Tang *et al.*, “Tensile ductility of an AlCoCrFeNi multi-phase high-entropy alloy through hot isostatic pressing (HIP) and homogenization,” *Mater. Sci. Eng. A*, vol. 647, pp. 229–240, 2015.
- [42] Q. H. Tang, Y. Huang, Y. Y. Huang, X. Z. Liao, T. G. Langdon, and P. Q. Dai, “Hardening of an Al 0.3 CoCrFeNi high entropy alloy via high-pressure torsion and thermal annealing,” *Mater. Lett.*, vol. 151, pp. 126–129, 2015.
- [43] Y. H. Zhao and Y. T. Zhu, “Tailoring stacking fault energy for high ductility and high strength in ultrafine grained Cu and its alloy,” *Appl. Phys. Lett.*, vol. 89, pp. 1–4, 2006.
- [44] S. Asgari, E. El-danaf, S. R. Kalidindi, and R. D. Doherty, “Strain Hardening Regimes and Microstructural Evolution during Large Strain Compression of Low Stacking Fault Energy Fcc Alloys That Form Deformation Twins,” *Metall. Mater. Trans. A*, vol. 28, no. September, 1997.
- [45] Y. Deng, C. C. Tasan, K. G. Pradeep, H. Springer, A. Kostka, and D. Raabe, “Design of a twinning-induced plasticity high entropy alloy,” *Acta Mater.*, vol. 94, pp. 124–133, 2015.
- [46] M. W. Fu and W. L. Chan, *Micro-scaled Products Development via Microforming*. Springer, 2014.
- [47] F. Vollertsen, H. Schulze Niehoff, and Z. Hu, “State of the art in micro forming,” *Int. J. Mach. Tools Manuf.*, vol. 46, no. 11 SPEC. ISS., pp. 1172–1179, 2006.
- [48] M. Komarasamy, N. Kumar, Z. Tang, R. S. Mishra, and P. K. Liaw, “Effect of Microstructure on the Deformation Mechanism of Friction Stir-Processed Al 0.1 CoCrFeNi High Entropy Alloy Effect of Microstructure on the Deformation Mechanism of Friction Stir-Processed,” *Mater. Resseach Lett.*, vol. 3831, no. April 2017, pp. 0–5, 2015.
- [49] H. Zhao and G. Gary, “A new method for the separation of waves. Application to the SHPB technique for an unlimited duration of measurement,” *J. Mech. Phys. Solids*, vol. 45, no. 7, pp. 1185–1202, 1997.
- [50] S. W. Park and M. Zhou, “Separation of Elastic Waves in Split Hopkinson Bars Using One-point Strain Measurements,” *Exp. Mech.*, p. 77, 1998.

- [51] P. Konopi, “Micro-Tensile Test Technique Development and Application to Mechanical Property Determination,” in *ASTM Sixth International Symposium on Small Specimen Test Techniques*, 2014, vol. 6, pp. 12–30.
- [52] M. C. Gao, J. W. Yeh, P. K. Liaw, and Y. Zhang, *High-Entropy Alloys Fundamentals and Applications*. Springer International Publishing, 2014.
- [53] Y. Zhang, S. G. Ma, and J. W. Qiao, “Morphology transition from dendrites to equiaxed grains for AlCoCrFeNi high-entropy alloys by copper mold casting and bridgman solidification,” *Metall. Mater. Trans. A Phys. Metall. Mater. Sci.*, vol. 43, no. 8, pp. 2625–2630, 2012.
- [54] L. E. Murr, *Interfacial phenomena in metals and alloys*. Addison-Wesley Pub. Co., Advanced Book Program, 1975.
- [55] Z. Tang *et al.*, “Tensile ductility of an AlCoCrFeNi multi-phase high-entropy alloy through hot isostatic pressing (HIP) and homogenization,” *Mater. Sci. Eng. A*, vol. 647, pp. 229–240, 2015.
- [56] E. Ghassemali, R. Sonkusare, K. Biswas, and N. P. Guroo, “In-situ study of crack initiation and propagation in a dual phase AlCoCrFeNi high entropy alloy,” *J. Alloys Compd.*, vol. 710, pp. 539–546, 2017.
- [57] Y. Z. Tian, L. J. Zhao, S. Chen, A. Shibata, Z. F. Zhang, and N. Tsuji, “Significant contribution of stacking faults to the strain hardening behavior of Cu-15%Al alloy with different grain sizes,” *Sci. Rep.*, vol. 5, no. October, p. 16707, 2015.

CHAPTER 5 SUMMARY AND FUTURE DIRECTIONS

The foundation of this doctoral dissertation effort is rooted at the intersection of material science and mechanical engineering. Among the fundamental tenets guiding material science is that the properties (thermal, optical, mechanical, physical, chemical and nuclear) of any given material are determined by its structure. Additionally, the structure is dictated by processing parameters. Therefore, it is on the basis of these processing parameters – structure – properties interplays that an engineer can design an industry-specific component with a pre-determined set of properties. While this research provides a number of important insights on initial, post-processed, deformed and fractured morphologies the main contribution was on expanding the first-tier mechanical properties library of aerospace-grade materials intended for structural/critical applications. To the author knowledge, this dissertation represents the first documented attempt to report monotonic mechanical properties at different deformation rates, temperatures and states while analyzing its results in terms of deformation mechanisms and post-mortem morphologies.

Chapter 2 documents the plastic tensile and compressive behavior of an EBM Ti6Al4V with its corresponding strain hardening rate responses and fracture morphologies at varying strain rates and temperatures. Notice that, unlike Chapter 3, no thermal post-processes were performed on the test articles. Although, as shown in Chapter 3, thermal post-processes are recommended for PBF techniques, EBM as-built components have relative low levels of residual stresses when

compared against SLM build parts. In addition, only scarce volumetric microdefects (powder-induced porosity) were detected on the EBM Ti6Al4V as-built specimens.

Focusing on microstructural characteristics, EBM Ti6Al4V and SLM IN718 displayed columnar grains, that extend across multiple layers, parallel to deposition direction. Although, their differences in morphology are striking between the two materials, where the EBM Ti6Al4V exhibited coarse, homo-epitaxial growth, the SLM IN718 as-built microstructure is composed of fine, irregular, columnar grains. The metallurgy of an AM deposited material is determined by feedstock chemistry and process thermal history. An understanding, based on first principles, of thermo-mechanical cycles, solidification, solid-state phase transformations, residual stresses (magnitude and distribution) and geometrical distortions of AM material signify an experimental endeavor that could last several years and cost millions of dollars, therefore, it was not within the scope of this dissertation. In this context, an Integrated Computational Materials Engineering (ICME) approach for AM, as a simulation tool with prediction capabilities, should be adopted in order to expedite developmental efforts.

Given the stringent requirements that the aerospace sector imparts on structural materials, thermal post-processes are often used to alleviate residual stresses, eradicate volumetric defects, enhance mechanical properties, and eliminate the degree of material anisotropy. Therefore, Chapter 3 focused on the thermal post-processes influence on morphology and tensile plastic flow of an SLM IN718 superalloy. Microstructural investigations revealed a transformation from the as-built columnar, melt pool morphology to an isotropic, dendrite-free, architectural arrangement after a series of standard thermal post-processes (stress relief, hot isostatic pressing and homogenization and solution heat treatments). From the improvement in the tensile strengths observed under quasi-static and high rate deformation conditions, it was concluded that that the

precipitation of strengthening phases, which was the main goal of the STA heat treatment, was achieved. Still, evidence of the precipitation of the aforementioned phases is needed in the form of high resolution imagery, Transmission Electron Microscopy (TEM) and/or X-Ray Diffraction (XRD) analysis.

The macroscopic response of EBM Ti6Al4V was studied under different stress states (tension and compression), deformation rates (0.001 s^{-1} and 1500 s^{-1}) and temperatures ($23 - 500^\circ\text{C}$). The results identified that, (a) compressive yield strengths are higher than their tensile counterparts, (b) the strength differential effect is more prominent under high strain rates, and (c) the thermal softening was the dominant phenomena controlling the HR-elevated temperature compressive flow stresses. The mechanical behavior was explained in terms of deformation mechanisms reasoned from close inspection of strain hardening rate curves. With respect to SLM IN718, due to the limited number of specimens the analysis was limited to elucidating the post processing influence on the strain rate dependence of the material through ambient temperature QS and HR tension experiments. As reported in Chapter 3, yield (σ_y) and ultimate tensile (UTS) strengths increase with each sequential post-processing step while elongation to failure (ε_f) values decrease. The improvement in strength is attributed to precipitation of the γ' and γ'' strengthening phases. In addition, high rate tensile results exhibited the classical positive correlation with strength whereas, as expected, a negative correlation is observed between strain rate and ε_f . Despite the experimental work done on mechanical behavior some areas remain unexplored:

- **Anisotropy and thermal-post processes influence on EBM Ti6Al4V mechanical properties:** the mechanical characterization activities of this study were limited to the as-built condition strained in only one direction – the loading axis normal to

deposited layers. For instance, although minimal, the data collected from other researchers. Table 1-1 shows that PBF AM Ti6Al4V tensile results exhibited a level of anisotropy. Thus, additional research efforts are needed on this area.

On the contrary, thermal post-processes influence, significantly, tensile strengths and ductility values. Given the stringent requirements that the aerospace sector imparts on structural materials, thermal post-processes are often used, hence, additional characterization activities are suggested to elucidate the thermal post- processes influence.

- **Corroborate EBM Ti6Al4V deformation mechanisms:** via close inspection of strain hardening rate curves, the presence of mechanical twinning, as relevant plasticity contributors, on tensile test articles was detected. However, visual confirmation is required in the form of TEM studies.
- **EBM Ti6Al4V and SLM IN718 fatigue behavior:** this dissertation was focused on the monotonic, uniaxial tensile and compressive responses of EBMTi6Al4V and SLM IN718. Still, fatigue behavior is of importance to the aerospace industry as often it is considered a limiting property for material selection, therefore, a series of fatigue tests are recommended.
- **SLM IN718 stress asymmetry and anisotropy:** this research studied the tensile behavior, under different deformation rates, of coupons machined in only one direction with respect to build axis. Future investigations on stress asymmetry and anisotropy are suggested.

Finally, chapter 4 summarized the findings on low and high Al content ($\text{Al}_{0.3}$ and $\text{Al}_{0.7}$) HEAs. The $\text{Al}_{0.3}$ HEA exhibited a FCC microstructure with sigmoidal plastic behavior

suggesting multiple deformation mechanisms occurring in the material. As expected, higher values of flow stresses were recorded as the strain rate increase. With respect to Al_{0.7}, it consisted of a multi-phase FCC and BCC type microstructure that exhibited a linear hardening behavior. As shown by the mechanical data across strain rate scales, the precipitation of a second phase, BCC type, influence positively the alloy strength.

Elevated temperature compression testing provided the most interesting results. The combination of high elevated-temperature strength, excellent thermal stability, and enhanced ductility makes HEAs a potential candidate material system for high-temperature applications, however, stringent controls over the manufacturing processes are required to ensure their success.

REFERENCES

- [1] U. S. A. Office, “Opportunities, Challenges, and Policy Implications of Additive Manufacturing,” 2015.
- [2] E. Sachs *et al.*, “Three-Dimensional Printing: The Physics and Implications of Additive Manufacturing,” *Ann. CIRP*, vol. 42, pp. 257–260, 1993.
- [3] I. Gibson and D. P. Shi, “Material properties and fabrication parameters in selective laser sintering process,” *Rapid Prototyp. J.*, vol. 3, no. 4, pp. 129–136, 1997.
- [4] J.-P. Kruth, M. C. Leu, and T. Nakagawa, “Progress in Additive Manufacturing and Rapid Prototyping,” *CIRP Ann. - Manuf. Technol.*, vol. 47, no. 2, pp. 525–540, 1998.
- [5] J. G. Zhou, D. Herscovici, and C. C. Chen, “Parametric process optimization to improve the accuracy of rapid prototyped stereolithography parts,” *Int. J. Mach. Tools Manuf.*, vol. 40, no. 3, pp. 363–379, 2000.
- [6] D. Hu, R. Kovacevic, and Sensing, “Modeling and control for laser-based additive manufacturing,” *Int. J. Mach. Tools Manuf.*, vol. 43, no. 1, pp. 51–60, 2003.
- [7] X. Gong, “Microstructural Characterization and Modeling of Ti6Al4V Parts Made By Electron Beam Additive Manufacturing,” The University of Alabama, 2014.
- [8] G. Hu, D. Zhang, T. Tang, X. Shen, and L. Jiang, “Effects of Nd addition on microstructure and mechanical properties of Mg – 6Zn – 1Mn – 4Sn alloy,” *Mater. Sci. Eng. A*, vol. 634, pp. 5–13, 2015.
- [9] D. B. Miracle, J. D. Miller, O. N. Senkov, C. Woodward, M. D. Uchic, and J. Tiley, “Exploration and development of high entropy alloys for structural applications,” *Entropy*, vol. 16, no. 1, pp. 494–525, 2014.
- [10] D. B. Miracle, “High entropy alloys and their development as structural materials,” *Mater. Sci. Technol.*, vol. 0, no. 0, p. 1743284714Y.000, 2015.
- [11] F. Otto, C. Somsen, H. Bei, G. Eggeler, and E. P. George, “The influences of temperature and microstructure on the tensile properties of a CoCrFeMnNi high-entropy alloy,” *Acta Mater.*, vol. 61, no. 15, pp. 5743–5755, 2013.
- [12] Z. Tang *et al.*, “Aluminum alloying effects on lattice types, microstructures, and mechanical behavior of high-entropy alloys systems,” *Jom*, vol. 65, no. 12, pp. 1848–1858, 2013.

- [13] Z. Tang *et al.*, “Tensile ductility of an AlCoCrFeNi multi-phase high-entropy alloy through hot isostatic pressing (HIP) and homogenization,” *Mater. Sci. Eng. A*, vol. 647, pp. 229–240, 2015.
- [14] R. Ding, Z. X. Guo, and A. Wilson, “Microstructural evolution of a Ti – 6Al – 4V alloy during thermomechanical processing,” *Mater. Sci. Eng. A*, vol. 327, pp. 233–245, 2002.
- [15] L. E. Murr *et al.*, “Metal Fabrication by Additive Manufacturing Using Laser and Electron Beam Melting Technologies,” *J. Mater. Sci. Technol.*, vol. 28, no. 1, pp. 1–14, 2012.
- [16] C. Kai Chua, K. Fai Leong, and C. Sing Lim, *Rapid prototyping: principles and applications*, 3rd ed. World Scientific Publishing Company, 2010.
- [17] ASTM F42, “F2792 – 12a Additive Manufacturing Technologies.” 2013.
- [18] W. J. Sames, F. A. List, S. Pannala, R. R. Dehoff, and S. S. Babu, “The metallurgy and processing science of metal additive manufacturing,” *Int. Mater. Rev.*, vol. 6608, no. March, 2016.
- [19] B. Dutta and F. H. Froes, “The additive manufacturing (AM) of titanium alloys,” in *Titanium powder metallurgy: science, technology and applications*, Elsevier Inc., 2015, pp. 447–468.
- [20] M. A. Meyers, G. Subhash, B. K. Kad, and L. Prasad, “Evolution of microstructure and shear-band formation in α -hcp titanium,” *Mech. Mater.*, vol. 17, no. 2–3, pp. 175–193, 1994.
- [21] M. G. da Silva and K. T. Ramesh, “The rate-dependent deformation and localization of fully dense and porous Ti-6Al-4V,” *Mater. Sci. Eng. A*, vol. 232, no. 1–2, pp. 11–22, 1997.
- [22] S. Liao and J. Duffy, “Adiabatic shear bands in a Ti-6Al-4V titanium alloy,” *J. Mech. Phys. Solids*, vol. 46, pp. 2201–2231, 1998.
- [23] S. Nemat-Nasser, W. G. Guo, V. F. Nesterenko, S. S. Indrakanti, and Y. B. Gu, “Dynamic response of conventional and hot isostatically pressed Ti-6Al-4V alloys: Experiments and modeling,” *Mech. Mater.*, vol. 33, no. 8, pp. 425–439, 2001.
- [24] W.-S. Lee and C.-F. Lin, “Plastic deformation and fracture behaviour of Ti-6Al-4V alloy loaded with high strain rate under various temperatures,” *Mater. Sci. Eng. A*, vol. 241, no. 1–2, pp. 48–59, 1998.
- [25] X. Liu, C. Tan, J. Zhang, F. Wang, and H. Cai, “Correlation of adiabatic shearing behavior with fracture in Ti-6Al-4V alloys with different microstructures,” *Int. J. Impact Eng.*, vol. 36, no. 9, pp. 1143–1149, 2009.
- [26] D. Rittel and Z. G. Wang, “Thermo-mechanical aspects of adiabatic shear failure of AM50 and Ti6Al4V alloys,” *Mech. Mater.*, vol. 40, no. 8, pp. 629–635, 2008.

- [27] P. Landau, a. Venkert, and D. Rittel, “Microstructural aspects of adiabatic shear failure in annealed Ti6Al4V,” *Metall. Mater. Trans. A Phys. Metall. Mater. Sci.*, vol. 41, no. 2, pp. 389–396, 2010.
- [28] C. Zheng *et al.*, “Capturing of the propagating processes of adiabatic shear band in Ti–6Al–4V alloys under dynamic compression,” *Mater. Sci. Eng. A*, vol. 658, pp. 60–67, 2016.
- [29] F. Martinez, L. E. Murr, a. Ramirez, M. I. Lopez, and S. M. Gaytan, “Dynamic deformation and adiabatic shear microstructures associated with ballistic plug formation and fracture in Ti-6Al-4V targets,” *Mater. Sci. Eng. A*, vol. 454–455, pp. 581–589, 2007.
- [30] N. Biswas, J. L. Ding, V. K. Balla, D. P. Field, and a. Bandyopadhyay, “Deformation and fracture behavior of laser processed dense and porous Ti6Al4V alloy under static and dynamic loading,” *Mater. Sci. Eng. A*, vol. 549, pp. 213–221, 2012.
- [31] P. Li, W. Guo, W. Huang, Y. Su, X. Lin, and K. Yuan, “Thermomechanical response of 3D laser-deposited Ti – 6Al – 4V alloy over a wide range of strain rates and temperatures,” *Mater. Sci. Eng. A*, vol. 647, pp. 34–42, 2015.
- [32] A. Mohammadhosseini, S. H. Masood, D. Fraser, and M. Jahedi, “Dynamic compressive behaviour of Ti-6Al-4V alloy processed by electron beam melting under high strain rate loading,” *Adv. Manuf.*, vol. 3, no. 3, pp. 232–243, 2015.
- [33] O. L. Rodriguez *et al.*, “Dynamic tensile behavior of electron beam additive manufactured Ti6Al4V,” *Mater. Sci. Eng. A*, vol. 641, pp. 323–327, 2015.
- [34] L. E. Murr *et al.*, “Microstructures and mechanical properties of electron beam-rapid manufactured Ti-6Al-4V biomedical prototypes compared to wrought Ti-6Al-4V,” *Mater. Charact.*, vol. 60, no. 2, pp. 96–105, 2009.
- [35] G. G. Yapici, I. Karaman, Z. P. Luo, and H. Rack, “Microstructure and mechanical properties of severely deformed powder processed Ti-6Al-4V using equal channel angular extrusion,” *Scr. Mater.*, vol. 49, no. 10 SPEC., pp. 1021–1027, 2003.
- [36] B. Baufeld, O. van der Biest, R. Gault, and K. Ridgway, “Manufacturing Ti-6Al-4V Components by Shaped Metal Deposition: Microstructure and Mechanical Properties,” *Mater. Sci. Eng.*, vol. 26, p. 12001, 2011.
- [37] J. T. Hammer, “Plastic Deformation and Ductile Fracture of Ti-6Al-4V under Various Loading Conditions,” The Ohio State University, 2012.
- [38] S. Nemat-Nasser, W. G. Guo, and J. Y. Cheng, “Mechanical properties and deformation mechanisms of a commercially pure titanium,” *Acta Mater.*, vol. 47, no. 13, pp. 3705–3720, 1999.
- [39] D. R. Chichili, K. T. Ramesh, and K. J. Hemker, “The high-strain-rate response of alpha-

titanium: experiments, deformation mechanisms and modeling,” *Acta Mater.*, vol. 46, no. 3, pp. 1025–1043, 1998.

- [40] A. Roth, M. A. Lebyodkin, T. A. Lebedkina, J. S. Lecomte, T. Richeton, and K. E. K. Amouzou, “Mechanisms of anisotropy of mechanical properties of alpha-titanium in tension conditions,” *Mater. Sci. Eng. A*, vol. 596, pp. 236–243, 2014.
- [41] A. A. Salem, S. R. Kalidindi, and R. D. Doherty, “Strain hardening regimes and microstructure evolution during large strain compression of high purity titanium,” *Scr. Mater.*, vol. 46, no. 6, pp. 419–423, 2002.
- [42] A. A. Salem, S. R. Kalidindi, and R. D. Doherty, “Strain hardening of titanium: Role of deformation twinning,” *Acta Mater.*, vol. 51, no. 14, pp. 4225–4237, 2003.
- [43] R. Kapoor and S. Nemat-Nasser, “Determination of temperature rise during high strain rate deformation,” *Mech. Mater.*, vol. 27, no. 1, pp. 1–12, 1998.
- [44] Y. Me-Bar and D. Shectman, “On the adiabatic shear of Ti-6Al-4V ballistic targets,” *Mater. Sci. Eng.*, vol. 58, no. 2, pp. 181–188, 1983.
- [45] A. G. Odeshi, S. Al-ameeri, and M. N. Bassim, “Effect of high strain rate on plastic deformation of a low alloy steel subjected to ballistic impact,” *J. Mater. Process. Technol.*, vol. 162–163, pp. 385–391, 2005.
- [46] D.-G. Lee, Y. H. Lee, S. Lee, C. S. Lee, and S.-M. Hur, “Dynamic deformation behavior and ballistic impact properties of Ti-6Al-4V alloy having equiaxed and bimodal microstructures,” *Metall. Mater. Trans. A*, vol. 35, no. 10, pp. 3103–3112, 2004.
- [47] A. Marchand and J. Duffy, “An experimental study of the formation process of adiabatic shear bands in a structural steel,” *J. Mech. Phys. Solids*, vol. 36, no. 3, pp. 251–283, 1988.
- [48] I. Gibson, *Advanced manufacturing technology for medical applications: reverse engineering, software conversion and rapid prototyping*. John Wiley & Sons, 2006.
- [49] K. G. Cooper, J. E. Good, and S. D. Gilley, “Layered Metals Fabrication Technology Development for Support of Lunar Exploration at NASA / MSFC,” *Earth*, pp. 728–735, 2007.
- [50] S. Bihamno *et al.*, “Electron beam melting of Ti-48Al-2Cr-2Nb alloy: Microstructure and mechanical properties investigation,” *Intermetallics*, vol. 19, no. 6, pp. 776–781, 2011.
- [51] M. Niinomi, “Recent metallic materials for biomedical applications,” *Metall. Mater. Trans. A*, vol. 33, no. MARCH, pp. 477–486, 2002.
- [52] G. E. Ryan, A. S. Pandit, and D. P. Apatsidis, “Porous titanium scaffolds fabricated using a rapid prototyping and powder metallurgy technique,” *Biomaterials*, vol. 29, pp. 3625–3635, 2008.

- [53] G. A. Rao, M. Kumar, and D. S. Sarma, “Effect of standard heat treatment on the microstructure and mechanical properties of hot isostatically pressed superalloy inconel,” *Mater. Sci. Eng. A*, vol. 355, pp. 114–125, 2003.
- [54] D. Zhang, W. Niu, X. Cao, and Z. Liu, “Effect of standard heat treatment on the microstructure and mechanical properties of selective laser melting manufactured Inconel 718 superalloy,” *Mater. Sci. Eng. A*, vol. 644, pp. 32–40, 2015.
- [55] SAE AMS F Corrosion Heat Resistant Alloys Committee, “AMS5664E: Nickel Alloy, Corrosion and Heat Resistant, Bars, forgings, and Rings, 52.5Ni - 19Cr - 3.0Mo - 5.1Cb - 0.90Ti - 0.50Al - 18Fe, Consumable Electrode or Vacuum Induction Melted, 1950 °F (1066 °C) Solution Heat Treated, Precipitation Hardenable.” SAE International, p. 9, 2006.
- [56] K. Kunze, T. Etter, J. Grässlin, and V. Shklover, “Texture, anisotropy in microstructure and mechanical properties of IN738LC alloy processed by selective laser melting (SLM),” *Mater. Sci. Eng. A*, vol. 620, pp. 213–222, 2015.
- [57] J. Strößner, M. Terock, and U. Glatzel, “Mechanical and Microstructural Investigation of Nickel-Based Superalloy IN718 Manufactured by Selective Laser Melting (SLM),” *Adv. Eng. Mater.*, vol. 17, no. 8, pp. 1099–1105, 2015.
- [58] L. N. Carter, M. M. Attallah, and R. C. Reed, “Laser Powder Bed Fabrication of Nickel-Base Superalloys: Influence of Parameters; Characterisation, Quantification and Mitigation of Cracking,” in *Superalloys 2012: 12th International Symposium on Superalloys*, 2012, pp. 577–586.
- [59] K. N. Amato *et al.*, “Microstructures and mechanical behavior of Inconel 718 fabricated by selective laser melting,” *Acta Mater.*, vol. 60, no. 5, pp. 2229–2239, 2012.
- [60] Y. Lu *et al.*, “Optics & Laser Technology Study on the microstructure , mechanical property and residual stress of SLM Inconel-718 alloy manufactured by differing island scanning strategy,” *Opt. Laser Technol.*, vol. 75, pp. 197–206, 2015.
- [61] X. Wang and K. Chou, “Effects of thermal cycles on the microstructural evolution of Inconel 718 during selective laser melting process,” *Addit. Manuf.*, vol. 18, pp. 1–14, 2017.
- [62] J. W. Yeh *et al.*, “Nanostructured high-entropy alloys with multiple principal elements: Novel alloy design concepts and outcomes,” *Adv. Eng. Mater.*, vol. 6, no. 5, p. 299–303+274, 2004.
- [63] D. B. Miracle and O. N. Senkov, “A critical review of high entropy alloys and related concepts,” *Acta Mater.*, vol. 122, pp. 448–511, 2017.
- [64] M. C. Gao, J. W. Yeh, P. K. Liaw, and Y. Zhang, *High-Entropy Alloys Fundamentals and Applications*. Springer International Publishing, 2014.

- [65] J.-W. Yeh *et al.*, “Formation of simple crystal structures in Cu-Co-Ni-Cr-Al-Fe-Ti-V alloys with multiprincipal metallic elements,” *Metall. Mater. Trans. A*, vol. 35, no. 8, pp. 2533–2536, 2004.
- [66] I. S. Wani, T. Bhattacharjee, S. Sheikh, P. P. Bhattacharjee, S. Guo, and N. Tsuji, “Materials Science & Engineering A eutectic high entropy alloy using thermo-mechanical processing,” *Mater. Sci. Eng. A*, vol. 675, pp. 99–109, 2016.
- [67] N. Kumar *et al.*, “High strain-rate compressive deformation behavior of the Al0.1CrFeCoNi high entropy alloy,” *Mater. Des.*, vol. 86, pp. 598–602, 2015.
- [68] D. Li *et al.*, “High-entropy Al 0.3 CoCrFeNi alloy fibers with high tensile strength and ductility at ambient and cryogenic temperatures,” *Acta Mater.*, vol. 123, pp. 285–294, 2017.
- [69] C. Li, J. C. Li, M. Zhao, and Q. Jiang, “Effect of aluminum contents on microstructure and properties of Al_xCoCrFeNi alloys,” *J. Alloys Compd.*, vol. 504, pp. S515–S518, 2010.
- [70] D. Li and Y. Zhang, “The ultrahigh charpy impact toughness of forged Al_xCoCrFeNi high entropy alloys at room and cryogenic temperatures,” *Intermetallics*, vol. 70, no. July, pp. 24–28, 2016.
- [71] M. Komarasamy, K. Alagarsamy, and R. S. Mishra, “Serration behavior and negative strain rate sensitivity of Al0.1CoCrFeNi high entropy alloy,” *Intermetallics*, vol. 84, pp. 20–24, 2017.
- [72] H. Y. Yasuda, K. Shigeno, and T. Nagase, “Dynamic strain aging of Al0.3CoCrFeNi high entropy alloy single crystals,” *Scr. Mater.*, vol. 108, pp. 80–83, 2015.
- [73] T. T. Shun and Y. C. Du, “Microstructure and tensile behaviors of FCC Al0.3CoCrFeNi high entropy alloy,” *J. Alloys Compd.*, vol. 479, no. 1–2, pp. 157–160, 2009.
- [74] Y. F. Kao, T. J. Chen, S. K. Chen, and J. W. Yeh, “Microstructure and mechanical property of as-cast, homogenized, and deformed Al_xCoCrFeNi high-entropy alloys,” *J. Alloys Compd.*, vol. 488, no. 1, pp. 57–64, 2009.
- [75] J. Joseph, N. Stanford, P. Hodgson, and D. M. Fabijanic, “Tension/compression asymmetry in additive manufactured face centered cubic high entropy alloy,” *Scr. Mater.*, vol. 129, pp. 30–34, 2017.
- [76] Z. Li, S. Zhao, H. Diao, P. K. Liaw, and M. A. Meyers, “High-velocity deformation of remarkable resistance to shear failure,” *Sci. Rep.*, pp. 1–8, 2017.
- [77] C. Tong *et al.*, “Mechanical Performance of the Al x CoCrCuFeNi High-Entropy Alloy System with Multiprincipal Elements,” *Metall. Mater. Trans. A*, vol. 36, no. May, pp. 1263–1271, 2005.

- [78] C. Tsai, Y. Chen, M. Tsai, J. Yeh, T. Shun, and S. Chen, “Deformation and annealing behaviors of high-entropy alloy Al0.5CoCrCuFeNi,” *J. Alloys Compd.*, vol. 486, no. 2009, pp. 427–435, 2010.
- [79] C. Tsai, M. Tsai, J. Yeh, and C. Yang, “Effect of temperature on mechanical properties of Al 0 . 5 CoCrCuFeNi wrought alloy,” *J. Alloys Compd.*, vol. 490, pp. 160–165, 2010.
- [80] M. Tsai *et al.*, “Intermetallics Morphology , structure and composition of precipitates in Al 0 . 3 CoCrCu 0 . 5 FeNi high-entropy alloy,” *Intermetallics*, vol. 32, pp. 329–336, 2013.
- [81] L. H. Wen, H. C. Kou, J. S. Li, H. Chang, X. Y. Xue, and L. Zhou, “Effect of aging temperature on microstructure and properties of AlCoCrCuFeNi high-entropy alloy,” *Intermetallics*, vol. 17, pp. 266–269, 2009.
- [82] A. V. Kuznetsov, D. G. Shaysultanov, N. D. Stepanov, G. A. Salishchev, and O. N. Senkov, “Tensile properties of an AlCrCuNiFeCo high-entropy alloy in as-cast and wrought conditions,” *Mater. Sci. Eng. A*, vol. 533, pp. 107–118, 2012.
- [83] M. Tsai, J. Yeh, M. Tsai, and J. Yeh, “High-Entropy Alloys : A Critical Review,” *Mater. Res. Lett.*, vol. 3831, no. February, 2014.
- [84] S. Guo, C. Ng, J. Lu, and C. T. Liu, “Effect of valence electron concentration on stability of fcc or bcc phase in high entropy alloys,” *J. Appl. Phys.*, vol. 109, no. 10, pp. 1–6, 2011.
- [85] W. Wang, W. Wang, S. Wang, Y. Tsai, C. Lai, and J. Yeh, “Effects of Al addition on the microstructure and mechanical property of Al_xCoCrFeNi high-entropy alloys,” *Intermetallics*, vol. 26, pp. 44–51, 2012.
- [86] A. M. Giwa, P. K. Liaw, K. A. Dahmen, and J. R. Greer, “Microstructure and small-scale size effects in plasticity of individual phases of Al0.7 CoCrFeNi High Entropy alloy,” *Extrem. Mech. Lett.*, vol. 8, pp. 220–228, 2016.
- [87] R. Abbaschian, L. Abbaschian, and R. E. Reed-Hill, *Physical Metallurgy Principles*, 4th ed. CL Engineering, 2009.